EXPERIMENTAL AND COMPUTATIONAL STUDY OF FLUID FLOW AND HEAT TRANSFER IN THE LOST FOAM CASTING PROCESS

Except where reference is made to the work of others, the work described in this dissertation is my own or was done in collaboration with my advisory committee. This dissertation does not include propriety or classified information.

Xuejun Liu

Certificate of Approval:

Ruel A. Overfelt
Professor
Materials Engineering

Sushil H. Bhavnani, Chair
Professor
Mechanical Engineering

Jay M. Khodadadi
Professor
Mechanical Engineering

Amnon J. Meir
Professor
Mathematics and Statistics

Stephen L. McFarland
Dean
Graduate School

EXPERIMENTAL AND COMPUTATIONAL STUDY OF FLUID FLOW AND HEAT TRANSFER IN THE LOST FOAM CASTING PROCESS

Xuejun Liu

A Dissertation

Submitted to

the Graduate Faculty of

Auburn University

in Partial Fulfillment of

the Requirements for the

Degree of

Doctor of Philosophy

Auburn, Alabama
December 16, 2005

EXPERIMENTAL AND COMPUTATIONAL STUDY OF FLUID FLOW AND HEAT TRANSFER IN THE LOST FOAM CASTING PROCESS

Xuejun Liu

Permission is granted to Auburn University to make copies of this dissertation at its discretion, upon the request of individuals or institutions and at their expense. The author reserves all publication rights.

____
Signature of Author

____
Date of Graduation

VITA

Xuejun Liu, son of Chuanzhen Liu and Guorong Li, was born on April 7, 1968, in Liaoning, China. He obtained his Bachelor of Science in Nuclear Power Engineering from Power Mechanical Engineering Department at Shanghai Jiao Tong University, Shanghai, China, in July 1990. He then entered Graduate School of Shanghai Jiao Tong University and graduated with Master of Science degree in Nuclear Power Engineering from Power Mechanical Engineering Department in March 1993. In August 2000, he entered Graduate School of Auburn University for the degree of Doctor of Philosophy in Mechanical Engineering. He married Hong Yang, daughter of Baoan Yang and Manzhen Ma, in March 1995. Xuejun Liu and Hong Yang have a son, Chenyang Liu, who was born on July 2, 1996, in Shanghai, China.

DISSERTATION ABSTRACT

EXPERIMENTAL AND COMPUTATIONAL STUDY OF FLUID FLOW AND HEAT TRANSFER IN THE LOST FOAM CASTING PROCESS

Xuejun Liu

Doctor of Philosophy, December 16, 2005
(M.S., Shanghai Jiao Tong University, 1993)
(B.S., Shanghai Jiao Tong University, 1990)

176 Typed Pages

Directed by Sushil H. Bhavnani

The Lost foam casting (LFC) process has been considered as one of the most significant modern developments in casting technology. The use of polymer foam patterns allow complex shapes to be created by integrating several parts in one casting. Even though the LFC process has been incorporated in casting production around the world, a fundamental understanding of the interaction between the molten metal and foam pattern is limited. Computational modeling, which has proven to be very successful in the simulation and optimization of traditional sand casting, has been hindered by limited knowledge of LFC process. The LFC process, therefore, has yet to be optimized to achieve reductions in cost and time.

This research study consists of two major parts: an experimental study of the transport phenomena between the molten metal front and foam pattern, and a computational simulation of the foam decomposition by improving the basic LFC model in the commercial package FLOW-3D.

In the experimental study, a cylindrical polymer foam pattern and heated steel block were used to study the endothermic losses associated with the thermal degradation of the polymer pattern at the metal front. Thermocouple readings were analyzed to determine the kinetic zone temperature and the heat transfer coefficient between the advancing metal front and the receding foam pattern. Flow visualization was also used to verify the measurements in the kinetic zone. The results showed that the endothermic degradation of the polystyrene pattern at the metal front introduced a steep thermal gradient in the metal and a consistently increasing heat flux and heat transfer coefficient as the foam decomposes. The values of heat transfer coefficient, initially 150 W/m^2·K gradually increased to 220 ~ 300 W/m^2·K to the end of the process. The kinetic zone temperature was measured to be in the range of 150 to 290°C with an average of 200°C and a gaseous gap size of 1 to 4 cm which is further confirmed by the visualization.

In the numerical study, a computational fluid dynamics (CFD) model has been developed to simulate the flow of molten aluminum and the heat transfer at the interfacial gap between the metal front and the foam pattern. The commercial code FLOW-3D provides a basic LFC model that can track the front of the molten metal by a Volume of Fluid (VOF) method and allow complicated parts to be modeled by the Fractional Area/Volume Ratios (FAVOR) method. The code was modified by including the effects of varying interfacial heat transfer coefficient. The modification was validated against experimental studies and the comparison showed improved agreement over the basic model.

ACKNOWLEDGEMENTS

The author would like to sincerely express his special gratitude to his advisor, Dr. Sushil H. Bhavanni, alumni professor in the Department of Mechanical Engineering, for his guidance, encouragement and patience in the completion of the research and dissertation. In particular, his suggestions, discussion and criticism contributed much to this dissertation.

The author is also grateful to his advisory committee members, Dr. Ruel A. Overfelt in Materials Engineering, Dr. Jay K. Khodadadi in Mechanical Engineering, and Dr. Amnon J. Meir in Mathematics and Statistics, for their academic guidance, kindness and help through these years.

Thanks are also due to his colleagues Kenneth F. Wall, Rohan Bhat, Nitesh Nimkar, Daniel Pate and Rory Jones in the Heat Transfer Research Laboratory and staff members in the Department of Mechanical Engineering for their valuable discussion, support and assistance during the period of his study at Auburn University.

Lastly, sincere thanks to his wife, Dr. Hong Yang, who provided the biggest support and encouragement to help the author finish all the research work. The author also wants to thank his son and parents who always give out their hands and give the author joy and encouragement during all the times.

Style manual or journal used: Guide to Preparation and Submission of Thesis and Dissertation

Computer Software used: MSWord 2002, FLOW-3D

TABLE OF CONTENTS

LIST OF TABLES....................xiii

LIST OF FIGURES....................xiv

NOMENCLATURE....................xxi

INTRODUCTION....................1

CHAPTER 1 LITERATURE REVIEW....................6

1.1 Lost Foam Casting Process....................6

1.1.1 Foam Pattern Production and Inspection....................7

1.1.2 Casting Production and Inspection....................8

1.2 Thermal Degradation of Foam Pattern....................9

1.3 Fluid Flow and Heat Transfer in Mold Filling....................11

1.4 Problems with LFC Process....................12

1.5 Process Variables in the Casting Formation Process....................13

1.5.1 Pattern Property....................13

1.5.2 Pattern Coating....................14

1.5.3 Metal Front Velocity....................15

1.5.4 Mold Media....................15

1.6 Visualization and Kinetic Zone....................17

1.7 Modeling of Foam Degradation and Mold Filling...17

    1.7.1 Analytical Models...17

    1.7.2 Computational Fluid Dynamic (CFD) and Heat Transfer Models...20

1.8 Objective of This Study...23

CHAPTER 2 EXPERIMENTAL SETUP AND PROCEDURES...................................31

2.1 Visualization Experiment...31

2.2 Realistic Top-down Experiment..34

2.3 Measurement of Heat Flux and Heat Transfer Coefficient.............................35

2.4 Gas Pressure Measurement...37

2.5 Experimental Procedure...38

2.6 Analysis of Variance (ANOVA) F-Test...39

CHAPTER 3 NUMERICAL MODELING METHOD..47

3.1 Fractional Area/Volume Obstacle Representation (FAVOR) Method...........48

3.2 Governing Equations...49

3.3 SOLution Algorithm and Volume-of-Fluid (SOLA-VOF) method................51

3.4 Overall Solution Procedures..52

3.5 Basic Model of Metal Front Velocity with Gravity Effect.............................53

3.6 Improved Model..56

    3.6.1 Effect of Gas Pressure...56

    3.6.2 Effect of Metal Temperature..57

    3.6.3 Effect of Bead Degree of Fusion..58

3.7 Model of Defect Tracking..59

CHAPTER 4 EXPERIMENTAL RESULTS AND DISCUSSION.................................63

4.1 Morphology of Polymer Foam Patterns..63

4.2 Visualization..64

4.3 Heat Flux and Heat Transfer Coefficient Measurements...............................65

4.4 Pressure Measurements...70

4.5 Effects of Process Variables on Kinetic Zone Temperature...........................73

4.6 Effect of Metal Initial Surface Temperature..74

4.7 Effects of Process Variables on Gas Peak Pressure..75

CHAPTER 5 MODELING RESULTS AND DISCUSSION..89

5.1 Code Verification and Validation...89

5.1.1 Simple Cylinder..89

5.1.2 Simple Plate with Three Ingates..91

5.1.3 GM Box...93

5.1.4 Effect of Metal Temperature...93

5.1.5 Effect of Degree of Bead Fusion...95

5.2 Parametric Study on Defect Formation..96

5.2.1 Simple Plate...96

5.2.2 GM Box...97

CHAPTER 6 CONCLUSIONS..112

REFERENCES..114

APPENDICES..126

A. THERMOPHYSICAL PROPERTIES..126

B. PRESSURE TRANSDUCER CALIBRATION..130

C. UNCERTAINTY ANALYSIS...133

D. LABVIEW® INTERFACE...137

E. SID 2.0 FHNL SERIAL INTERFACE DEVICE PROGRAM.......................141

F. LIST OF R VALUE CORRESPONDING TO VELOCITY OF THE MOTION SYSTEM..143

G. DESIGN OF HEATER AND CYLINDER..145

H. CUSTOMIZED FORTRAN SUBROUTINE FOR THE IMPROVED MODEL..147

I. FLOW-3D® PROJECT INPUT FILE EXAMPLE...151

LIST OF TABLES

Table 4.1 Kinetic zone temperature for different foam and metal front velocities under the same coating thickness of 0.7 cm..73

Table 4.2 Effect of metal initial surface temperature at metal front velocity of 1.5 cm/sec with coating thickness of 0.2 mm for EPS 24 kg/m³.....................74

Table 4.3 Effect of metal initial surface temperature at metal front velocity of 1.5 cm/sec with coating thickness of 0.2 mm for EPS 27 kg/m³.....................75

Table 4.2 ANOVA F-value results of gas peak pressure for the factors of metal front velocity and foam density..76

Table 5.1 Coefficient of Temperature for Different Metal Temperature.........................95

LIST OF FIGURES

Figure 1.1 Flow chart for the lost foam casting process..24

Figure 1.2 Schematic of molten metal pouring in the lost foam casting process............24

Figure 1.3 Photograph showing typical defects (a) surface porosity, (b) large amount of porosity at the metal front near a lap defect, (c) fold area on fracture surface, (d) inclusions on fracture surface, (e) surface collapse of a flange, and (f) misrun of a flange (Shivkumar *et al.*, 1990; Hill *et al.*, 1998)...25

Figure 1.4 Visualization results (a) Yao's (1994) images (M, G, P represents the metal, gas layer, and the polymer pattern) (b) Liu (2001) observation showed a gas zone more than 5 cm wide...26

Figure 1.5 Model with an interface gap (kinetic zone) for the lost foam casting process (Liu *et al.*, 1997)...27

Figure 1.6 Heat and mass transfer processes in the kinetic zone (Warner *et al.*,1998) between the advancing metal front and foam pattern..28

Figure 1.7 (a) Kinetic zone model from Molibog (2002). EPS = expanded p olystyrene; RT = room temperature, (b) Predicted temperature of kinetic zone, and (c) predicted kinetic zone thickness..................................29

Figure 1.8 Undercut model between the metal front and foam pattern proposed by Barone and Caulk (2005)..30

Figure 2.1 (a) Schematic of the visualization experiment set-up, and (b) Sand mold flask showing the visualization window..41

Figure 2.2 Picture of the visualization experiment set-up: (a) a view of overall set-up, and (b) the front view..42

Figure 2.3 Instrumented steel block that simulates the molten metal front in the visualization experiment...43

Figure 2.4 Expanded polymer patterns: (a) uncoated, (b) coated with visualization window left uncoated, and (c) fully coated..43

Figure 2.5 The uncoated part of the foam pattern is in contact with the quartz glass window in the visualization experiment..44

Figure 2.6 Sieve curve of the Olivine sand ASF30 used in experiment.........................44

Figure 2.7 (a) Schematic of experiment set-up for the realistic top-down arrangement showing pressure and temperature measurement locations, (b) picture showing the pressure taps and tubes in the foam pattern, and (c) picture showing the temperature sensors in the foam pattern...........45

Figure 2.8 Position of simulated metal front and foam pattern at different time instances: (a) initial position, (b) at time t_1 the foam around thermocouple D begins to collapse when it reaches collapse temperature, and (c) at time t_2 the metal front reaches thermocouple D resulting in a very rapid rise in temperature.......................46

Figure 2.9 Watlow Series 93 microprocessor-based auto-tuning temperature control...46

Figure 3.1 Typical mesh resolutions of a circular object by (a) finite difference method and (b) finite element method..61

Figure 3.2 The FAVOR method to describe geometry in finite difference grids with definitions of the open area and volume fractions......................61

Figure 3.3 Coarser grid than in standard finite difference methods can be used to represent complex geometries by the FAVOR method...................62

Figure 3.4 Volume of Fluid (VOF) function definition...62

Figure 4.1 Morphology of the polymer foams: (a) outside fused surface, (b) fractured surface for EPS foam polymers, (c) fractured surface for copolymer (70%EPS and 30%PMMA), and (d) hotwire-cut surface...77

Figure 4.2 Morphology of the polymer foams: (a) coating and foam residual in a half-run test, and (b) close look of the foam interface...........................78

Figure 4.3 (a) Quartz window observations and gaseous gap size for a foam density of 24 kg/m³ with a metal front velocity of 0.036 cm/s and coating thickness of 0.12 cm at (i) 0 second, (ii) 10 seconds, (iii) 20 seconds, (iv) 30 seconds, (v) 40 seconds, (vi) 50 seconds, (vii) 60 seconds, and (viii) 70 seconds. The arrow indicates the metal front position. (b) Gap size observed from these images...................79

Figure 4.4 (a) Quartz window observations and gaseous gap size for a foam density of 27 kg/m3 with a metal front velocity of 1.5 cm/s at (i) 0 second, (ii) 5 seconds, and (iii) 10 seconds. The arrow indicates the metal front position. (b) Gap size observed from these images and measured from thermocouples...80

Figure 4.5 Response of thermocouples inside simulated metal front for a foam density of 24 kg/m³ with velocity of 0.44 cm/s and coating thickness of 0.12 cm..........81

Figure 4.6 Heat flux at the simulated metal front for a velocity of (a) 0.44 cm/s, and (b) 1.5 cm/s with coating thickness of 0.12 cm..........82

Figure 4.7 Response of thermocouples inside the foam pattern showing the kinetic zone for 27 kg/m³ foam pattern with a coating thickness of 0.07 cm under the metal front velocity of 0.95 cm/s..........83

Figure 4.8 With metal front velocity of 0.95 cm/s, EPS foam density of 27 kg/m³ and coating thickness of 0.07 cm (a) Kinetic zone temperature, and (b) gaseous gap size..........84

Figure 4.9 Kinetic zone temperature for different metal front velocities with different EPS foam density and coating thickness..........85

Figure 4.10 Heat transfer coefficient for a velocity of (a) 0.44 cm/s, and (b) 1.5 cm/s with coating thickness of 0.12 cm..........86

Figure 4.11 Gap peak pressure as a function of simulated metal front velocity for all the coating thicknesses in both visualization and realistic top-down experiments: (a) foam density of 24 kg/m³ and (b) foam density 27 kg/m³. Gap average peak pressures for a coating thickness of 0.12 cm are listed in the table above..........87

Figure 4.12 Verification of pressure measurement of pressure tap P by another two taps P1 and P2 for a metal front velocity of 1.5 cm/s with a foam density of 27 kg/m³ and coating thickness 0.07 cm. The two arrows show the useful part of pressure signal before the metal front pushes the pressure taps.....88

Figure 4.13 Gas pressure between the metal front and foam pattern as a function of foam density (Mirbagheri et al., 2004). The blue star shows the possible gas pressure for the foam density in the present work.....88

Figure 5.1 Computational domains: (a) cylinder, (b) plate with 3 ingates, (c) plate with side ingate, (d) GM box, and (d) GM box with sprue configuration.....98

Figure 5.2 The mass flow rate at the entrance of the gate as a function of the grid size in the longitudinal direction.....99

Figure 5.3 Experimental validation of basic model with gravity effect and improved model with varying heat transfer coefficient dependent on gas pressure for EPS foam with density 24kg/m³, coating thickness of 0.7 mm and metal front velocity of 1.5 cm/sec.....100

Figure 5.4 Relation between correction factor for gas pressure and coating thickness.....101

Figure 5.5 Mold fill time as a function of (a) coating thickness and (b) metal front velocity.....101

Figure 5.6 Comparison of mold filling times for a plate pattern: (a) measured values by thermometric technique (Shivkumar and Galois, 1987), (b) simulation filling times based on heat transfer coefficient model with gravity effect, and (c) simulation filling times filing times based on the modified model with heat transfer coefficient based on both gas pressure and coating thickness......................................102

Figure 5.7 Mold filling time at the right wall of the mold for the plate pattern with 3 ingates...103

Figure 5.8 Mold filling times at various locations in the casting with 3 side gates for a foam pattern with average degree of fusion of 76% for (a) and 51% for (b). The filling time was determined from the responses of chromel-alumel thermocouples positioned at various locations during the production of the casting (Sand and Shivkumar, 2005)........................104

Figure 5.9 Comparisons of filling times predicted by the two models: (a) default heat transfer model with gravity effect, and (b) and (c) modified model with heat transfer coefficient based on both gas pressure and coating thickness for average degree of bead of fusion 51% and 76%. Color indicates time of filling (blue is earliest and red latest)...................105

Figure 5.10 Experimental results for Yao (1994) showing the temperature effect on the molding filling times. The arrow represents the position of the ingate: (a) 190°C, (b) 490°C, (c) 715°C, and (d) 1115°C..........................106

Figure 5.11 Simulation results showing the temperature effect on the molding filling times. Color indicates time of filling (blue is earliest and red latest): (a) 190°C, (b) 490°C, (c) 715°C, and (d) 1115°C..........................107

Figure 5.12 Mold filling time at the right side surface of mold showing the temperature effect..108

Figure 5.13 Experimental results for Yao (1994) showing the effect of bead fusion on the molding filling times. The arrow represents the position of the ingate: (a) lower degree of bead fusion with foam density of 26 kg/m³, and (b) higher degree of bead fusion with foam density of 21 kg/m³.........109

Figure 5.14 Simulation results showing the effect of bead fusion on the molding filling times. Color indicates time of filling (blue is earliest and red latest): (a) lower degree of bead fusion with foam density of 26 kg/m³, and (b) higher degree of bead fusion with foam density of 21 kg/m³.........110

Figure 5.15 Defects formation predicted by (a) basic heat transfer coefficient model with gravity effect, (b) improved model with heat transfer coefficient based on both gas pressure and coating thickness, and (c) improved model for two ingates. Color represents probability for defects (blue is the lowest and red highest)...111

Figure 5.16 Comparisons of defects formation predicted by the two models: (a) basic heat transfer model with gravity effect, and (b) improved model with heat transfer coefficient based on gas pressure. Color represents probability for defects (blue is the lowest and red highest).......111

NOMENCLATURE

English Symbols

A_c	cross-section area of metal/foam interface, m^2
A_x	fractional area open to flow in the x direction
A_y	fractional area open to flow in the y direction
A_z	fractional area open to flow in the z direction
c_D	coefficient of bead fusion
c_p	foam specific heat, W/kg·K
c_g	gravity factor
c_k	pressure coefficient
c_T	temperature coefficient
A, B, C, D, E, F, and G	thermocouples at different locations
DOF_a	average degree of bead fusion
DOF_D	foam degree of bead fusion
EPS	Expanded Polystyrene
F	volume fraction
f_D	correction factor for foam bead degree of fusion
f_p	correction factor for gas pressure
f_T	correction factor for metal temperature
f_v	correction factor for metal front velocity
g_{ht}	gravity component normal to metal/foam front

h	heat transfer coefficient, W/m²·K
I	macroscopic mixture internal energy, W
k	thermal conductivity, W/m·K
P, P1 and P2	pressure taps and transducers
p_g	gas pressure in the kinetic zone, Pa
p_h	average pressure head for the pouring of metal in the sprue, Pa
q_s	heat transfer rate from metal front to the kinetic zone, W
q_f	surface heat flux to the foam, W/m²
Q_{liq}	latent heat of fusion of foam, J/kg
Q_{vap}	heat of vaporization of foam, J/kg
Q_{depoly}	heat of depolymerization of foam, J/kg
r_m	fixed reference radius
R	= 1 for Cartesian coordinate, = r_m/r for cylindrical coordinate
t_c	ratio of coating thickness to the characteristic length scale of the surface irregularities at the metal/foam interface
T_z	temperature in the gaseous gap, °C
T_s	metal front surface temperature, °C
T_∞	initial foam temperature, °C
T_p	peak volatilization temperature, °C
T_m	metal pouring temperature, °C
$TDIF$	heat diffusion term
V_{adv}	metal front advancing velocity, m/s
V_{rec}	foam recession velocity, m/s

V_{ht}	nominal velocity of the metal front, m/s
V_g	characteristic speed of gravity waves, m/s
V_m	metal front velocity, m/s
r_s	characteristic length scale of the surface irregularities at the metal/foam interface
(u, v, w)	velocity components
(x, y, z)	Cartesian coordinate directions
(r, θ, z)	cylindrical coordinate directions
(G_x, G_y, G_z)	body acceleration, N/kg
(F_x, F_y, F_z)	viscous forces per unit mass, N/kg

Greek Symbols

ρ	foam density, kg/m^3
ρ_{EPS}	density of EPS pattern, kg/m^3
ρ_{KZ}	average density of degradation products in the kinetic zone, kg/m^3
δ	thickness of kinetic zone.
ξ	coordinate constant, = 1 for cylindrical coordinate, = 0 for Cartesian coordinate

Subscripts

s	related to the metal front surface
z	related to the kinetic zone

INTRODUCTION

As a unique technique to produce integrated components which otherwise must be cast in several parts, the lost foam casting (LFC) process has drawn great interest from both academia and industry. Significant advances in understanding and controlling the LFC process have enabled rapid growth of LFC production around the world. Casting output in LFC process is increasing about 20% every year in North America (Bates *et al.*, 2001).

Originally, the LFC process was invented and patented by Shroyer (1958) using a foam pattern of the desired shape in bonded sand and pouring molten metal to form the casting. He named the new casting technique the “cavityless casting mold” method. An improvement was made by Smith (1964) who patented the LFC process with unbonded sand. Since then the lost foam casting process has been called a variety of names, such as full-mold casting, evaporative casting, and expendable casting (Lessiter, 1994; Liu, 2001). The LFC process was mainly used by art casters and did not receive much commercial interest from foundries for nearly three decades after it was invented. In the late 1980s, driven by the need for weight and cost reduction, usage of the LFC process gained new momentum. Large companies like General Motors and its Saturn subsidiary currently use the LFC process to produce a wide variety of products for automobiles, such as intake manifolds, engine blocks and cylinder heads (Lessiter, 2000). Because of the similarities with the well-established lost wax casting process, both industrial practitioners and academic researchers have settled on the name − lost foam casting.

The key feature of the LFC process is that a polymer foam pattern of the desired shape is buried in unbonded sand and replaced by advancing molten metal. The polymer pattern of required shape is initially produced by injection molding. The most widely used polymer is expanded polystyrene (EPS), whereas other polymers such as polymethyl methacrylate (PMMA) and polyalkylene carbonate (PAC) are also used to manufacture ferrous castings (Walling and Dantzig, 1994).

There are many advantages that the LFC offers over conventional empty mold casting processes (Wong, 2000; Miller, 1996). For instance, it eliminates the requirements of cores for internal structures because foam patterns are used in sand mold during pouring of molten metal. This also allows several parts to be integrated and makes more complex casting designs possible. The high cost to make the EPS foam pattern is justified by integration of several components, elimination of required cores, increased dimensional accuracy, and saved material required for post-machining process. Another advantage of the LFC process is that sand is reusable and it requires minimal cleaning because no binders are used, which makes LFC a more environmentally friendly process. This process also eliminates issues like dewaxing and mold firing that occur in the lost wax process. It has been shown that the mechanical properties of lost foam castings are better than or comparable to those produced in traditional green sand castings, but are inferior to the properties observed in permanent mold products (Shivkumar *et al.*, 1990). Other attractive features include near-net-shape casting, elimination of parting lines, excellent surface finish, low wear and long life with aluminum tools, and lower capital investment. A comparison of surface finish with shell mold and sand casting is shown below (Mazouz, 2000).

Process	Surface Finish (RMS)
Lost Foam Casting	60-300
Shell Mold	120-300
Sand Casting	560-900

Though studies have been conducted successfully to cast all ferrous and nonferrous metals using LFC process, only aluminum and iron castings are widely produced in foundries because the metal pouring temperature needs to be higher than 550°C to completely decompose the foam pattern and gating system. Lower melting temperature metals can be poured, but the size of the product is limited. Additionally, very low carbon ferrous casting requires special processing and treatment due to carbon-pickup in the process. The projected market share of aluminum casting using LFC process is about 30% of the total aluminum production in the North America in 2010, whereas for iron production it is about 15% (Garland, 2003). For aluminum alloys, LFC is the most widely used among all the LFC processes.

From the viewpoint of economic and commercial potential, the LFC process uses almost a quarter less energy and a third less molten metal than conventional casting by cutting the use of natural gas and electricity, reducing costs for sand cleaning, and saving downstream machining and assembly (Barnett, 2002). However, the excessive scrap rates require extra energy to re-melt the metal, decrease productivity, and inevitably increase the production cost. It has been estimated that a 7% reduction in scrap would expand application of LFC process from the 36 foundries to all of the 2,900 foundries in the United States, resulting in saving 660 million kW·h of natural gas and electricity annually by 2010.

The need to reduce scrap rate has drawn great effort in the research of effect of process and design variables on the defect formation in the LFC process. Extensive experimental investigations have been performed to study effect of process parameters involved in the production process (Wang *et al.*, 1990; Sun *et al.*, 1996; Liu *et al.*, 1997; Hill *et al.*, 1997; Cai *et al.*, 2002). Influence of foam processing variables on polymer degradation has also been investigated (Celotto *et al.*, 1994; Rossacci and Shivkumar, 2003). It has been recognized that the pyrolysis products are the main source of defects in lost foam casting (Wang *et al.*, 1990; Green *et al.*, 1998). Study of the "white side" – foam pattern properties − has drawn interest toward the study of process variables in the foam production process (Smith and Biederman, 2000; Wall *et al.*, 2003; Bhat *et al.*, 2005). Due to the complexity of the LFC process, important parameters such as the heat transfer coefficient between the metal front and the foam pattern has not been quantified. Several experiments have been carried out to measure the heat transfer coefficient between the metal and mold. These experiments have resulted in heat transfer coefficient between the metal and mold in the range of 40 − 160 W/m²·K (Khan *et al.*, 2000 and 2001).

In addition to the experimental study of the LFC process, computational models have been developed to better understand the interactions of various process variables in order to help reduce defect formation in the castings. (Tsai and Chen, 1988; Chen *et al.*, 1997; Hirt and Barkhudarov, 1997; Sun *et al.*, 2004, Mirbagheri, *et al.*, 2004). Since the heat transfer between the metal front and foam pattern plays a very important role in the LFC process, models without sufficient consideration of the foam pyrolysis process do not capture the effect of process parameters on the defect formation in the castings.

The current study is focused on the heat and mass transfer between the metal front and foam pattern by both experimental measurements and numerical modeling of the foam elimination process in the production of aluminum alloy casting. The main objective is to understand the effect of process and design variables on the heat and mass transfer while the molten metal is advancing and the foam is receding. Also, the commercial simulation package FLOW-3D is applied and its source code modified to incorporate experimental results to provide a more realistic model to study the LFC process.

CHAPTER 1 LITERATURE REVIEW

In this chapter, the lost foam casting process is reviewed with an emphasis on industrial procedures, technological aspects, process variables, and recent developments in the fields. Both experimental and computational techniques are discussed, and a comprehensive study of current research is summarized.

1.1 Lost Foam Casting Process

Reynolds (1999) summarized nine major procedures in the LFC process as shown in Figure 1.1. Every step needs to be carefully monitored for the purpose of producing consistent and high-quality castings. It is generally agreed that the LFC process is more susceptible to process changes than any other casting processes because of numerous variables and complex interactions between them. In some foundries the approach of "don't touch anything" is utilized when casting results are satisfactory because of an insufficient understanding of critical variables and their interactions. In current industrial LFC foundries, the nine basics procedures of the process are practiced in two major sections:

- Foam pattern production and inspection
- Casting production and inspection.

1.1.1 Foam Pattern Production and Inspection

Smith and Biederman (2000) suggested that a very large percent of defects formed in castings are due to the problems in the foam pattern. Wall *et al.* (2003) and Bhat (2005) did a comprehensive review on the production of EPS foam patterns and performed an experimental study on the process and design variables for the pattern production. In this part of production, raw beads go through three major steps which are pre-expansion, stabilization and molding. In order to produce high quality castings, it is necessary to start with high quality foam patterns. The foam patterns need to be dimensionally accurate and have constant bead properties such as bead fusion and foam density.

In pre-expansion, raw expandable beads are fed into a preheated vessel where they are heated to 90°C and expanded by steam and air under controlled temperature, pressure and flow rate. Meanwhile, expanding agents such as pentane are applied with certain additives and agitation.

Then the pre-expanded beads are dried in a fluid bed drier and kept in bins to reach ambient temperature, which is called the stabilization or maturing process. The stabilization time can vary from few hours to four days depending upon bead density. As the beads exit the pre-expander, vacuum is created in the newly created cellular structure of the foam. The stabilization process allows the air to diffuse into the beads and balance the pressure, and dissipate excess water and blowing agent out of the beads.

During the molding process the matured beads are blown into a canister with vents to produce the pattern. Beads are fed through injectors into the mold cavity, then high pressurized steam is passed though the mold causing the beads to soften, expand and fuse to form a solid pattern. The canister is then cooled and opened, and the foam pattern is removed. Fresh molded foam patterns are stored for at least 24 hours for them to stabilize in a controlled atmosphere, free from cold draft. Complex patterns may be produced by bonding several individual patterns, using hot-melt adhesive.

Finally the foam patterns are inspected for foam defects, such as dimensional inaccuracy, shrinkage and expansion, dents, cracks, tears, and density variations. Any deviation from the right bead production process can lead to defects in the final casting. Statistical process control is usually applied for comparison with historical data and to determine the trends or stability of the pattern quality (Reynolds, 1999).

1.1.2 Casting Production and Inspection

Several identical castings can be produced in one flask by bonding patterns into clusters with hot-adhesive. After the patterns are assembled into clusters with necessary gating systems, they are then coated with a thin layer of water-based refractory slurry which provides support against the weight of the sand before the molten metal solidifies, withstands the high temperature of molten metal, provides insulation to keep the molten metal from losing too much heat and solidifying prematurely, and helps eliminate the foam products of liquids and gases. After the coating process, the wet clusters are placed in humidity- and temperature-controlled rooms for drying. After the coating is dried, pattern clusters are positioned in the flask, and loose, unbonded sand is rained around the clusters while vibrators are used to compact the sand to build strength.

Finally, without removing the foam patterns, molten metal is poured into the mold. The schematic of the metal pouring process is shown in Figure 1.2. The heat from the molten metal immediately vaporizes the patterns and fills the mold cavity, completely replacing the space previously occupied by the foam patterns and leaving desired dimensional casting products. As the metal replaces the foam pattern, the process involves a series of complex foam reactions: collapse, liquefaction, vaporization, and depolymerization. The degradation products are vented through the coating layer into the surrounding sand. The quality of castings in the LFC process is strongly affected by the elimination of liquid and gaseous products produced by the foam pattern (Hill *et al.*, 1998; Green *et al.*, 1998, Liu *et al.*, 2002). If the foam pyrolysis products can not be effectively eliminated from the casting, they can cause various defects as discussed in detailed in Section 1.4. After the castings cool down, they are shaken out, de-gated, cleaned and inspected for quality. These final procedures are similar to those used in conventional casting processes.

1.2 Thermal Degradation of Foam Pattern

The polymer materials used in LFC undergo thermal depolymerization at elevated temperatures. Yao (1994), Mehta and Shivkumar (1994) and Mehta *et al.* (1995) studied the thermal degradation of polymers in several stages. During the initial stage, as temperature is increased, the polymer retains its structure without any changes until the temperature reaches the glass transition temperature (T_g). Above T_g, the polymer molecules gain enough translational freedom and the viscosity of the polymer decreases rapidly. With further increase in temperature, the polymer starts to collapse; this is known as the collapse point. Additional temperature rise results in breakdown of the polymer chain yielding a partially depolymerized residue which consists of monomers, dimers, and other oligmers.

Expanded polystyrene (EPS) is the most commonly used polymer for aluminum casting. EPS is a linear hydrocarbon with a chemical formula of $(C_8H_8)_n$ and a molecular weight of about 300,000. The characteristics of EPS thermal degradation are summarized in Appendix A, Table A.1. When exposed to elevated temperatures above the glass transition temperature, the polymer beads collapse at about 120°C and the volume decreases substantially, to 1/40 of its original size. As temperature increases, the collapsed polymer undergoes depolymerization by a mechanism referred to as random scission. The C-C bonds in the polymer chain are broken randomly at various locations. At 160°C, the collapsed beads melt to form viscous residue which consists predominantly of partially depolymerized products such as dimer, trimer, and tetramer. As the temperature increases to above 275°C, the polymer starts to volatize and reaches maximum volatization at about 400°C. Up to about 500°C, the volatized products consist primarily of styrene monomer (C_8H_8). As temperature is increased further, the gases undergo additional fragmentation. At about 750°C, the gaseous products contain styrene, toluene (C_7H_8), benzene (C_6H_6), ethylene (C_2H_4), acetylene (C_2H_2) and methane (CH_4). The formation of hydrogen and graphitic carbon results in carbon-related defects in cast iron known as “lustrous carbon defects.” Gas yields have been measured to be on the order of 230 cm^3(STP)/g at 750°C and 760 cm^3(STP)/g at 1300°C.

Carbon-related defects may be eliminated by using polymethl methacrylate (PMMA) as the pattern material instead of EPS for ferrous casting. PMMA is also a linear polymer with a chemical formula of $(C_5H_8O_2)_n$ and undergoes degradation by a mechanism referred to as “unzipping.” As temperature is increased, the scission of the polymer occurs primarily by monomer units splitting off at the end of the molecular chain which leads to very high monomer yields (95-100%). The presence of two oxygen atoms in the monomer molecule facilitates the conversion of carbon to CO, minimizing carbon-related defects. The characteristics of PMMA degradation are also listed in Appendix A, TableA.1.

Recently, other polymers such as polyalkylene carbonate (PAC) and copolymers of EPS and PMMA have been developed and used in the lost foam casting process in order to minimize carbon defects in ferrous casting.

1.3 Fluid Flow and Heat Transfer in Mold Filling

In most traditional empty mold casting processes, molten metal is introduced into the mold cavity under the influence of gravity. The metal flow characteristic is usually turbulent and non-uniform. Additionally, unfavorable temperature gradients may exist and the ensuing lack of directional solidification may lead to shrinkage and porosities in the solidified casting. To solve the problem, appropriate gate and riser systems are designed in most conventional casting processes (Lawrence *et al.*, 1998).

In LFC, the metal flow pattern is essentially governed by the thermal degradation of the polymer pattern at the metal front. The continual back pressure exerted by the foam pattern and polymer degradation products during mold filling acts as a resistance to the flow of liquid metal. The molten metal flows through the gates and displaces the foam pattern with a significantly lower velocity than conventional sand casting processes. Consequently, the metal and pattern interface is relatively smooth and uniform. It has been reported that laminar flow is achieved in thin sections with a head less than 36 cm resulting in a Reynolds number in the range of 400 to 3000 (Shivkumar and Galois, 1987). Typical flow velocities at the metal front have been measured to be several centimeters per second for lost foam casting process and two orders of magnitude higher for green sand casting process (Tseng and Askeland, 1991).

1.4 Problems with the LFC Process

Despite the advantages that LFC offers, it has been known that the quality of castings is more sensitive to process variables than in traditional casting processes. There are unique internal inclusions and surface porosities formed in the castings, which are mostly related to the products of foam during the foam elimination process (Hill *et al.*, 1998). The EPS foam pattern undergoes a series of complex reactions: collapse, liquefaction, vaporization, and depolymerization. Molibog (2002) and Warner *et al.* (1998) showed that the pyrolysis liquid and gaseous products are potential defect sources and the effective elimination of these degradation products is important to produce sound parts. Common LFC defects − internal porosity, folds and surface defects − shown in Figure 1.3 (Shivkumar *et al.*, 1990) are all pyrolysis product related.

Porosity defects are created when a fast moving metal front engulfs portions of the foam pattern which form voids in the solidified castings. Folds are caused when two streams of molten metal meet and pyrolysis products at the metal front prevent the two streams of metal from fusing. Surface defects are present at the surface of the casting, and are a result of foam pyrolysis products trapped at the metal – coating interface. It is believed that the uniformity of foam density, coating properties, and metal front velocity are among the most important variables that affect the defect formation.

1.5 Process Variables in the Casting Formation Process

Unlike traditional sand casting, LFC is relatively new and the process parameters are not well understood and quantified. Hence, a lot of difficulties have been encountered in industrial production. This leads to surface and internal defects mostly caused by the pyrolysis products when the EPS foam patterns are replaced by the molten metal. Several process variables need to be closely monitored in the LFC process in order to produce defect-free castings.

1.5.1 Pattern Properties

The properties of the pattern may significantly affect the casting quality. A very large percent of defects caused in castings are attributed to the non-uniformity in pattern density. Instead of molten metal uniformly displacing the foam, the metal tends to flow towards the lower density areas in the pattern. This causes various streams of molten metal to interact, causing folds and foam inclusions in a cast part. Additionally, when the foam has a region of low degree of bead fusion, metal is observed to move much faster in that part of the pattern. It has generally been agreed that pattern density variation inside the pattern and degrees of bead fusion are the two most important factors (Sands and Shivkumar, 2003 and 2005). For a 64% increase in foam density, the fill times of the molten metal are measured to increase about 2 times. For an increase of 50% bead degree of fusion, the fill times increase about 45%.

In the pattern production process, the temperature, time and pressure at which steam is passed during the bead molding process have a great effect of bead fusion. The pattern density variation is affected by variation in pressure while blowing beads, pressure in bead canister, venting configuration, location of injectors, and thickness of pattern cross-section (Bhat, 2005).

1.5.2 Pattern Coating

The refractory layer coating the outside of the foam pattern has been recognized as a critical factor to good quality castings (Goria *et al.*, 1896; Lessiter, 1996). If the gaseous and liquid pyrolysis products are not released through the coating in a timely manner, the gas pressure in the kinetic zone increases until it exceeds the metallostatic pressure. The gases now escape through the molten metal discontinuously and form defects in the castings. On the contrary, if the pyrolysis products are released too fast, local pressure drops are sufficient high to cause sand collapse. The coating layer is then not supported by gas or metal pressure and can no longer bear the weight of the sand. This leads to surface collapse defects. An ideal pattern coating must allow gaseous and liquid foam degradation products to be transported out of the casting in a timely and balanced manner. Variables such as coating material, percent solid, viscosity, liquid absorption capability, coating thickness and gas permeability affect the quality of casting. There is no standard method to measure and control liquid absorption and gas permeability. To produce good quality castings, consistent coating properties including wettability, permeability and viscosity should be maintained. In a recent development, additional binders and chemical agents have been applied to produce a reactive coating which has an elastic behavior before casting and reacts immediately to produce the required properties when heated by the molten metal (Salah *et al.*, 2002). The coating layer can be easily removed from the casting after it cools down.

1.5.3 Metal Front Velocity

Hill *et al.* (1998) correlated the metal front velocity and shape with the quality of casting products. It was found that there exists a critical velocity window of 1.4 to 1.8 cm/s which produces defect-free castings for the aluminum flanges produced in the study. If the metal front velocity is above the critical range, internal porosity, folds, and surface carbon defects and even serious penetration occur. Figure 1.3 (a) to (d) show surface and internal porosities and fold defects. A metal front velocity below the critical range led to the formation of surface collapse and misruns as shown in Figure 1.3 (e) and (f). Other casting parameters need to be adjusted to provide a metal front velocity within the critical window in order to assure good quality castings.

1.5.4 Mold Media

The condition of the sand used in the LFC process has an effect on casting quality. Since the sand used in LFC is unbonded without any binders, defects related to additives and water in conventional molding are eliminated. During casting, the liquid foam products wick through the coating into the sand. Meanwhile, gas foam products penetrate through the coating into the sand, and depending on the sand properties such as permeability, fineness and thermal conductivity the gas may condense into liquid again or continue to travel through the sand as more heat is transferred from molten metal. The use of coarse-grain sand allows gases to escape faster from the sand to the atmosphere (Sands and Shivkumar, 2003). The mold filling time can increase 50% at its maximum for finer sands than coarser sands. Under extreme conditions, where impermeable mold is used, the mold filling time increases by over 5 times of the typical value since the pyrolysis products have to escape through the molten metal.

Silica sand, the most widely used unbonded sand, tends to produce larger castings when hot and smaller casting in cold conditions. Silica sand undergoes phase transformation to lower density sand causing gross sand movement. Since this movement is in the direction parallel to the flow of molten metal, the casting dimension is larger in this direction. Sand with low thermal expansion coefficient and high diffusivity produces better dimensional accuracy. It has been observed that high temperature of sand increases the occurrence of folds and blisters. To obtain better dimensional accuracy chromite, silicon carbide, mulite, carbon and olivine sands are recommended. Sands used in LFC require high heat diffusivity and must not have a total linear expansion greater than 1% when the temperature is varied from 0°C to 1600°C. Additionally, sand compaction and control have been identified as important factors that affect the precision and productivity of the LFC process (Lessiter, 1997). To allow sand to flow into pattern cavities and produce a rigid support with sufficient strength to resist metal and gas pressure in the metal pouring, sand is vibrated during flask filling, but this may result in pattern distortion, which is critical for producing castings with fine features and internal structures. Industrial suppliers are developing a new generation of equipment to improve the sand fill and compaction process (Sheldon, 2002). Horizontal compaction showed maximum densification with minimum distortion and least amount of energy used.

1.6 Visualization and Kinetic Zone

Tseng and Askeland (1991), Yao (1994), Walling (1995), and Liu (2001) used transparent windows to investigate the existence of a gaseous gap between the molten metal front and the foam pattern. Tseng and Askeland (1991) and Walling (1995) reported that no vapor gap was observed between the liquid metal and the EPS pattern during the aluminum filling process. But images recorded by Yao (1994) (Figure 1.4(a)) and Liu (2001) (Figure 1.4(b)) showed that a gas layer develops at the metal front and the maximum length is more than 5 cm. In Yao's image, the foam pattern turns into finger-like shapes in front of the molten metal.

Liu *et al.* (1997) established an interface gap model to describe the foam-metal-coating interface between the metal front and EPS pattern as show in Figure 1.5. The model was further developed and a kinetic zone, which is the gap between the advancing metal front and the receding foam pattern, was proposed by Warner *et al.* (1998) to model the LFC process. During the mold filling process, the degradation products escape from the kinetic zone through the coating layer into the sand. Complex reactions occuring between the molten metal and foam pattern makes the simulation of LFC extremely difficult. The kinetic zone model with heat and mass transfer is shown in Figure 1.6. The heat and mass transfer phenomena require extraordinary simplification to allow mathematical representations of the LFC process.

1.7 Modeling of Foam Degradation and Mold Filling

1.7.1 Analytical Models

Molibog (2002) developed a mathematical model based on the assumption that a uniform kinetic zone exists between the metal front and foam pattern. Fluid flow in the kinetic zone was assumed two dimensional and laminar with a parabolic longitudinal velocity profile shown in Figure 1.7(a). The longitudinal fluid velocity component was found to be

$$v(x,y) = -\frac{6V_{rec}\rho_{EPS}}{\rho_{KZ}}\, y\left(\frac{x^2}{\delta^3} - \frac{x}{\delta^2}\right) \tag{1.1}$$

where $v(x,y)$ is the longitudinal velocity;

V_{rec} is the foam recession velocity;

ρ_{EPS} is the density of EPS pattern;

ρ_{KZ} is the average density of degradation products in the kinetic zone;

δ is the thickness of kinetic zone.

By solving the mass conservation equation for two-dimensional incompressible flow, the transverse velocity component, u, was found to be

$$u(x) = V_{rec}\frac{\rho_{EPS}}{\rho_{KZ}}\left(\frac{2x^3}{\delta^3} - \frac{3x^2}{\delta^2}\right) \tag{1.2}$$

The temperature in the kinetic zone was assumed to vary from the heater temperature, T_h, at the heater surface to the EPS melting temperature, T_m, chosen at 150°C. An energy balance in the kinetic zone was described by the general energy conservation equation for fluid flow with internal energy consumption. The energy equation was then solved analytically by the power series. The average temperature of the kinetic zone was predicted to have a linear relation with metal front temperature as shown in Figure 1.7(b). The foam recession velocity did not exhibit a strong effect on the kinetic zone temperature. The predicted average kinetic zone temperature varied from 320°C to 400°C in the heater temperature range of 590°C to 790°C. The predicted thickness of the kinetic zone was shown in Figure 1.7(c). At a recession rate of 1 cm/s, the kinetic zone thickness increased from about 0.19 mm to 0.26 mm as the heater temperature increased from 590°C to 790°C. At recession rate of 3 cm/s and 4.5 cm/s, the kinetic zone thickness was not affected by the heater temperature and had average values of 0.06 mm and 0.04 mm, respectively. The kinetic zone model introduced a new way of analyzing the gaseous gap in LFC. Since the model did not include the escape of gaseous product, effect of foam density and gravity orientation which are all shown to be important to the process, the model is not sufficient to provide a comprehensive understanding of LFC.

More recently Barone and Caulk (2005) proposed a coating undercut at the pattern boundary where gas diffuses through the coating and into the sand as shown in Figure 1.8. Most of the pattern interior decomposes by ablation, but the boundary cells decompose by a collapse mechanism, which creates an undercut in the pattern next to the coating. The model successfully showed that filling speeds are independent of pattern thickness, strongly dependent on sand temperature, weakly dependent on metal temperature and much faster in cut foam compared with molded foam. But the model did not include coating effects and was not validated by experimental data.

1.7.2 Computational Fluid Dynamics (CFD) and Heat Transfer Models

The simulation of traditional sand casting with an empty mold has been studied extensively since the SOLution Algorithm-Volume of Fluid (SOLA-VOF) method was originally formulated by Hirt and Nichols (1981). Hwang and Stoehr (1983) first applied it to the modeling of traditional green sand casting problems. Because this code can capture the metal front surface, most of the finite difference and finite volume models in casting simulation are based on the SOLA-VOF method. Due to the fact that lost foam casting process shares a lot of similar characteristics with traditional sand casting, the theory and techniques applied to model LFC mostly originated from simulation methods of traditional sand casting.

Earlier modeling of LFC process was based on an energy balance between the metal and foam pattern without attempts to simulate the fluid flow. Tsai and Chen (1988) used the finite element method to solve the heat transfer equations which simplified the metal flow into a constant flow field. The major findings were that the fluidity of the metal, which is defined as the distance that the metal flows before freezing, decreases as pattern density increases and as the pouring temperature decreases. Chang and Tsai (1989) modified the model and found that latent heat release due to casting solidification can increase the metal fluidity. Abayarathna and Tsai (1989) continued the previous study and used the finite difference method to study the carbon diffusion in the casting and heat and mass transfer in the sand mold. Their results suggested that the application of a vacuum to quickly suck the polystyrene mixture from the sand mold can reduce the casting carburization. Shivkumar (1994) also used a finite difference method to solve the energy equation at the metal front with the assumption that there is no gas layer between the metal front and foam pattern. The model was successful in predicting the temperature losses in the liquid metal accompanying the endothermic degradation of the polymer pattern. In all the above-mentioned studies the metal flow field was simplified to a constant metal front velocity and only the energy equation was solved. The boundary conditions include constant heat transfer coefficients between molten metal and the sand mold and between metal and the foam pattern.

Recognizing the physical importance of interaction of metal flow field and the foam pattern, researchers started to include the fluid flow and heat transfer in their models. By assuming that the pattern decomposition rate is a linear function of metallostatic head and metal front temperature, Wang *et al.* (1993) simulated the lost foam casting process in an arbitrary 3-D geometry based on the existing computer program of conventional sand casting. Liu *et al.* (2002) included back pressure in the kinetic zone in their 1-D mathematical model and predicted metal front velocity. The predicted metal front temperature and velocity showed accurate agreement with their experimental measurements. Since the model assumed the foam degradation velocity was based a constant heat transfer coefficient and one-dimensional Bernoulli's equation was used to solve the metal flow field, it was impossible to apply the model to complex geometry casting problems.

Recently, Mirbagheri *et al.* (2003, 2004) developed a foam degradation model with a pressure correction scheme for the free surface at the metal front based on the numerical technique of SOLA-VOF. The governing equations were discretized and solved by finite difference method. A similar back-pressure force scheme was adopted by Kuo *et al.* (2003) in the momentum equation and the value of this force was adjusted to study the filling sequence of patterns according to experimental results. Most of these simulations predict a much slower filling speed for LFC process than that of traditional sand casting process. But the role of foam degradation is mostly not a part of the models, and experimental data or empirical functions are needed to perform simulations. Additionally, these models were all based on the finite difference method which has a limited capability to treat complex geometries even with a refined stepwise grid system. This method usually approximates the complex geometries in a zigzag fashion which can significantly reduce the accuracy of the simulations. This method imposes very heavy loads on computer memory and CPU time if high accuracy is required.

To summarize, the existing numerical models of LFC process have some disadvantages:

- Not adequate to simulate the process by only conduction heat transfer and Bernoulli equations
- Boundary conditions need to be considered more realistically
- Model should allow efficient applications to complex geometries
- Lack of the capability to predict casting defects
- Limited benchmark experimental data

FLOW3D® is a commercial computational fluid dynamics (CFD) program developed from the SOLA-VOF algorithm and fractional area/volume ratios (FAVOR) method. It is capable of simulating the lost foam casting process for any complex-shaped geometry. A full set of coupled continuity, momentum and energy equations together with the free surface boundary conditions are solved. A special defect-tracking scheme is also developed and implemented in the LFC model. Successful simulation has been validated with experiments on a one-gate General Motor test box for the lost foam casting process (Hirt and Barkhudarov, 2002). The shortcoming is that metal flow velocity is assumed to be a linear function of heat transfer coefficient between the metal front and foam pattern, which is set as a constant in the code. From the measurement as discussed in Chapter 4, the interfacial heat transfer coefficient actually is varying during the casting process. Additionally gas pressure in the kinetic zone, which is an important parameter to the LFC, is not considered in the model.

1.8 Objective of This Study

The current research aims to investigate the heat and mass transfer phenomena between the metal front and the foam pattern experimentally and develop better models to describe the process. Flow visualization is used to monitor the metal and foam interaction. Heat flux and heat transfer coefficient at the metal front are measured. The experiment is also designed to study the pressure development between the foam pattern and the molten metal. With better understanding of the physical process of foam degradation at the metal front, a computational fluid dynamics model is developed to incorporate the kinetic zone into the existing simulation model in FLOW-3D. The primary variables in the study are metal front velocity, foam pattern density and coating thickness.

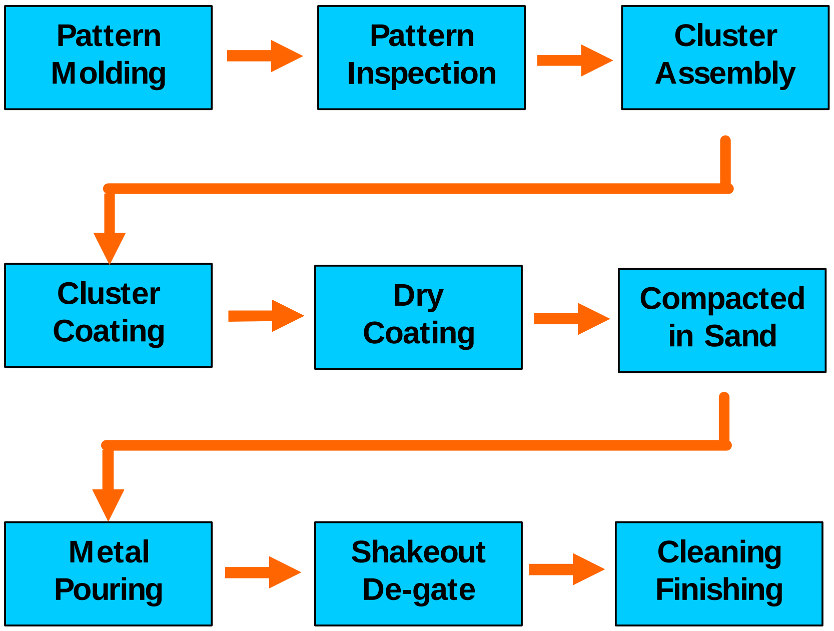
Pattern Molding
Pattern Inspection
Cluster Assembly
Cluster Coating
Dry Coating
Compacted in Sand
Metal Pouring
Shakeout De-gate
Cleaning Finishing

Figure 1.1 Flow chart for the lost foam casting process

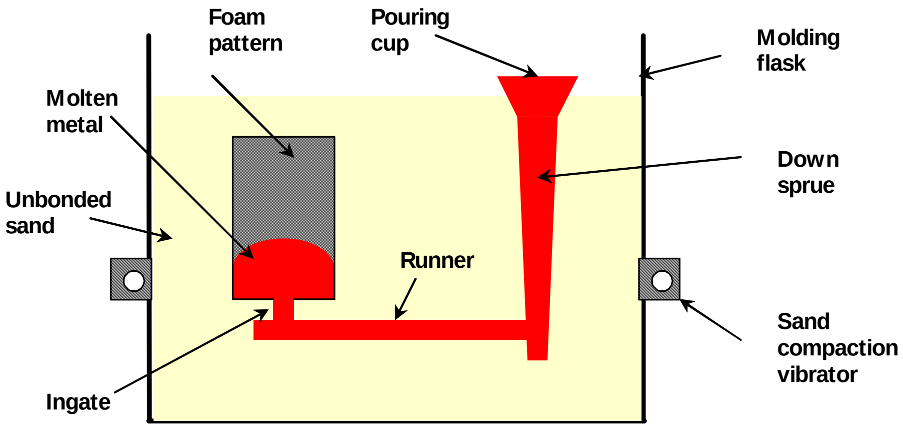
Foam pattern
Pouring cup
Molding flask
Molten metal
Down sprue
Unbonded sand
Runner
Sand compaction vibrator
Ingate

Figure 1.2 Schematic of molten metal pouring in the lost foam casting process

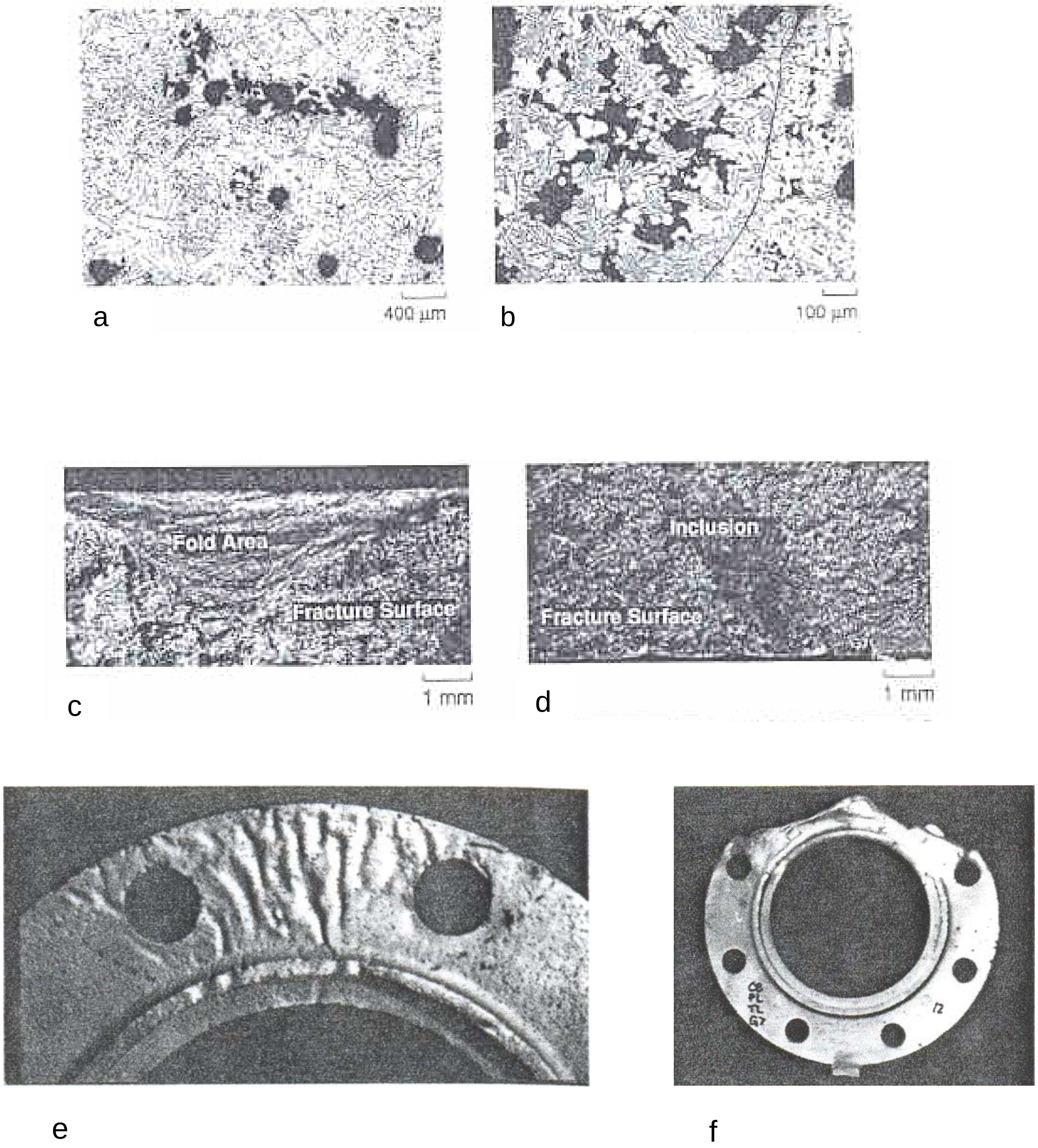
a
400 µm
b
100 µm
Fold Area
Fracture Surface
c
1 mm
Inclusion
Fracture Surface
d
1 mm
e
f

Figure 1.3 Photograph showing typical defects (a) surface porosity, (b) large amount of porosity at the metal front near a lap defect, (c) fold area on fracture surface, (d) inclusions on fracture surface, (e) surface collapse of a flange, and (f) misrun of a flange (Shivkumar *et al*., 1990; Hill *et al*., 1998)

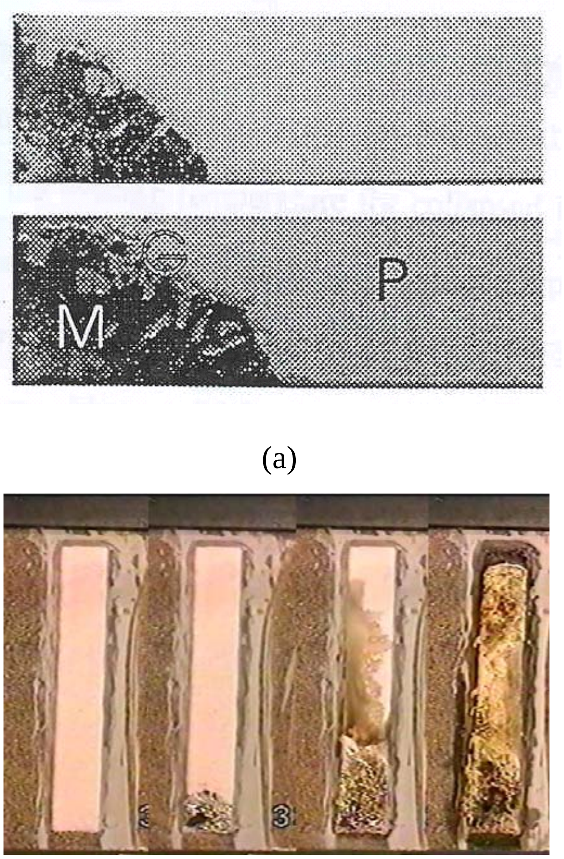

(a)

(b)

Figure 1.4 Visualization results (a) Yao’s (1994) images (M, G, P represents the metal, gas layer, and the polymer pattern) (b) Liu (2001) observation showed a gas zone more than 5 cm wide

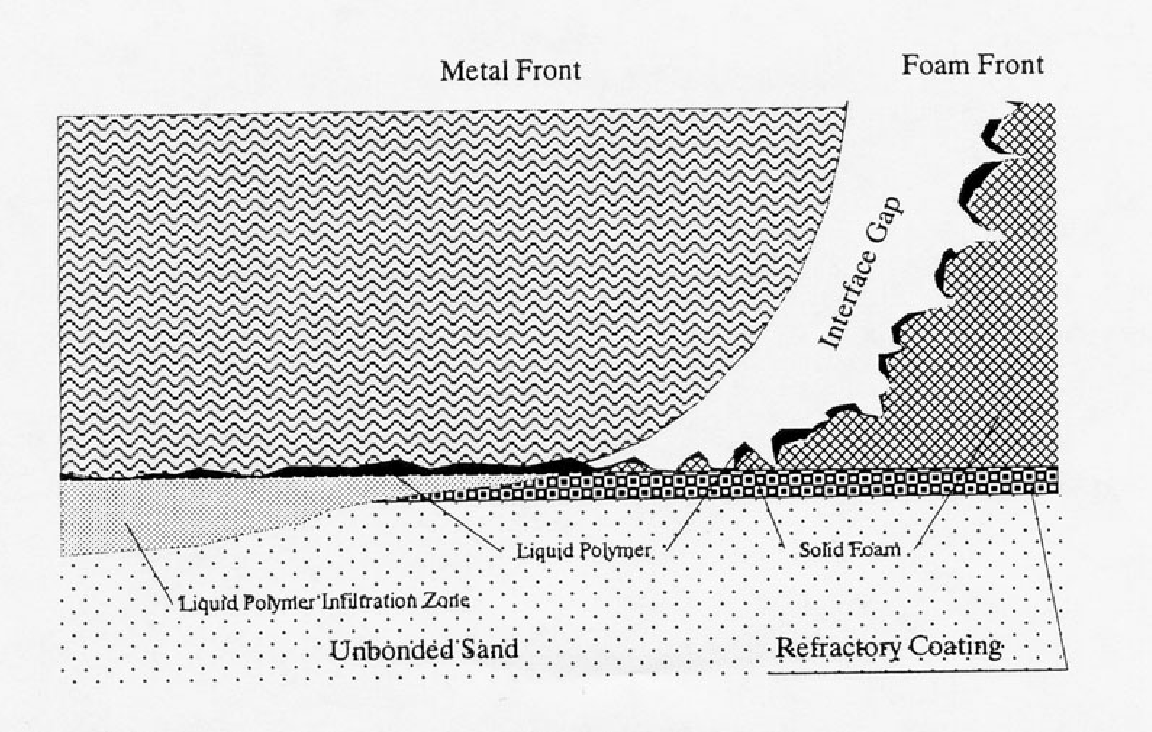
Metal Front
Foam Front
Interface Gap
Liquid Polymer
Solid Foam
Liquid Polymer Infiltration Zone
Unbonded Sand
Refractory Coating

Figure 1.5 Model with an interface gap (kinetic zone) for the lost foam casting process (Liu *et al*., 1997)

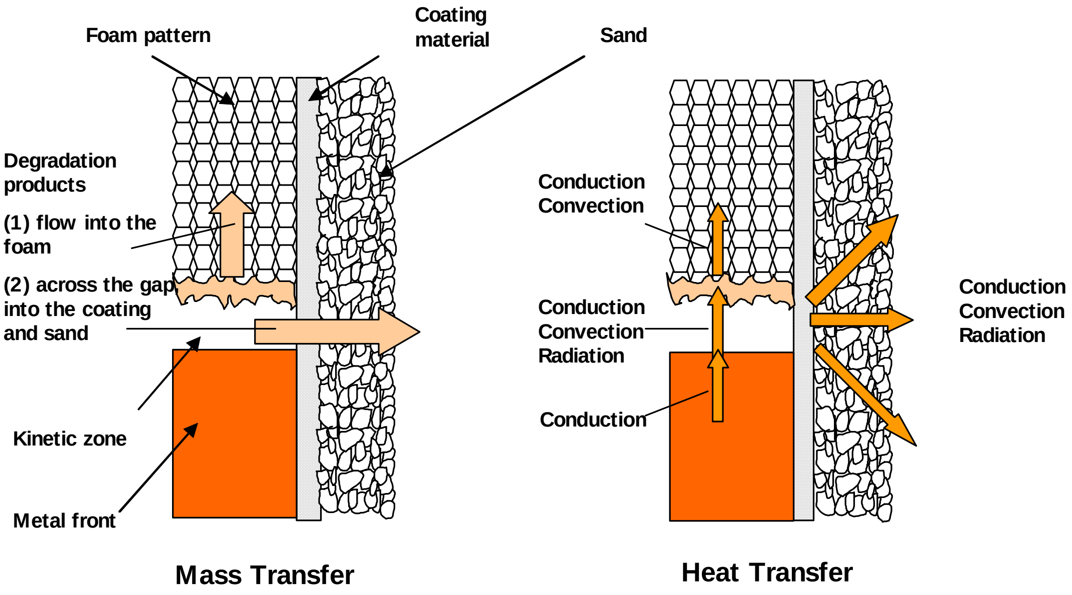
Foam pattern
Coating material
Sand
Degradation products
(1) flow into the foam
(2) across the gap into the coating and sand
Kinetic zone
Metal front
Mass Transfer
Conduction
Convection
Conduction
Convection
Radiation
Conduction
Conduction
Convection
Radiation
Heat Transfer

Figure 1.6 Heat and mass transfer processes in the kinetic zone (Warner *et al.*, 1998) between the advancing metal front and foam pattern

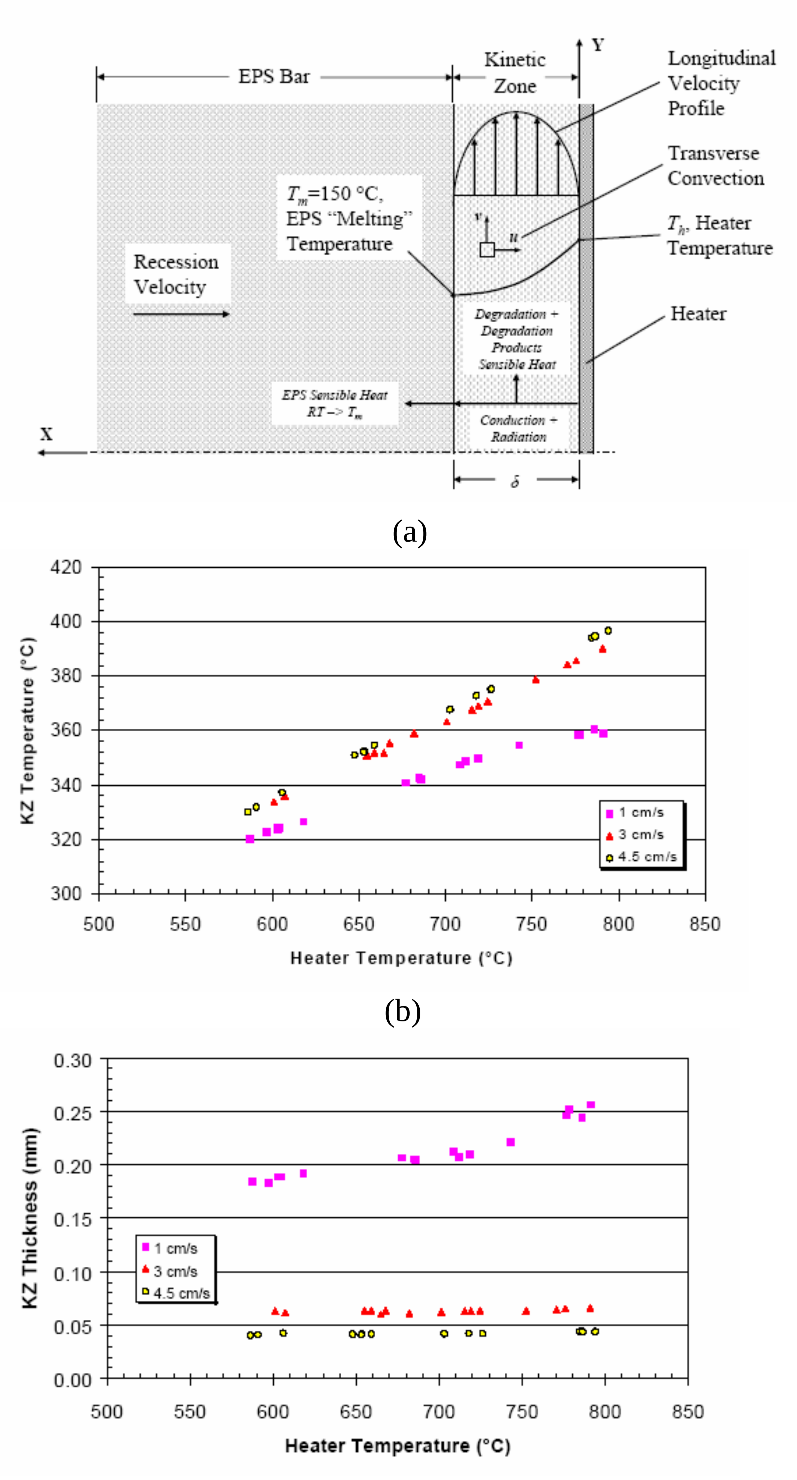

(a)

(b)

(c)

Figure 1.7 (a) Kinetic zone model from Molibog (2002). EPS = expanded polystyrene; RT = room temperature, (b) Predicted temperature of kinetic zone, and (c) predicted kinetic zone thickness

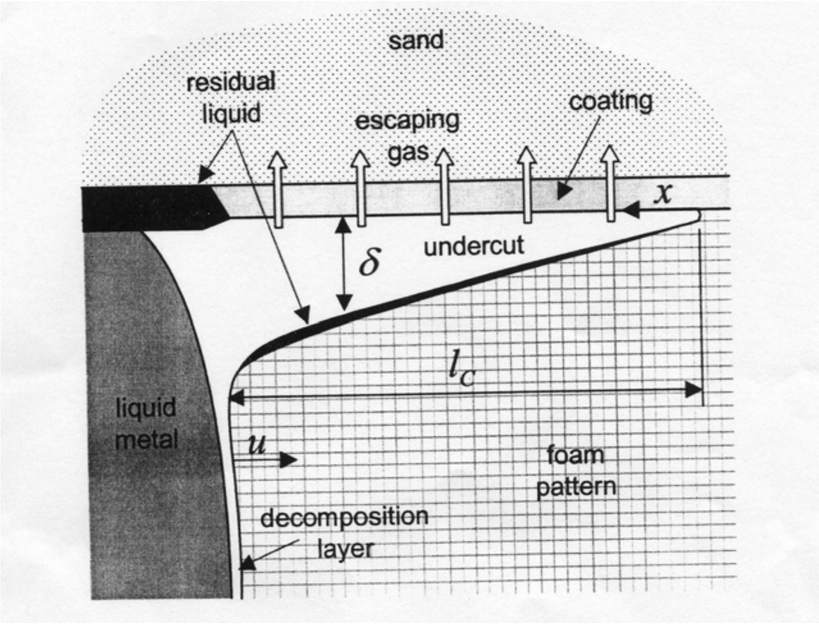
sand
residual liquid
escaping gas
coating
x
δ
undercut
l_c
liquid metal
u
foam pattern
decomposition layer

Figure 1.8 Undercut model between the metal front and foam pattern proposed by Barone and Caulk (2005)

CHAPTER 2 EXPERIMENTAL SETUP AND PROCEDURE

The present experimental study was conducted in two stages. First, a visualization experiment using a cylindrical quartz window with simulated metal front moving upwards was built to visualize the process and make necessary measurements. The second phase involved conducting similar experiments on a realistic fully coated foam pattern with the metal front moving from top to bottom. Additionally, visualization is performed in the second phase with metal front moving from top to bottom. Temperatures in the metal front and foam pattern were recorded during the process together with pressure measurements between the foam pattern and the metal front.

2.1 Visualization Experiment

An experimental system using a cylindrical quartz window and heated steel block was set up to make measurements and visualize the process (Figure 2.1(a)). A 60° arc section was cut from a quartz tube of 9 cm inside diameter and 0.25 cm thickness. The cylindrical quartz window was positioned in the rectangular open area (4.6 cm × 30 cm) of a 38 cm diameter cylinder steel flask 50 cm high as shown in Figure 2.1(b). The picture of the experimental set-up is shown in Figure 2.2(a). A front view of the set-up is shown in Figure 2.2 (b).

In the experiment, a heated steel block was used to simulate the molten metal front. By using this method, the most important parameter in LFC – metal front velocity can be controlled to simulated different operating conditions. There were 6 holes of 1.6 cm diameter evenly drilled through the steel block and a 1700 W cartridge heater was inserted in each of the holes. The design of steel block with heaters and cylinders with supporting part is shown in Appendix G. An engine piston was mounted on the bottom end of the steel block and piston rings were used to seal the system to prevent the egress of gaseous degradation products, as shown in Figure 2.3.

The piston was connected to an electric cylinder and motor which facilitated the controlled movement of the steel block. The electric cylinder is Model ETS32-B08LA20-FM300-A with 300 mm stroke from Parker Hannifin Corporation, Wadsworth, Ohio. The step motor is NEMA 23 P/N 5618L-0502 with step motion control system P/N SID 2.0 FHNL from TMG the Motion Group, Clovis, California. The system moves longitudinally 0.3175 mm in 200 rotations. Accurate position and velocity can be controlled precisely by computer running the QBasic program. The section of the QBasic program that needs to be modified is listed in Appendix E. The R value in line 510 of Appendix E can be adjusted to generate the desired speed according to the table in Appendix F.

Three 0.15 cm wire diameter chromel-alumel (K-type) thermocouples (±0.4% full scale) were embedded longitudinally from the surface of the steel block, as shown in Figure 2.3. The diameter of the steel block is 86 mm, which left a 1 mm clearance in the radial direction for the foam pattern. Considering the thermal expansion of the steel block, the actual clearance between the steel block and foam pattern is less than 0.5 mm. The small clearance minimizes the escape of the gaseous products and at the same time permits unconstrained movement of the simulated metal front. Since piston rings are used to seal the system at the bottom of the steel block, the escape of gaseous products is minimal. The first thermocouple A is 2.5 mm from the surface and 25 mm from thermocouple B. Thermocouple B and C are 25 mm from the each other. The radial distance of the thermocouple is 36 mm from the center of the cylindrical steel block.

A National Instruments data acquisition system using a PCI-MIO-16XE-50 data acquisition card, SCXI-1100 multiplexer amplifier, SCXI-1000 conditioning chassis, and Labview® software was used to record the pressure and temperature at a rate of five hundred samples per second. Every one hundred scans are averaged, yielding five recorded pressure and temperature measurements per second from each pressure transducer and thermocouple. The Labview® interface is shown in Appendix D.

Foam patterns were supplied by Foseco Inc. The EPS foam patterns tested have densities of 24 kg/m^3 and 27 kg/m^3. A copolymer (70%EPS and 30%PMMA) with a density of 25 kg/m^3 was also used in the experiments. Both types of foam patterns were 88 mm in diameter and 254 mm long as shown in Figure 2.4(a) for uncoated foam pattern. The foam patterns were dipped in commercial DCH Ashland refractory material with a 54.2% solid and density of 1570 kg/m^3. By controlling the water content of the coating material and the pattern dipping time, three different coating thicknesses were obtained: 0.2 mm, 0.7 mm and 1.2 mm.

In the visualization experiment, a 60° arc section of the foam pattern was covered with duct tape before it was dipped in the coating bath. The protective tape was removed later leaving a rectangular open area (46 mm × 254 mm) for visualization. In the visualization experiment, 16% of the surface area of the foam pattern is left uncoated for observation through the quartz glass window as shown in Figure 2.4(b).

The coated foam pattern was placed in the upper steel flask and then sand was filled around the foam pattern and compacted manually to produce the desired closely packed mold. The uncoated part of the foam pattern is in contact with the quartz glass window as shown in Figure 2.5. AFS30 Olivine sand was used, and it has 90% percent of the sand grain size less than 0.6 mm with the sieve curve shown in Figure 2.6. The properties of mold media were not a variable in this study.

The steel block was first heated to the desired temperature by the cartridge heaters. Then the motor was started and electric cylinder moved the steel block at a predetermined constant velocity. Velocities of 0.36 cm/s and 0.44 cm/s were set in the experiments. The foam patterns went through the degradation process and were replaced by the advancing metal. Images of the process were recorded through the quartz window. This experimental set-up was used primarily to record the size of the gap between the metal front and the foam.

2.2 Realistic Top-down Experiment

During initial experimentation, it was noted that if the simulated metal front was moved faster than a certain velocity, the steel block pushed the foam pattern against the sand, disturbing the original position of the foam pattern. To allow a higher velocity in the range recommended by Hill *et al.* (1998) for aluminum lost foam casting, a realistic top-down experiment was built to move the steel block downwards.

The instrumentation set-up for this configuration was almost similar to that of the visualization process, except for a few modifications which were made in the foam pattern coating and the direction of simulated metal front movement. Figure 2.7(a) shows the schematic diagram of the experimental set-up for the realistic top-down experiment.

The two important features of this segment of the study are the full coating of foam patterns and the higher velocity at which the simulated metal front can move. The foam patterns and coating materials were the same as those used in the visualization experiment, but there was no uncoated part left for visualization. In this way the effect of quartz window on the foam degradation process was eliminated. The velocities of the metal front were set at 0.95 cm/s, 1.5 cm/s and 1.9 cm/s in addition to the lower velocities of 0.36 cm/s and 0.44 cm/s used in the visualization experiments. This experimental set-up was used to record pressures and temperatures as a function of various process variables.

2.3 Measurement of Heat Flux and Heat Transfer Coefficient

The surface temperature and temperature gradient at the metal front were calculated from the readings from thermocouples A, B, and C which were located near the surface of the steel block shown in both Figure 2.3 and 2.7. The temperature and size of the kinetic zone were measured using four additional thermocouples D, E, F, and G which were embedded in the foam pattern shown in Figure 2.7(a) and (c). In order to have a fast response time, the diameter of the bare chromel and alumel wires (K-type) was 0.025 cm with a bead diameter less than 0.08 cm. These thermocouples were also insulated using two-bore ceramic tubes to protect the wire near the bead tip from the high temperature of the advancing simulated metal front. All four thermocouples were placed in the foam pattern, 3.8 cm apart from each other. Thermocouple D was 6.4 cm from the top surface of the foam pattern.

Temperatures recorded in the steel block during the process provided an instantaneous axial temperature profile. This was used to provide a measure of surface temperature as well as the heat flux at the surface. The surface heat flux q_s can be calculated using Fourier's law by evaluating the temperature gradient at the surface and the thermal conductivity of the cylinder material (AISI 1018) at different surface temperatures (Davis, 1990):

$$q_s = -k \left. \frac{\partial T}{\partial x} \right|_s \tag{2.1}$$

where k is the metal thermal conductivity of the metal;

T is the temperature in the metal front;

x is the axial position from the metal front;

s represents the surface to the metal front.

The heat transfer coefficient h is then calculated by Newton's Law of Cooling:

$$h = \frac{q_s}{T_s - T_z} \tag{2.2}$$

where T_s is the metal front surface temperature;

T_z is the kinetic zone temperature.

In order to calculate the heat transfer coefficient, thermocouples embedded in the foam were used to measure the kinetic zone temperature. These thermocouples measurements were also used in conjunction with the pre-determined metal front velocity to measure the gap size as described below. As the metal front advances to replace the foam pattern, thermocouples D, E, F, and G were used to record the thermal history of the foam pattern at precisely determined locations and time instances. As shown in Figure 2.8, the foam around thermocouple D collapses when it reaches the collapse temperature of 120°C (Mehta *et al.*, 1995) at which point the time was noted as t_1. The temperature increases rapidly until the metal front makes contact with the thermocouple at time t_2. At the moment t_1 the gaseous gap size d is equal to the distance that the steel block traveled between t_1 and t_2 at the given velocity. The kinetic zone temperature is then calculated from the thermocouple readings between time t_1 and t_2.

2.4 Gas Pressure Measurement

A pressure hole was also drilled through the steel block through which a 1.6 mm I.D. brass tube was inserted as shown in Figure 2.3 and 2.7(a). A polyurethane pressure tube connected the brass tube to an Omega PX800 high accuracy and fast response pressure transducer from Omega Engineering, Inc., Stamford, Connecticut. The pressure transducer has an accuracy of ±0.1% best-fit straight line (BFSL) and the pressure range is 0 to 20 kPa. The calibration curve is shown in Figure B.1 in Appendix B. The pressure in the gaseous gap between the simulated metal front and the foam pattern could be measured in real time by using the pressure tube P.

In addition to the pressure tap installed through the steel block which is noted as P in Figure 2.7(a), three other pressure taps noted as P1, P2 and P3 in Figure 2.7 (a) and (b) were positioned in the foam pattern in order to verify the pressure measurement by pressure tap P. Pressure readings from P give the complete pressure development in the kinetic zone during the foam degradation process, and readings from P1, P2 and P3 provide local pressure information before the metal front touches the pressure taps. Omega PX70 transducers were used to measure the pressures from P1, P2 and P3. These transducers have a linearity of ±0.5% FS and a repeatability of ±0.3% FS with a pressure range of 0 to 15 kPa. A typical calibrations curve is shown Figure B.2 in Appendix B.

2.5 Experimental Procedure

At beginning of every experiment, the foam pattern was drilled at precise locations to position the thermocouples and pressure transducers. To prevent gas leak through the connection between the coating and the transducers, hot plastic glue was applied around the connection to perform the sealing. Then the foam pattern was placed in the sand flask in alignment with the simulated metal front. Loose sand was poured around the foam pattern with manual compaction. Before the power of heater controller was turned on, the simulated metal front was moved along the glide about 30 cm away from the foam pattern. Then a piece of ceramic plate was palced between the foam pattern and the metal front to prevent the foam being preheated by the heaters. Thermocouple C was connected to the temperature controller as an input control. The temperature controller Series 93 from Watlow Controls, Winona, Minnesota is shown in Figure 2.9. The controller can automatically tune the system to reach desired temperature.

After the pre-set temperature was reached, the power of the heaters was shut down. Then thermocouple C was switched to the data acquisition system to record temperature together with other thermocouples. The insulating ceramic plate was then removed and the heated steel block was positioned along the foam pattern. As soon as the simulated metal front was aligned well with the foam pattern, a signal sent from the computer to the motor controller started the movement of the steel block. The foam decomposition process started and metal front advanced to replace the foam pattern. At the same time, Labview® software recorded the data from thermocouples and pressure transducers. In the visualization experiment, Video cameras were also used to record the foam degradation process

2.6 Analysis of Variance (ANOVA) F-Test

The Analysis of Variance (ANOVA) F-Test provides statistical information about effect of various parameters in the observed data. Process parameters, also known as factors in ANOVA, can have several different levels of values. For example in the experiment, factors may include density of foam pattern, coating thickness and velocities of the simulated metal front. Density of EPS foam pattern has two levels which are 24 kg/m^3 and 27 kg/m^3. Coating thickness has three levels which are 0.2 mm, 0.7 mm and 1.2 mm. Metal front velocity has three levels which are 0.44 cm/s, 0.95 cm/s and 1.5 cm/s. Combinations of different factors and levels can have various effect on a particular response. ANOVA can then be used to provide statistical information on the significance of different factors.

The major assumption in ANOVA is that the monitored responses are randomly obtained and have a normal distribution. The data collected are then analyzed by two different statistical models. A full model is a model that is used to adequately describe the data with separate means for each group of data. A reduced model is a special case of the full model obtained by assuming equal means for all the groups. By applying the two models, a residual can be calculated as the observation value minus its estimated mean, and the residual sum of squares is the summary of the residuals for a particular model.

The difference between the residual sum of squares for reduced model and that for full model is the extra sum of squares. From these residual sums of squares and the respective degree of freedom, the F-value can then be calculated

$$F = \frac{[SSR(reduced) - SSR(full)]/[dof(extra)]}{SSR(full)/dof(full)} \tag{2.3}$$

where *SSR(reduced)* represents sum of squares for the reduced model;

SSR(full) represents sum of squares for the full model;

dof(extra) is the extra degree of freedom;

dof(full) is the degree of freedom for the full model.

The F-value can be used to analyze the significance of the particular factor and the combination of several factors if it is desired. Ramsey and Schafer (2002) presented a detailed description of the ANOVA analysis and Anderson and Whitcomb (2000) provided software to carry out the computations.

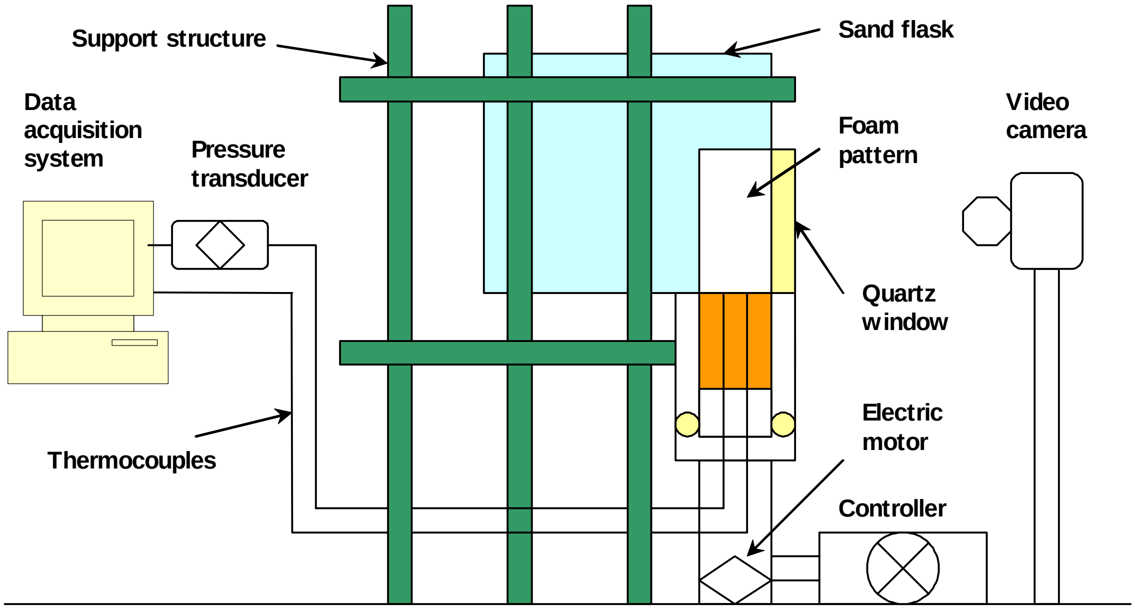
Support structure
Sand flask
Data acquisition system
Pressure transducer
Foam pattern
Video camera
Quartz window
Electric motor
Thermocouples
Controller

(a)

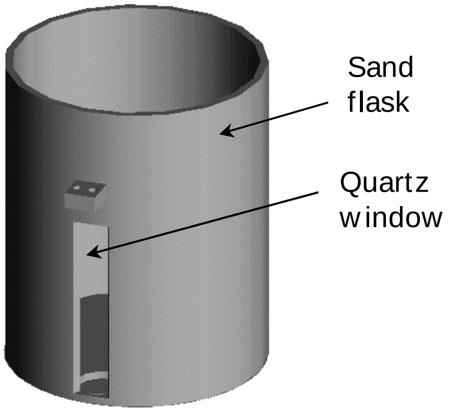
Sand flask
Quartz window

(b)

Figure 2.1 (a) Schematic of the visualization experiment set-up, and (b) Sand mold flask showing the visualization window

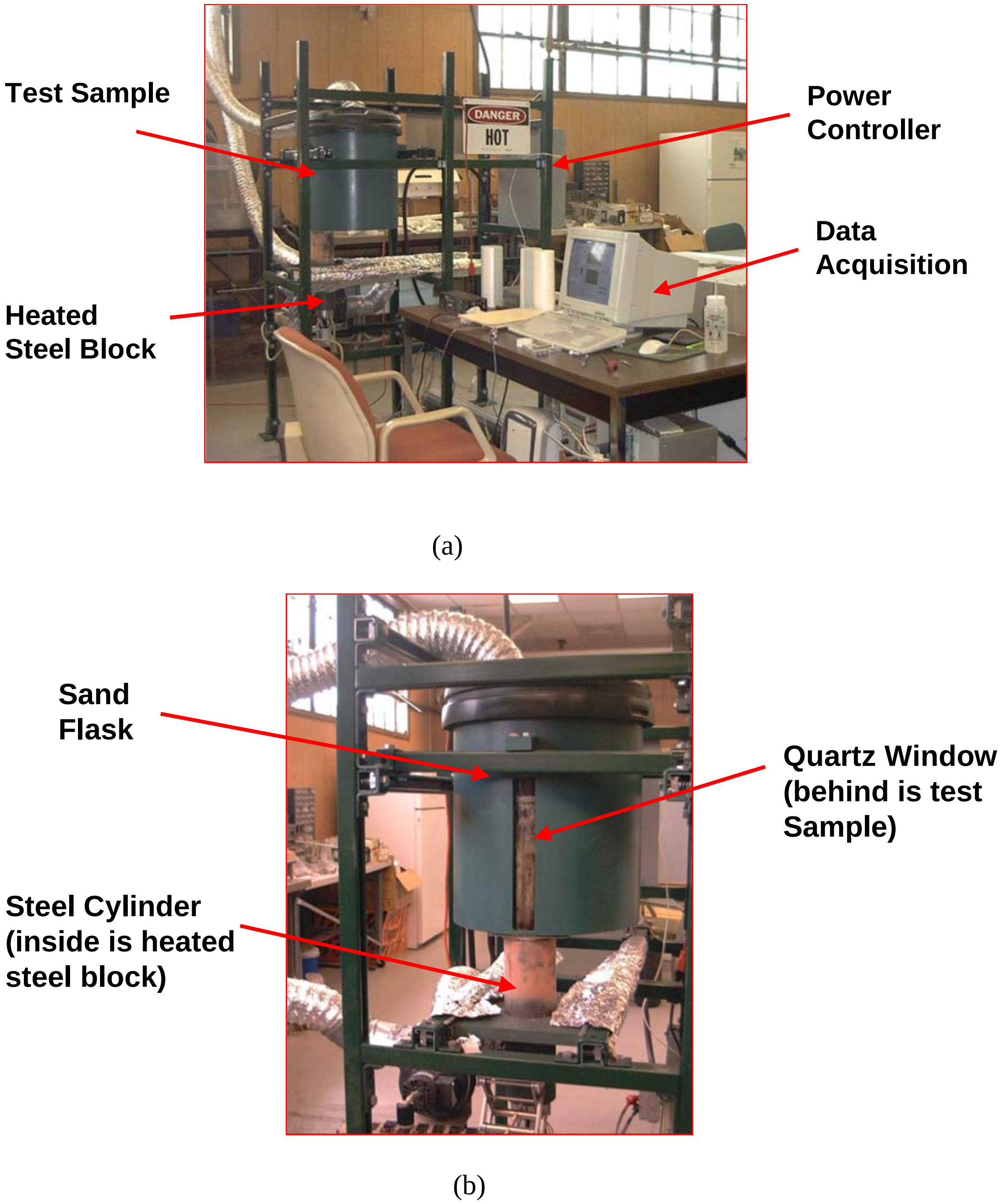
Test Sample
Power Controller
Data Acquisition
Heated Steel Block
DANGER
HOT
(a)
Sand Flask
Quartz Window (behind is test Sample)
Steel Cylinder (inside is heated steel block)
(b)

Figure 2.2 Picture of the visualization experiment set-up: (a) a view of overall set-up, and (b) the front view

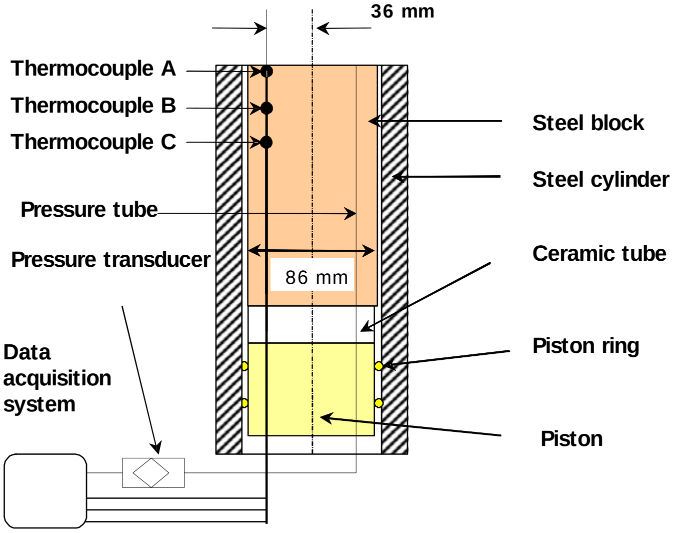
36 mm
Thermocouple A
Thermocouple B
Thermocouple C
Pressure tube
Pressure transducer
86 mm
Data acquisition system
Steel block
Steel cylinder
Ceramic tube
Piston ring
Piston

Figure 2.3 Instrumented steel block that simulates the molten metal front in the visualization experiment

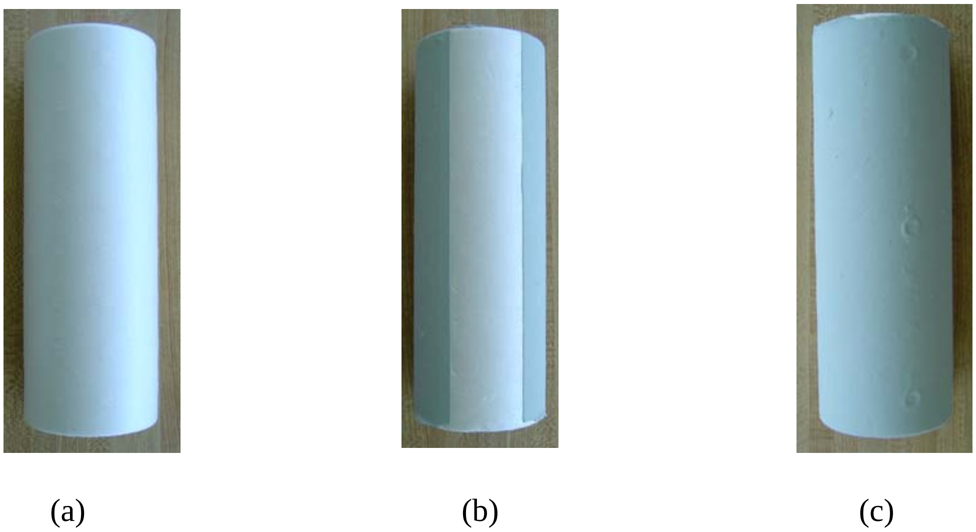

Figure 2.4 Expanded polymer patterns: (a) uncoated, (b) coated with visualization window left uncoated, and (c) fully coated

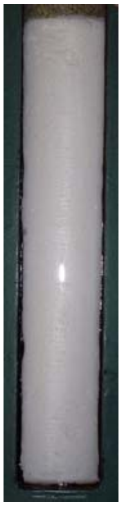

Figure 2.5 The uncoated part of the foam pattern is in contact with the quartz glass window in the visualization experiment

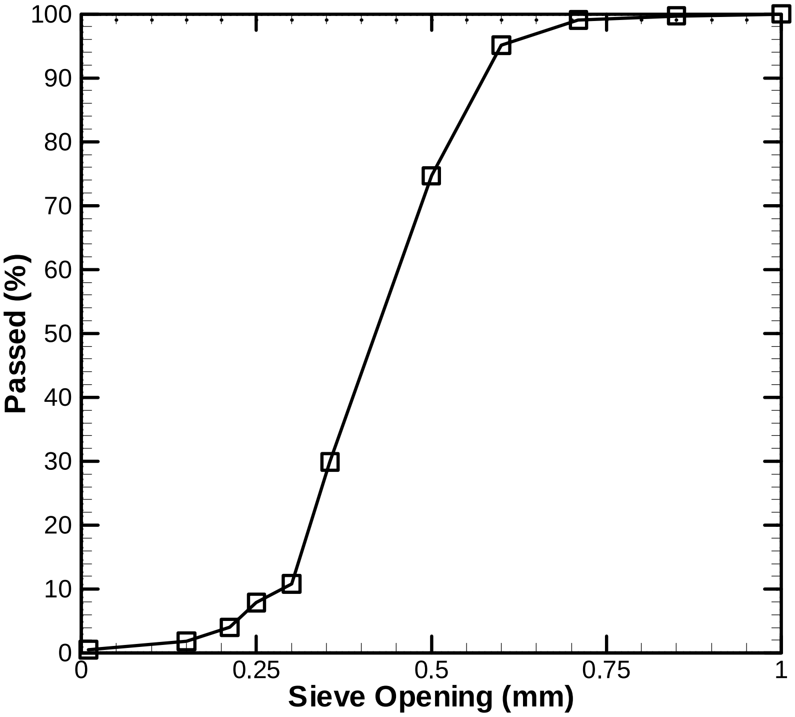

Figure 2.6 Sieve curve of the Olivine sand ASF30 used in experiment

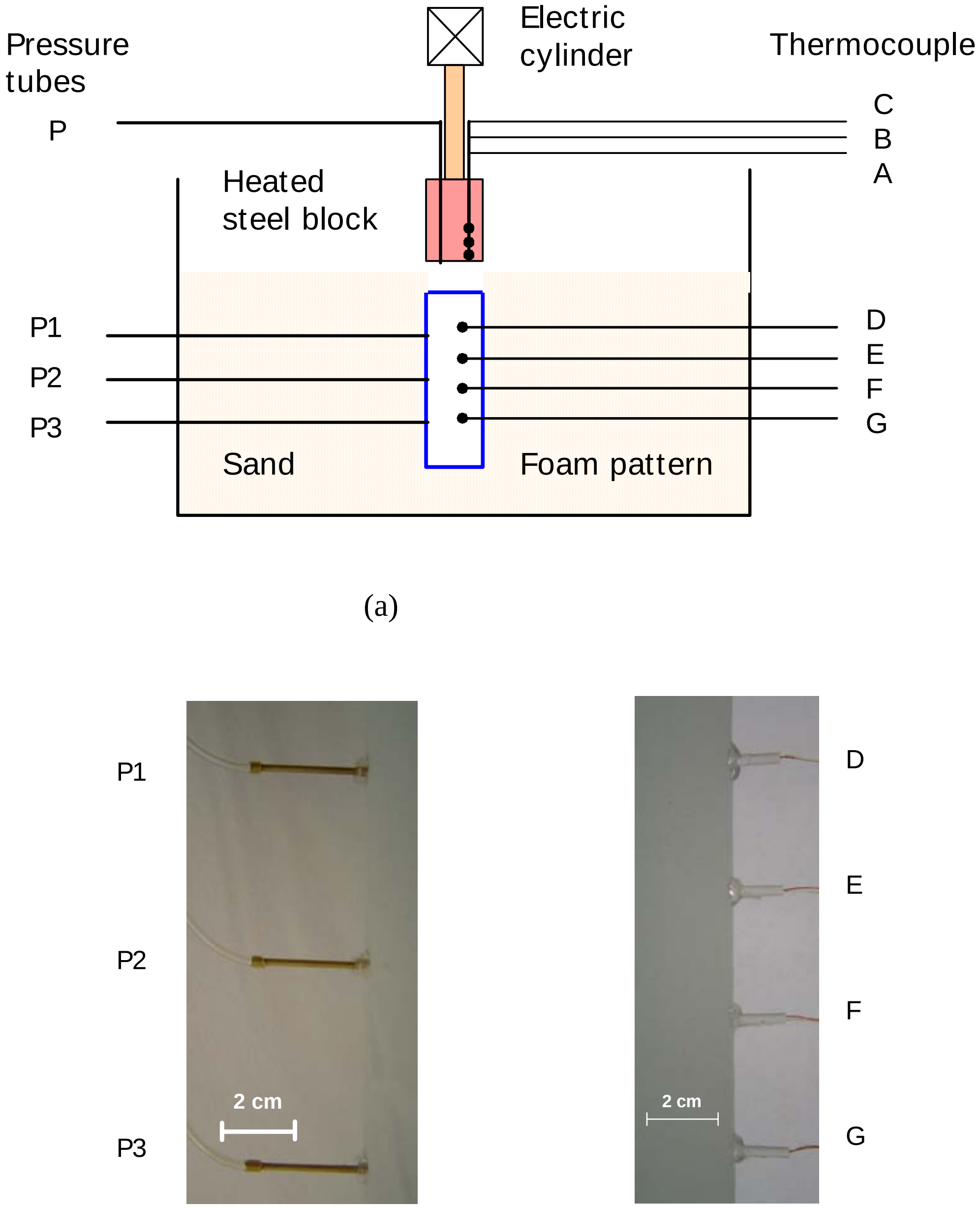
Pressure tubes
P
Electric cylinder
Thermocouple
C
B
A
Heated steel block
P1
P2
P3
D
E
F
G
Sand
Foam pattern
P1
P2
2 cm
P3
2 cm
D
E
F
G

(a)

(b) (c)

Figure 2.7 (a) Schematic of experiment set-up for the realistic top-down arrangement showing pressure and temperature measurement locations, (b) picture showing the pressure taps and tubes in the foam pattern, and (c) picture showing the temperature sensors in the foam pattern

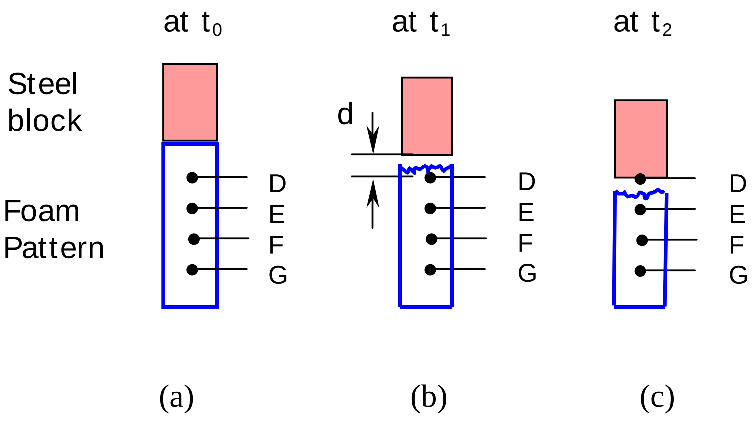
at t_0
at t_1
at t_2
Steel block
Foam Pattern
d
D
E
F
G
(a)
(b)
(c)

Figure 2.8 Position of simulated metal front and foam pattern at different time instances: (a) initial position, (b) at time t_1 the foam around thermocouple D begins to collapse when it reaches collapse temperature, and (c) at time t_2 the metal front reaches thermocouple D resulting in a very rapid rise in temperature

WATLOW
93
93.0
93.0

Figure 2.9 Watlow Series 93 microprocessor-based auto-tuning temperature control

CHAPTER 3 NUMERICAL MODELING

Successful computer simulations can help reduce the number of trials and cut down the lead time in the design of new casting products by better understanding the complex mechanisms and interplay of different process parameters in the foam decomposition process. In this chapter, an existing computational fluid dynamics (CFD) model has been improved to simulate the fluid flow of molten aluminum and the heat transfer involved at the interfacial gap between the metal and the foam pattern. The commercial code FLOW-3D® was used because it can track the front of the molten metal and solve the governing equations efficiently by a SOLution Algorithm − Volume of Fluid (SOLA − VOF) method and allow complex geometries to be captured easily by the Fractional Area/Volume Obstacle Representation (FAVOR) method. The code was modified to include the effects of varying interfacial heat transfer coefficient based on gaseous gap pressure which is related to foam degradation and coating permeability. The modification was validated against experimental data and the comparison showed improved agreement compared to the original model. Process parameters such as initial metal temperature, foam pattern property, and gating system were varied. The defect prediction model was also used to study the dependence of defect formation on the process variables.

3.1 Fractional Area/Volume Obstacle Representation (FAVOR) Method

Both finite difference (finite volume) and finite element methods are used to solve casting simulation problems (Mirbaghri *et al.*, 2004, Kuo *et al.*, 2003, and Houzeaux and Codina, 2004). The grid generation in the finite difference method is much easier because of the use of structured mesh and low storage requirements to describe the geometry as shown in Figure 3.1(a). The finite element method applies body-fitted computational grids which are a more accurate representation of the geometry as shown in Figure 3.1(b). However, body-fitted grids can be difficult to generate and it often takes more computational time. Additionally, solution accuracy degenerates in highly distorted grids.

Though the grid generation in conventional finite difference methods is much easier, it often requires fine grids to describe complicated geometry to reduce discretization error associated with the stair-step representation of curved boundaries. To overcome this limitation, an advantageous fractional area/volume obstacle representation (FAVOR) method was developed by Hirt (1993) and selected as the basis of grid generation for FLOW-3D®. Structured grid cells can be partially blocked by obstacles and the blockage is described by using fractional cell volumes and areas on cell sides in the FAVOR method as shown in Figure 3.2. The FAVOR method improves the accuracy of numerical solution on the boundaries with complex shape. Grids coarser than that in standard finite difference can be used to simulate practical engineering problems with arbitrary geometries which can be easily generated from CAD software as shown in Figure 3.3. Since the geometry representation is less mesh-dependent, the FAVOR method is also referred to as a free-gridding method. Results from grid independence study in Chapter 5 further illustrated the advantage of the FAVOR method.

For problems with moving fluid surfaces, complex flow regions at the interface need to be captured. Constructing good quality body-fitted grids is very difficult and time-consuming to establish workable grids. With the FAVOR method, complex fluid surfaces can be simulated by structured, smoothly varying, fast to generate, and strictly orthogonal grids with comparable accuracy of body-fitted grid methods. The FAVOR method combined with SOLA-VOF algorithm allows the use of coarser grids and improves the accuracy of the numerical solutions for complex geometries and fluid surface tracking which is a very important issue in modeling the LFC process.

3.2 Governing Equations

The fluid flow of molten metal during mold filling is characterized by a transient condition with a moving metal front surface. The mathematical model includes the continuity, momentum and energy equations in the molten metal, moving metal front and porous wall boundary conditions. The governing equations can be described as follows:

(a) Mass continuity equation:

$$\frac{\partial}{\partial x}(uA_x) + R\frac{\partial}{\partial y}(vA_y) + \frac{\partial}{\partial z}(wA_z) + \xi\frac{uA_x}{x} = 0 \tag{3.1}$$

where the velocity components (u, v, w) are in the coordinate directions (x, y, z) or (r, θ, z). A_x is the fractional area open to flow in the x direction, A_y and A_z are similar area fractions for flow in the y and z directions, respectively. The coefficient R depends on the choice of coordinate system in the following way. When cylindrical coordinates are used, ξ is set to unity, and y derivatives must be converted to azimuthal derivatives,

$$\frac{\partial}{\partial y} \to \frac{1}{r}\frac{\partial}{\partial \theta} \tag{3.2}$$

In FLOW-3D code this transformation is accomplished by using the equivalent form

$$\frac{1}{r}\frac{\partial}{\partial\theta}=\frac{r_m}{r}\frac{\partial}{\partial y} \tag{3.3}$$

where $y = r_m\,\theta$ and r_m is a fixed reference radius. The transformation given by Equation (3.3) is particularly convenient because its implementation only requires the multiplier $R = r_m/r$ on each y derivative in the original Cartesian coordinate equations. When Cartesian coordinates are to be used, R is set to unity and ξ is set to zero.

(b) Momentum equations:

$$\frac{\partial u}{\partial t}+\frac{1}{V_f}\left\{uA_x\frac{\partial u}{\partial x}+vA_yR\frac{\partial u}{\partial y}+wA_z\frac{\partial u}{\partial z}\right\}-\xi\frac{A_yv^2}{xV_f}=-\frac{1}{\rho}\frac{\partial P}{\partial x}+G_x+F_x \tag{3.4}$$

$$\frac{\partial v}{\partial t}+\frac{1}{V_f}\left\{uA_x\frac{\partial v}{\partial x}+vA_yR\frac{\partial v}{\partial y}+wA_z\frac{\partial v}{\partial z}\right\}+\xi\frac{A_yuv}{xV_f}=-\frac{1}{\rho}R\frac{\partial P}{\partial y}+G_y+F_y \tag{3.5}$$

$$\frac{\partial w}{\partial t}+\frac{1}{V_f}\left\{uA_x\frac{\partial w}{\partial x}+vA_yR\frac{\partial w}{\partial y}+wA_z\frac{\partial w}{\partial z}\right\}=-\frac{1}{\rho}\frac{\partial P}{\partial z}+G_z+F_z \tag{3.6}$$

where (G_x, G_y, G_z) are body acceleration (forces per unit mass), (F_x, F_y, F_z) are viscous forces per unit mass.

(c) Fluid energy equation

$$V_f\frac{\partial}{\partial t}(\rho I)+\frac{\partial}{\partial x}(\rho IuA_x)+R\frac{\partial}{\partial y}(\rho IvA_y)+\frac{\partial}{\partial z}(\rho IwA_z)+\xi\frac{\rho IuA_x}{x}=TDIF \tag{3.7}$$

where I is the macroscopic mixture internal energy, $TDIF$ is heat diffusion term and it is

$$TDIF=\frac{\partial}{\partial x}\left(kA_x\frac{\partial T}{\partial x}\right)+\frac{\partial}{\partial y}\left(kA_y\frac{\partial T}{\partial y}\right)+\frac{\partial}{\partial z}\left(kA_z\frac{\partial T}{\partial z}\right)+\xi\frac{kA_xT}{x} \tag{3.8}$$

where k is the thermal conductivity of the fluid.

3.3 SOLution Algorithm and Volume-of-Fluid (SOLA-VOF) method

SOLA-VOF has been widely used in simulation of all types of casting problems, and it has been shown to be more effective in solving transient moving surface problems than (Duff, 1999). FLOW-3D® also used this methodology to simulate the LFC process with adjustable time steps to improve efficiency, accuracy and stability.

Fluid configurations are defined in terms of a volume of fluid (VOF) function, *F(x,y,z)*. This function represents the volume of fluid per unit volume and satisfies the equation

$$\frac{\partial F}{\partial t}+\frac{1}{V_f}\left\{\frac{\partial}{\partial x}\left(FuA_x\right)+R\frac{\partial}{\partial y}\left(FvA_y\right)+\frac{\partial}{\partial z}\left(FwA_z\right)+\xi\frac{FA_x u}{x}\right\}=0 \tag{3.9}$$

The *F(x,y,z,t)* represents the volume fraction occupied by the fluid. The VOF method consists of three main components:

- A fluid fraction function *F(x,y,z,t)* which is equal to 1.0 in fluid regions, and equal to 0.0 in voids. On the interface region, *F(x,y,z,t)* is between 0 and 1 as shown in Figure 3.4.
- On the interface zero shear stress and constant pressure boundary conditions are applied.
- A special advection algorithm is used to track a sharp interface.

FLOW-3D® calls it Tru-VOF® if all the three parts are implemented in the calculation. In the past several years, a number of commercial CFD programs have claimed a VOF capability, when in reality they are only implementing one or two of the three VOF ingredients which often lead to incorrect results (Flow Science, Inc.).

In the main computation with the SOLA-VOF method, there are seven basic steps for the solution algorithm as follows.

Step 1: Guess initial pressure field.

Step 2: Compute velocity field from momentum equation.

Step 3: Solve Poisson equation resulting from the continuity equation to calculate pressure change for molten metal, and find velocity based on metal front model for foam-metal interface.

Step 4: Correct pressure and velocity due to change in pressure.

Step 5: Repeat step 3 and 4 until continuity is satisfied.

Step 6: Update remaining variables using new velocities.

Step 7: Move to next time cycle until desired time interval is reached.

3.4 Overall Solution Procedures

There are three parts of the whole computing process to solve any CFD problems by using FLOW-3D® computational codes:

1. Pre-Processing, which includes input of
    a. Control parameters of mathematical and numerical models
    b. Properties of fluids and obstacles
    c. Geometry and meshing
    d. Boundary and initial conditions
    e. Control parameters for output
2. Main computation with SOLA-VOF method
3. Post-Processing which include

a. Data plotting
b. Flow animation
c. Text file output
d. Customized data probe and printing

3.5 Basic Model of Metal Front Velocity with Gravity Effect

Flow of molten metal in the LFC casting process is different from traditional sand casting because of the boundary conditions at the metal front. The free surface condition usually used in traditional sand casting needs to be modified in the simulation the LFC process because of the existence of foam patterns in front of molten metal instead of air or a void in traditional sand casting. The boundary conditions at the wall also need to incorporate the effect of coating materials outside of the foam pattern. This coating layer provides strength required to support the pattern from collapsing while the foam is disappearing at the metal front and before the metal is solid enough to retain its shape. This is especially important if temperature of the molten metal is high and the permeability of the coating layer is low. Additionally the coating layer builds up insulation to prevent the metal front from losing too much heat and prematurely solidifies which results in cold shut defects in castings.

The metal front velocity is a function the heat absorbed by the foam, which depends not only on the properties of EPS foam and molten metal, but also on the process variables such as temperature of the metal, pressure head, coating materials, orientation of gravity, and metal front velocity itself. To find the metal front velocity, let q_s be the heat transfer rate from metal front to the kinetic zone. Then from Newton's Law of Cooling, we have

$$q_s = h(T_s - T_z)A_c \tag{3.10}$$

where h is the heat transfer coefficient at the metal front;

T_s is the metal front surface temperature;

T_z is the kinetic zone temperature;

A_c is the cross-section area of metal front.

The energy required by the foam pattern to get liquefied, vaporized and depolymerized can be expressed as

$$q_f = \dot{m}c_p(T_s - T_z) + \dot{m}Q_{liq} + \dot{m}Q_{vap} + \dot{m}Q_{depoly} \tag{3.11}$$

where q_f is the surface heat flux to the foam;

c_p is the polymer foam specific heat;

T_z is the initial foam temperature;

Q_{liq} is the latent heat of fusion of foam;

Q_{vap} is the heat of vaporization;

Q_{depoly} is the heat of depolymerization;

And the mass flow rate is

$$\dot{m} = \rho A_c V_{adv} \tag{3.12}$$

where ρ is the polymer foam density;

V_{adv} is the metal front velocity.

An energy balance can be applied between q_s and q_f to find the metal front velocity,

$$V_{adv} = \frac{h(T_s - T_z)}{\rho\left(c_p(T_s - T_z) + Q_{liq} + Q_{vap} + Q_{depoly}\right)} \tag{3.13}$$

The treatment of the moving boundary conditions at the metal front is the most critical part of all the models of the LFC process. FLOW-3D uses a velocity approach which is based on a heat transfer coefficient model as shown in Equation (3.13). The model can also incorporate the effect of gravity orientation. It has been shown through X-Ray video that an upward moving front progresses slower than a downward moving front (Hirt, 1999).

The gravity effect is taken into account by a correction factor, which is a function of gravity component normal to the metal/foam front. Because the foam decomposition products are usually lighter than the molten metal, the foam products can be displaced by the metal moving along the gravity direction and accumulate above the metal front that is moving against gravity direction. In FLOW-3D® the correction factor is defined as

$$f_g = sign(g_{ht}) \cdot c_g \cdot \left(\frac{V_g}{V_g + V_{ht}}\right) \tag{3.14}$$

where g_{ht} is the gravity component normal to metal/foam front;

c_g is gravity factor which can be tuned to get agreement with data;

V_{ht} is the nominal velocity of the metal front, which is

$$V_{ht} = \frac{h}{\rho c_P} \tag{3.15}$$

V_g is the characteristic speed of gravity waves, which is defined as

$$V_g = \sqrt{|g_{ht}| \cdot r_s} \tag{3.16}$$

where r_s is the characteristic length scale of the surface irregularities at the metal/foam interface. A value of 0.1 cm is recommended in the user's manual of FLOW-3D®.

3.6 Improved Model

3.6.1 Effect of Gas Pressure

A constant heat transfer coefficient is used in the basic LFC model in FLOW-3D®. Since an increasing heat transfer coefficient is observed in the present experimental study described in Chapter 4 and Liu *et al.* (2003), a model with varying heat transfer coefficient is needed to better model the process. The pressure of gas produced by the foam plays an important role in the LFC process. Mirbagheri *et al.* (2004) used empirical pressure to correct the free surface pressure as in the original VOF method (Hirt and Nichols, 1981). By forcing the tangential stress at the metal front to vanish and normal stress to balance the externally exerted normal stress, Kuo *et al.* (2003) applied back pressure force in the momentum equation and used several trials to determine a proper back-pressure for the model to get agreement data with experimental results. In the present study to improve the basic model in FLOW-3D®, a correction factor caused by the gas pressure at the metal front is introduced as follows,

$$f_p = c_k + (1 - c_k) \cdot \left(\frac{p_h}{p_h + p_g \cdot t_c} \right) \tag{3.17}$$

where c_k is the pressure coefficient;

p_h is the average pressure head for the pouring of metal in the sprue;

p_g is the gas pressure in the kinetic zone;

t_c is the ratio of coating thickness to the characteristic length scale of the surface irregularities at the metal/foam interface.

The gas pressure in the kinetic zone is a value measured from experiments. It is dependent on metal front velocity and foam density. Under a typical metal front velocity of 1.5 cm/s for aluminum LFC process, p_g is measured to be 10 to 30 kPa (Liu *et al.*, 2004). Experimental results are presented in detail in Chapter 4.

3.6.2 Effect of Metal Temperature

Wang *et al.* (1993) used a foam decomposition model based on a linear temperature dependence on the metal front velocity. But from Yao's (1994) experiment, the highest metal front velocity is observed at a metal temperature of 490°C. Metal temperatures lower or higher than 490°C lead to longer mold filling times. The nonlinear dependency of metal front velocity on the metal temperature is probably related to foam degradation characteristics. From the analysis of foam degradation characteristics listed in Appendix A, the peak volatilization temperature for EPS foam is about 400 to 420°C. If the metal temperature is less than the EPS peak volatilization temperature, the degradation products are essentially viscous residues which may result in higher resistance to the flow molten metal and lower metal front velocity. At the EPS peak volatilization temperature, the gaseous degradation products consist essentially of the monomer. If the metal temperature is higher than the EPS foam peak volatilization temperature, the monomer molecules undergo extensive fragmentation and the volume of the gases produced increases resulting in higher pressure in the kinetic zone. Depending on how effectively the gaseous product can be eliminated through the coating layer of the foam pattern, the metal front velocity is reduced at different levels. To improve the basic model in FLOW-3D®, a correction factor was introduced to take into account of different metal pouring temperatures.

$$f_T = c_T\left(\frac{T_p}{T_p + abs\left(T_m - T_p\right)}\right) \tag{3.18}$$

where T_p is the peak volatilization temperature set as 490°C in this model;

T_m is the metal pouring temperature;

c_T is the coefficient of temperature.

3.6.3 Effect of Bead Degree of Fusion

Yao (1994) observed that even when the density of the foam patterns is held constant, mold filling velocities may vary because of the different degrees of bead fusion in the patterns. By fracturing foam patterns Liu (1995) suggested that the number of fractured beads can act as an indicator of the degree of bead fusion. Rossacci and Shivkumar (2003) quantified the degree of fusion by quantitative image analysis techniques which was also correlated with the tensile test properties. In the study of Sands and Shivkumar (2005), the bead fusion was reported to have a very important effect on the mold filling and the defect formation in the LFC of aluminum alloys. In the present study to improve the basic model in FLOW-3D®, a correction factor was also introduced to incorporate the effect of bead fusion in the model.

$$f_D = c_D\left(\frac{DOF_a}{DOF_D}\right) \tag{3.19}$$

where DOF_a is the average degree of fusion for foam patterns used in casting, which is usually 50%;

DOF_D is the foam degree of fusion for the problem;

c_D is the coefficient of bead fusion.

3.7 Model of Defect Tracking

The LFC model in FLOW-3D$^{®}$ developed a scheme to predict defects which may be formed in the casting process (Barkhudarov and Hirt, 1998). Many defects observed in traditional casting processes originate from surface contamination that is entrained into the body of the metal. Surface contamination may come from loose sand, oxides and coatings. In LFC the liquid and gas product of foam patterns is extra source of contamination. For the surface contamination to be entrained into the interior of a casting, there may be meeting of two fronts or by surface turbulence which produces local overturning at the metal surface (Campbell, 1993).

The probability of defects is represented by a scalar variable that is initially zero in the flow region. The scalar quantity is incremented by an amount proportional to the mass of degraded foam in the control volume and it is allowed to accumulate at the metal front and to be trapped in metal if the two fronts meet. As the metal continues to fill the mold, the scalar variable can advect and diffuse into the casting. In the output of the simulation, the distribution of the scalar shows the probability of defect formation locations.

A wicking model is also implemented in FLOW-3D$^{®}$ after the original lost foam model was found to have some shortcomings in defect transport near the wall region

(Hirt, 1999). From experimental study, Shivkumar (1987) and Sun (1992) showed that the rate of foam liquefaction in aluminum casting was much greater than the rate of vaporization. The wetting and wicking properties of the refractory coating was very important in effective eliminating the foam product and reduce casting defects. The penetration of liquid foam residues in the coating is primarily determined by the value of its contact angle, which is a function of the chemistry of the coating material.

The original defect scalar in FLOW-3D® is proportional to the amount of foam that is degraded at each location along the metal front and then transported it with the moving metal. A second scalar quantity is introduced to account for the wicking of defect material into the coating and sand. This new scalar can only gain defect material from the original defect scalar. Once the defect material is stuck to the walls, it does not move with the flowing metal and the quantity is taken out of the original scalar defect quantity. The wicking scalar is proportional to the product of the original defect scalar and the coating wall area located in that computational cell. A constant of proportionality coefficient which is a rate per unit time and unit area is introduced and it is determined from experiment.

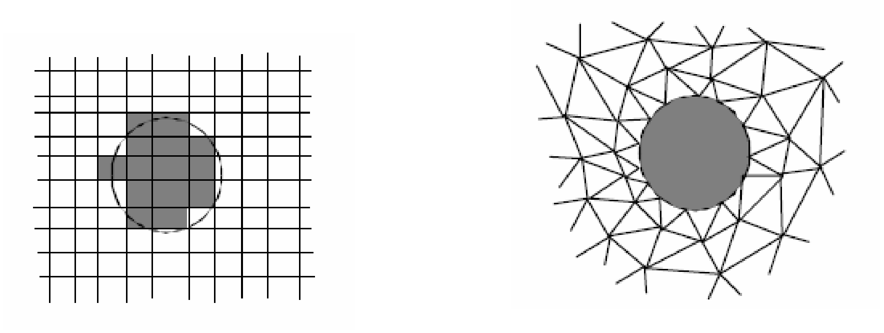

(a) (b)

Figure 3.1 Typical mesh resolutions of a circular object by (a) finite difference method and (b) finite element method (Flow Science)

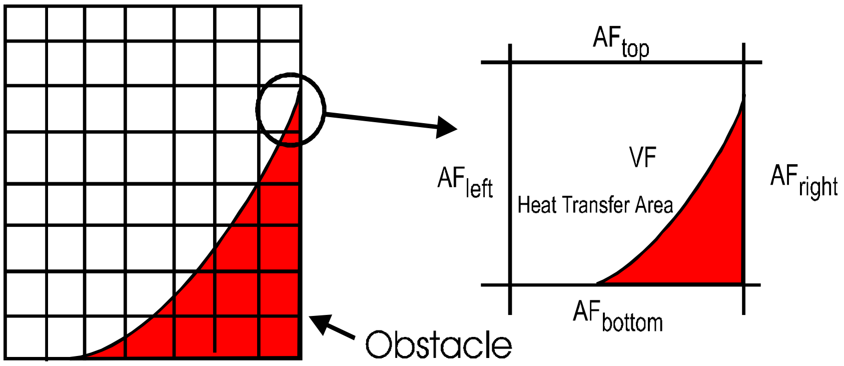
AF_{top}
VF
AF_{left}
Heat Transfer Area
AF_{right}
AF_{bottom}
Obstacle

Figure 3.2 The FAVOR method to describe geometry in finite difference grids with definitions of the open area and volume fractions (Flow Science)

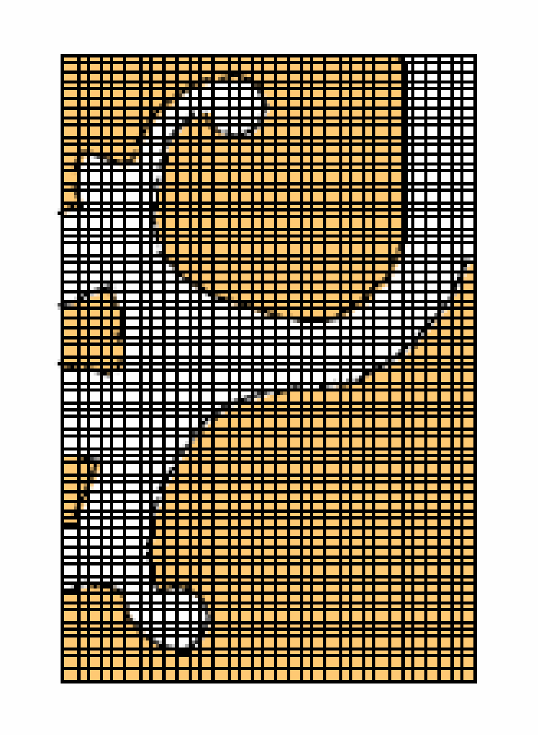

Figure 3.3 Coarser grid than in standard finite difference methods can be used to represent complex geometries by the FAVOR method (Flow Science)

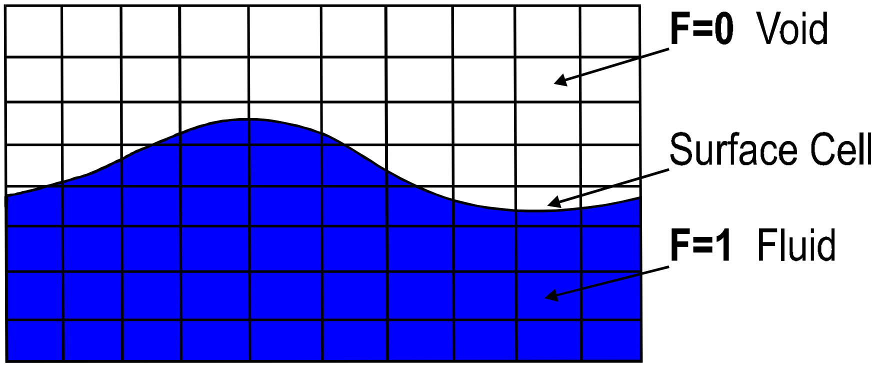
F=0 Void
Surface Cell
F=1 Fluid

Figure 3.4 Volume of Fluid (VOF) function definition (Flow Science)

CHAPTER 4 EXPERIMENTAL RESULTS AND DISCUSSION

In this chapter, first the results from the visualization experiment of the foam decomposition are summarized. Then for the fully coated foam patterns, experimental results of kinetic zone size and temperature, heat transfer coefficients and gas pressures are discussed.

4.1 Morphology of Polymer Foam Patterns

All the polymer foam patterns have smooth surfaces with fused beads packed next to each other as shown in Figure 4.1(a). The diameters of the beads are in the range of 0.3 to 1.2 mm. The surface finish of LFC products is significantly improved over traditional sand casting due to the smooth bead structure and protective coating materials surrounding the foam pattern. The lines on the bottom of right side of Figure 4.1(a) are formed by the slits for venting on the aluminum mold during the foam production. There are totally 105 vents evenly distributed on the 760 cm^2 surface of the foam pattern with an average of 7.2 vents/cm^2.

On the fractured surfaces of EPS and copolymer (70%EPS and 30%PMMA) foam patterns as shown in Figure 4.1(b) and (c), the bead structure can be visually identified as either trans-bead or inter-bead fracture. As suggested by Rossacci and Shivkumar (2003), the high trans-bead fracture indicates a higher degree of bead fusion, and high inter-bead fracture indicates a lower degree of bead fusion. From Figure 4.1(b) and (c), it can be seen that the copolymer has a higher degree of bead fusion than the EPS foam. If a hot-wire cutter is used to produce a foam pattern, the bead surface is changed into a fully fused surface and the bead structure can not be identified as shown in Figure 4.1(d). Since the mold filling process is affected by degree of the bead fusion, the hot-wire cutting needs to be practiced with caution.

The morphology of a polymer foam pattern after a half-run experiment is shown in Figure 4.2. The foam residual with coating is shown in Figure 4.2(a), and it is obvious that there is dark-colored foam residual on the interior of coating material. This residual can be source of defects in the final casting product. A close look at the foam interface is shown in Figure 4.2(b). Usually foam turns into gaseous products and finger-like liquids. While the liquids are observed in the half-run test, the gaseous products escaped through the coating and into the sand. It is interesting to see that the interface of a cylindrical foam pattern has formed into a concave shape.

4.2 Visualization Experiments

Observation of the degradation of the EPS foam pattern with density of 24 kg/m³, using a steel block velocity of 0.036 cm/s (Figure 4.3(a): (i) to (viii)) showed that there was a gaseous gap between the steel block and the foam pattern. The shape of the gaseous gap was not regular but finger like, which confirmed the observation of Yao (1994). The size of the gap decreased during the process from 3-4 cm at the beginning to 0.5-1 cm towards the end of the process, as shown in Figure 4.3(b). For higher metal velocity, the size of the gap was observed to be between 1-4 cm during the whole process. Similar observations were recorded for other velocities, foam densities, and coating thicknesses.

Gap size observed from video images agreed well with that measured from thermocouples located inside the EPS foam pattern as shown in Figure 4.4(b). Video observation of the degradation of the foam pattern with EPS density of 27 kg/m³, using a metal front velocity of 1.5 cm/s was shown in Figure 4.4(a): (i) to (iii).

In a study of aluminum casting, Walling (1995) used spray photo adhesive to glue the foam pattern to a sheet of pyrex glass. The reason Walling reported no vapor gap was probably because the spray photo adhesive interfered with the heat transfer from the metal to the foam pattern and decreased the temperature of the metal front. The absence of a vapor gap in the Tseng and Askeland (1991) study was probably due to the lack of coating material on the foam pattern. Under those conditions, the pyrolysis products could easily leave the system under low pressures without the need to build-up a high pressure vapor phase.

4.3 Heat Flux and Heat Transfer Coefficient Measurements

The response of the thermocouples located inside the simulated metal front for a foam density of 24 kg/m³ with velocity of 0.44 cm/s and coating thickness of 1.2 mm is shown in Figure 4.5. The thermocouple response for a foam density of 27 kg/m³ with the same velocity and coating thickness is very similar to that for the 24 kg/m³ samples. It suggests that the heat fluxes to the two different density foam patterns are also similar.

In Figure 4.6 (a) and (b) heat fluxes from metal front to foam for two different density EPS foam patterns are shown at the metal velocity of 0.44 cm/s and 1.5 cm/s, respectively. As expected from the temperature profile, the heat fluxes for the two foam densities are almost identical. For both densities, the values of heat flux, initially 78 kW/m², gradually increases to 110 kW/m² to the end of the process at a velocity of 0.44 cm/s. The heat flux at a higher velocity of 1.5 cm/s increases to 140 kW/m² to the end of the process. It is interesting to notice that the heat flux from the metal front to the foam is not constant, but keeps increasing during the process. This can be understood by considering the energy balance model shown in Equation (4.1):

$$q_s = \rho V c_p (T_z - T_z) + \rho V Q_{liq} + \rho V Q_{vap} + \rho V Q_{depoly} \tag{4.1}$$

where q_s is the surface heat flux;

ρ is the EPS foam density;

c_p is the EPS foam specific heat;

V is the metal front velocity;

Q_{liq} is the latent heat of fusion of foam;

Q_{vap} is the heat of vaporization;

Q_{depoly} is the heat of depolymerization.

The first term on the right hand side of Equation (4.1) is the sensible heat of the foam, which is constant as the metal advances and the foam recedes. The other three terms on the right hand side of the equation are not constant and they cause the heat flux to increase during the process. As the metal front moves to replace the foam pattern, the foam first collapses when the temperature of the foam reaches about 120°C. Then the foam starts to vaporize and decompose as the foam temperature increases. Since the process is an unsteady process, part of the foam gets decomposed and the rest of the foam is accumulated at the kinetic zone. The increase in heat flux at the metal front is because the melted foam keeps accumulating at the metal front thus more and more heat is needed to remove it. The problem is further complicated by the fact that some foam liquid or gas products dissipate through the coating and into the sand before getting depolymerized.

From the measured surface heat flux and metal front temperature, the heat transfer coefficient can be calculated by Equation (2.1) if the kinetic zone temperature, T_z, is known. In the experiment, the kinetic zone temperature is measured by the four thermocouples precisely positioned inside the foam pattern. A typical result is shown in Figure 4.7 for the 27 kg/m^3 foam pattern with a coating thickness of 0.07 cm and a metal front velocity of 0.95 cm/s. Figure 4.8 (a) shows the kinetic zone temperature and Figure 4.8(b) shows the gaseous gap in three test runs. The kinetic zone temperature is about 200°C and the gaseous gap size is between 1 to 4 cm for all three runs. For different foam densities, coating thickness and metal front velocities, the kinetic zone temperatures measured were in the range of 150 to 290°C, with an average of 200°C as shown in Figure 4.9. The kinetic zone temperature is not a strong function of foam density, coating thickness or metal front velocity. This confirms the assumption made by Warner *et al.* (1998) that the kinetic zone temperature is about 250°C in aluminum LFC castings and by Walling (1995) that this temperature is about 200°C. The kinetic zone gap size is between 1 to 4 cm for different metal velocities, foam densities and coating thickness, which is in good agreement with the visualization experiment. However, the decrease observed in the gap as the experiment progressed was not supported by the measurements from embedded thermocouples.

By using an average value of the kinetic zone temperature, T_z, 200°C in the gaseous gap, the heat transfer coefficient can be calculated from Equation (2.2) and it is plotted in Figure 4.10(a) for a metal front speed of 0.44 cm/s and in Figure 4.10(b) for a metal front velocity of 1.5 cm/s with the same coating thickness of 0.12 mm. For both densities, 24 kg/m³ and 27 kg/m³, the values of heat transfer coefficient, initially 150 W/m²·K gradually increase to 220 ~ 300 W/m²·K to the end of the process. The increasing trend in heat flux and heat transfer coefficient has been observed for experiments under different metal front velocities. Higher values are obtained towards the end of the process for higher metal front velocities.

According to Mehta *et al.* (1995), the heat required for polystyrene foam degradation is estimated to be on the order of 912 J/g measured using differential scanning calorimetry (DSC) and thermogravimetric analysis (TGA). Based on this value of polystyrene degradation heat, the average heat flux required for a 25.4 cm long foam pattern of density 24 kg/m³ and 27 kg/m³ with a speed of 0.44 cm/s are 93 kW/m² and 104 kW/m², respectively. As can be seen in Figure 4.6, the minimum and maximum heat fluxes measured in the current experiment are 78 kW/m² at the beginning and 110 kW/m² at the end of the process, showing good agreement. The discrepancy is due to the different final degradation products between the current experiment and the DSC and TGA experiments. Another reason is that some heat is lost to the environment in the experiment, whereas the DSC and TGA measurements were carried out in a closed chamber.

As the metal front advances, heat is lost from the steel surface to the pattern as well as to the sand. The process is further complicated because the pattern degradation products have to be eliminated from the metal front. Limitations on the mass transfer of these products through the coating materials and into the sand may introduce back pressure and affect the behavior of the foam pattern. The liquid polymer is displaced into the coating and sand surrounding the casting, where it continues to degrade with additional heat absorbed from the metal.

The fact that foam density has only a marginal effect on the heat flux from the metal surface to the foam reveals that the cooling effect on the metal front is not controlled by the foam properties but by heat and mass transfer in the gaseous gap and through the sand mold. Nevertheless, the fluidity of the metal is known to be impaired by higher foam density (Pan and Liao, 2000). This is quite reasonable because foams with higher density require more thermal energy to liquefy/gasify from the molten metal during the whole process of foam degradation. From an energy balance point of view, since the heat flows are similar at the metal front for different density patterns, then the heat needed to further eliminate the liquid/gas products remaining in the coating or the sand surrounding the metal is larger for the higher density foam patterns than the lower density ones during the solidification process.

Barkhudarov and Hirt (1998) used a constant heat transfer coefficient in the modeling of LFC. Chang and Chai (1989) assumed a value of 1300 $W/m^2 \cdot K$ and 200 $W/m^2 \cdot K$ for the heat transfer coefficient between the flowing metal front and the pattern, and between the metal and the sand mold, respectively. Not only were the heat transfer coefficients assumed to be constant in these models, but also the kinetic zone temperature was assumed to be the same as that of sand mold which was at room temperature. From the present study, it is clear that the temperature difference in Equation (2.2) should be the temperature difference between the instantaneous metal surface and the kinetic zone temperature. Khan *et al.* (2000) investigated the interfacial heat transfer coefficient between the casting and the sand during lost foam casting and found that the interfacial heat transfer coefficient was in the range of 40-160 W/m²·K depending upon the specific process parameters. There has been no experiment carried out to measure the heat transfer coefficient between the casting and the foam and the current research provides a better understanding of the mechanisms of the lost foam casting process.

4.4 Pressure Measurements

The peak pressures for a metal front velocity of 0.44 cm/s, 0.95 cm/s and 1.5 cm/s with different EPS foam densities and coating thicknesses are shown in Figure 4.11. For both EPS foam density of 24 kg/m³ shown in Figure 4.11(a) and 27 kg/m³ shown Figure 4.11(b), the gap peak pressure increases as the metal front velocity increases. Higher foam density gives rise to higher peak pressure with a metal front velocity less than 0.95 cm/s. With a metal front velocity of 1.5 cm/s, the peak pressure increase an order of magnitude from the value obtained at the lower velocity, while the density effect is not as prominent. For a metal front velocity of 1.5 cm/s with EPS foam density of 24 kg/m³ and coating thickness of 0.12 cm, the peak pressures are in the range of 16 and 35 kPa with an average of 25 kPa as shown in the tabulation in Figure 4.11. This pressure is much higher than that with lower velocities of 0.95 cm/s, 0.44 cm/s and 0.36 cm/s, but lower than the average peak pressure at a density of 27 kg/m³ under the same coating and velocity conditions.

It is evident that the faster the metal moves, the higher the gap pressure that results. The maximum gas pressure measured under low metal front velocity is close to the pressure reported by Shivkumar and Gallois (1987) which was 0.42 kPa with EPS foam density of 20 kg/m³ under equilibrium conditions. These data also partly confirm the pressure value reported by Liu *et al.* (2002) which was 6.57 kPa for 25 kg/m³ with 0.05 cm coating at velocity of 3 cm/s. But Yang *et al.* (1998) reported pressure values as low as 0.2 to 0.5 kPa for a 20 kg/m³ foam pattern with 0.02 cm coating at velocity of 1.6 to 4.6 cm/s. Both the Liu *et al.* and the Yang *et al.* experiments used pressure tubes positioned inside the foam pattern. This method can record pressure information only in a small portion of the whole process and it was not capable of capturing the entire gaseous pressure information during the whole process. The useful signal period used by Liu *et al.* was less than 1 second between the collapse of the foam pattern and the subsequent immersion of the pressure tube in the metal. This short period may not be representative of the complete process. The problem was even more evident in the Yang *et al.* experiment because the pressure tube used was probably too big for a pressure transducer to capture the small pressure signals. The interior and exterior diameters of the pressure tubes used in Yang et al experiment were 0.4 cm and 0.6 cm, respectively.

As shown in Figure 2.7(a), in the top-down experiment, two additional pressure taps (P1 and P2) were positioned inside the foam pattern to verify the signals measured by pressure tap (P) which was connected to a pressure tube passing through the steel block. A typical result is shown in Figure 4.12 for a metal front velocity of 1.5 cm/s with a foam density 27 kg/m³ and a coating thickness of 0.07 cm. The peak pressures measured by tap P1 and P2 are comparable to that measured by P which gave the whole picture of the pressure development during the process, whereas the signals from embedded pressure taps P1 and P2 are useful only for the time that the foam melts past the tap location until the steel block makes contact with the tap which is shown by arrows in Figure 4.12. The measured pressure in the gap between the metal front and the foam pattern is further confirmed by data in literature as shown in Figure 4.13. For foam density of 24 kg/m³, the gas pressure of the present study agrees reasonably well with that in Mirbaghri *et al*. (2004).

According to Warner *et al.* (1998), two distinctly different regimes exist for the decomposition and subsequent transport of gaseous/liquid EPS degradation products. The first is associated with low coating permeability and high metal front velocity. In this regime, called the back pressure controlled regime, a large amount of gaseous products build up in the gap between the metal front and foam pattern. Mold filling is controlled by the rate at which the refractory coating allows the gaseous products to escape into the sand. The second regime is associated with high coating permeability and low metal front velocity. In this regime, called foam-decomposition controlled regime, high permeability coatings allow the products of decomposition to easily escape from the kinetic zone. Under a constant metal front velocity, the foam decomposition products quickly penetrate through the coating and sand leaving a gaseous gap between the foam and metal front with convection currents in it.

The pressure trace indicates that the value is low except for several peaks in the process for the low metal front velocities. The phenomenon suggests that the gaseous products are effectively released from the kinetic zone which confirms that the flow is in the foam-decomposition controlled regime, which helps produce high quality castings. At higher simulated metal front velocities, the gap peak pressure increases one order of magnitude with the peaks more continuous as shown in Figure 4.12. This indicates that the flow for higher metal front velocity is in the back-pressure-controlled regime. The gaseous product at the front of the metal front can be trapped in the casting and cause defects in the final product.

4.5 Effects of Process Variables on Kinetic Zone Temperature

Effect of pattern density, metal front velocity and coating thickness on the kinetic zone temperature has been investigated. Shown in Table 4.1 under the same coating thickness, the kinetic zone temperature varies from 190°C to 255°C for EPS density 24 kg/m³, EPS 27 kg/m³ and copolymer 25 kg/m³ under metal front velocity of 0.44 cm/sec, 0.95 cm/sec and 1.5 cm/sec. There is no significant dependency on the foam materials and metal front velocity observed in the data. Similar results were obtained for coating thickness of 0.2 mm and 1.2 mm. The current research confirmed Walling's (1995) suggestion that the gaseous gap temperature is about 200°C. Due to the chaotic behavior of the foam elimination process, the temperature of the kinetic zone varies with experimental conditions in the range ±20% of the mean value.

Table 4.1 Kinetic zone temperature for different foam and metal front velocities under the same coating thickness of 0.7 mm

Variables	0.44 cm/sec	0.95 cm/sec	1.5 cm/sec
24 kg/m³ EPS	249.2	190.0	255.0
27 kg/m³ EPS	232.2	195.5	204.1
25 kg/m³ Copolymer	192.9	244.0	247.6

4.6 Effect of Metal Initial Surface Temperature on the Kinetic Zone

The effect of metal initial surface temperature on the kinetic zone is illustrated in Table 4.2 at metal front velocity of 1.5 cm/sec with coating thickness of 0.2 mm for EPS 24 kg/m³. Gas peak pressure, kinetic zone temperature and gap size seemed to reach maximum value at 750°C under these conditions. But the data shown in Table 4.3 for EPS 27 kg/m³ did not have this trend. The gas peak pressure ranged from 9 to 22 kPa, gap size was between 1 to 2.2 cm and kinetic zone temperature was about 200°C. In the study of Shivkumar *et al.* (1990), it was shown that the gas yield of thermal degradation of the polymer pattern keeps almost constant in the range of 600°C to 900°C. In the current study of aluminum alloy temperature range of 730°C to 850°C, the effect of temperature difference was shown to be insignificant because the process is controlled by the foam decomposition process instead of the characteristics of molten metal.

Table 4.2 Effect of metal initial surface temperature at metal front velocity of 1.5 cm/sec with coating thickness of 0.2 mm for EPS 24 kg/m³

Metal Initial Surface Temperature (°C)	Gas Peak Pressure (kPa)	Kinetic Zone Temperature (°C)	Gaseous Gap Size (cm)
730	11.9	163	1.2
750	15.4	225	2.2
780	9.0	220	1.8

Table 4.3 Effect of metal initial surface temperature at metal front velocity of 1.5 cm/sec with coating thickness of 0.2 mm for EPS 27 kg/m³

Metal Initial Surface Temperature (°C)	Gas Peak Pressure (kPa)	Kinetic Zone Temperature (°C)	Gaseous Gap Size (cm)
730	21.9	175.0	1.5
750	10.9	168.5	1.7
780	14.4	217.5	1.9

4.7 Effects of Process Variables on Gas Peak Pressure

An Analysis of Variance (ANOVA) F-Test was performed on the effect of foam density, metal front velocity and coating thickness on the gas peak pressure. Foam density was chosen to have two levels 24 kg/m³ and 27 kg/m³. Metal front velocity was chosen to have three levels 0.44 cm/s, 0.95 cm/s and 1.5 cm/s. Coating thickness was chosen to have two levels 0.23 mm and 0.7 mm. ANOVA results on the response of gas peak pressure were shown in Table 4.2. The high F-value and very small P-value showed that the metal front velocity has a statistically important effect of the gas peak pressure. There is only a 0.01% chance that the large F-value could occur due to other noise. Foam density also had similar effect on the gas peak pressure, but the F-value is smaller than that of metal front velocity indicating a weaker effect on the gaseous pressure. The F-value for coating thickness is the smallest among the three factors studied, and the P-value is 0.105 which indicates the effect of coating thickness on the gas peak pressure is not statistically significant.

Table 4.2 ANOVA F-value results of gas peak pressure for the factors of metal front velocity and foam density

Factor	Residual Sum of Squares	Degrees of Freedom	Mean Square	F-value	P-value
Metal Front Velocity	1227.5	2	613.7	150.6	<0.0001
Foam Density	266.7	1	266.7	65.5	<0.0001
Coating Thickness	149.0	3	49.7	2.85	0.105 Not significant

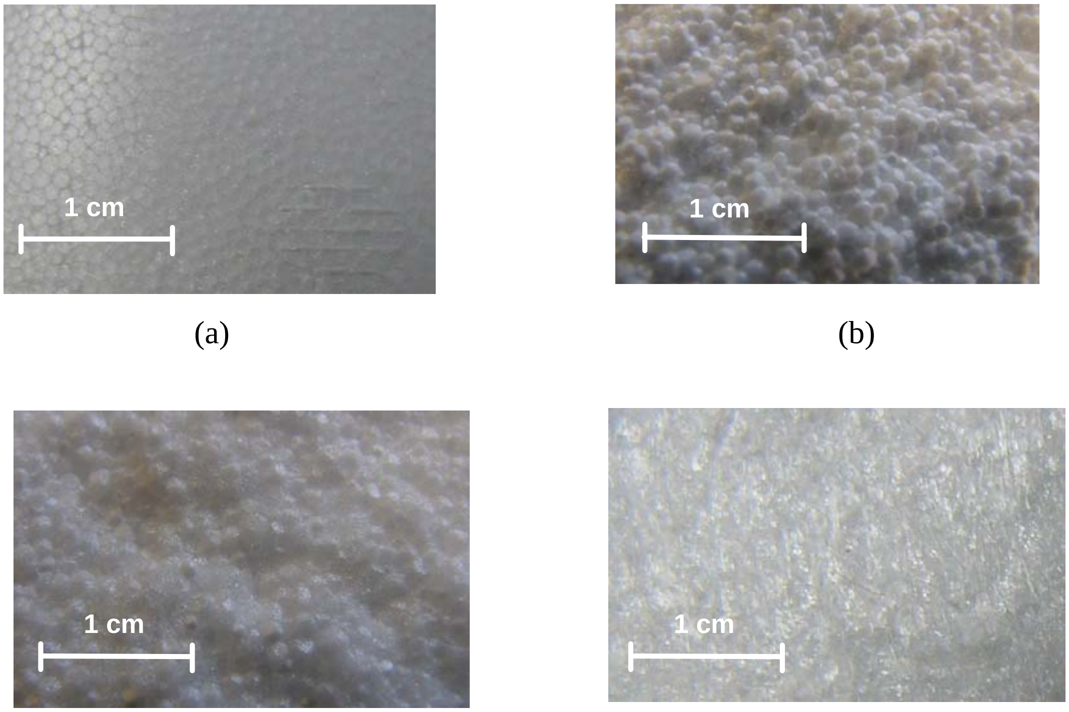

(a) (b)

(c) (d)

Figure 4.1 Morphology of the polymer foams: (a) outside fused surface, (b) fractured surface for EPS foam polymers, (c) fractured surface for copolymer (70%EPS and 30%PMMA), and (d) hotwire-cut surface

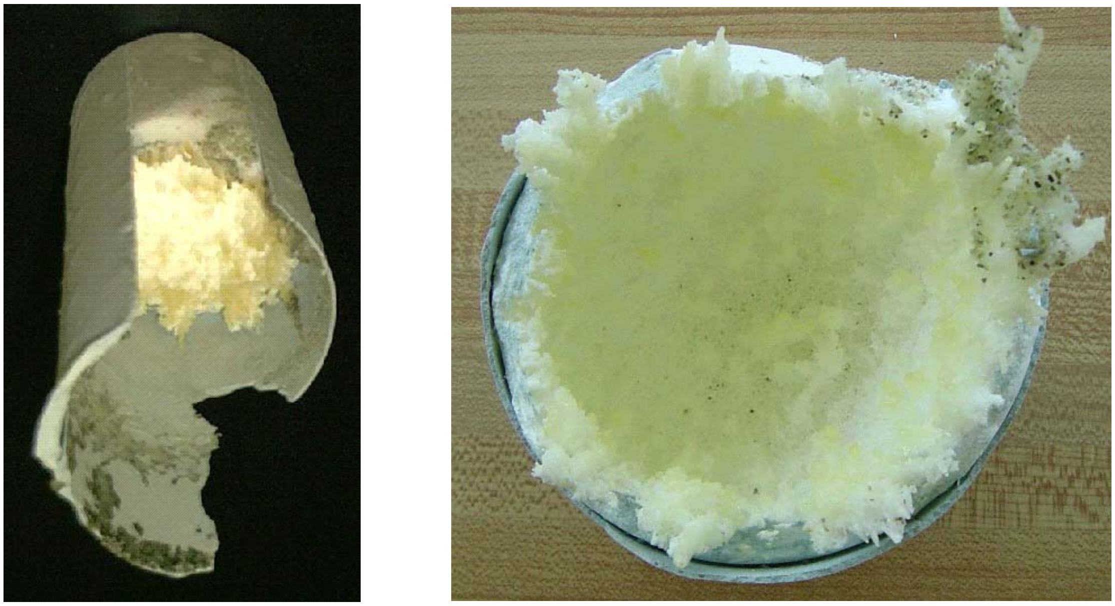

(a) (b)

Figure 4.2 Morphology of the polymer foams: (a) coating and foam residual in a half-run test, and (b) close look of the foam interface

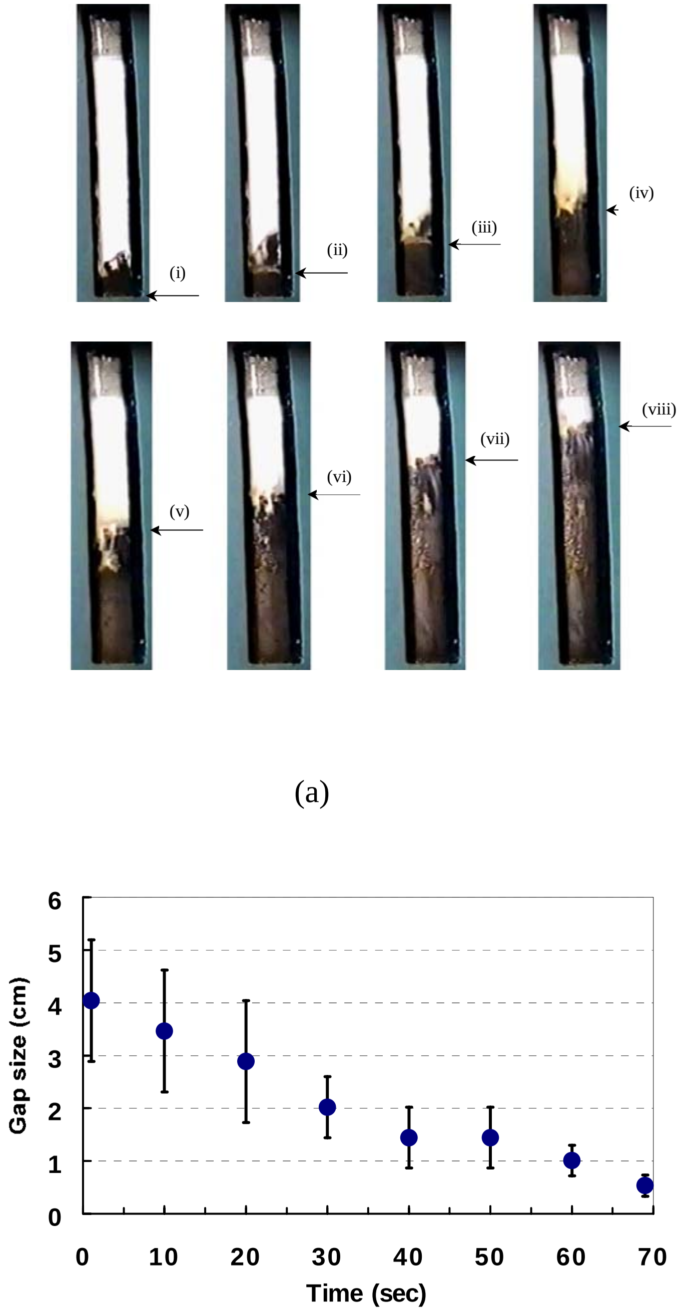

(b)

Figure 4.3 (a) Quartz window observations and gaseous gap size for a foam density of 24 kg/m³ with a metal front velocity of 0.036 cm/s and coating thickness of 0.12 cm at (i) 0 second, (ii) 10 seconds, (iii) 20 seconds, (iv) 30 seconds, (v) 40 seconds, (vi) 50 seconds, (vii) 60 seconds, and (viii) 70 seconds. The arrow indicates the metal front position. (b) Gap size observed from these images

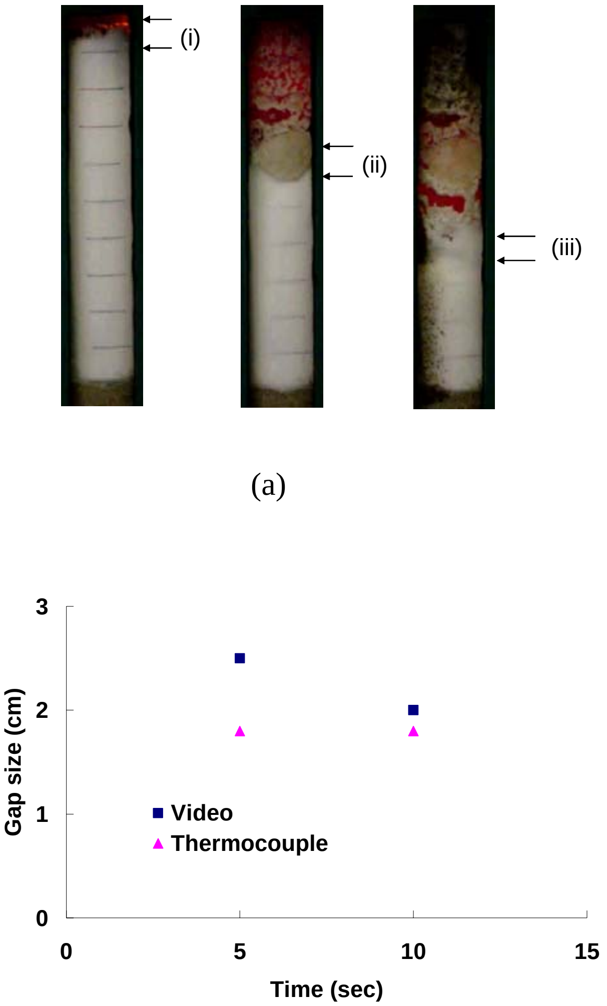

(a)

(b)

Figure 4.4 (a) Quartz window observations and gaseous gap size for a foam density of 27 kg/m^3 with a metal front velocity of 1.5 cm/s at (i) 0 second, (ii) 5 seconds, and (iii) 10 seconds. The arrow indicates the metal front position. (b) Gap size observed from these images and measured from thermocouples

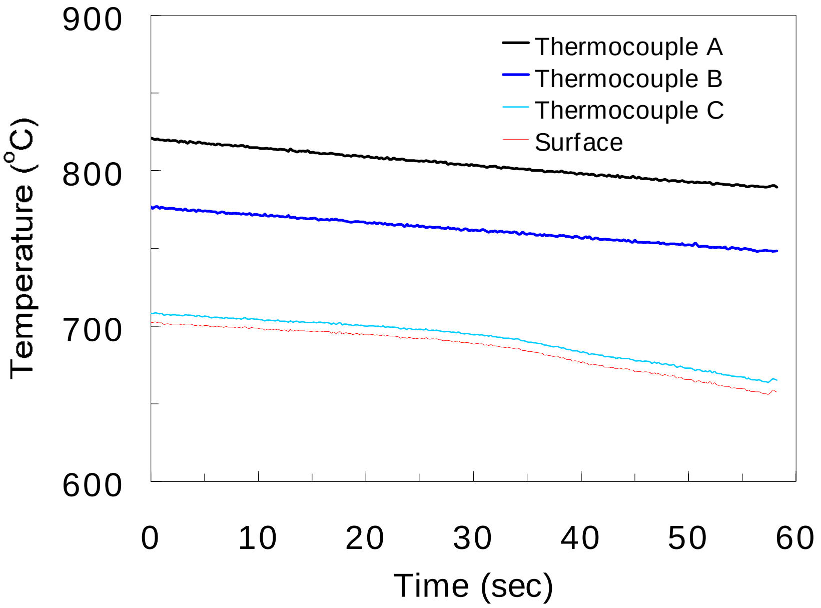

Figure 4.5 Response of thermocouples inside simulated metal front for a foam density of 24 kg/m³ with velocity of 0.44 cm/s and coating thickness of 0.12 cm

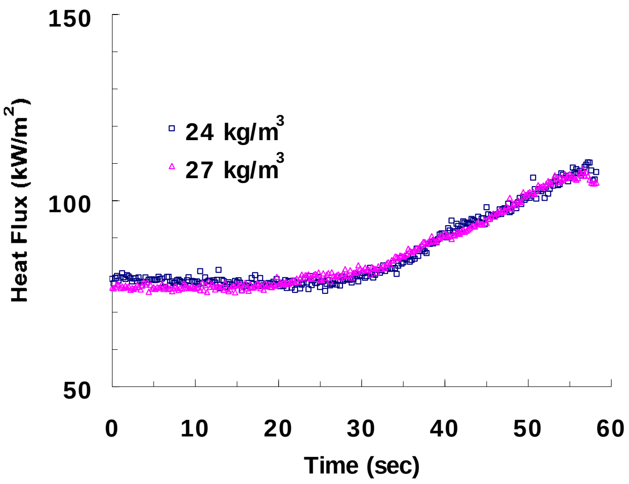

(a)

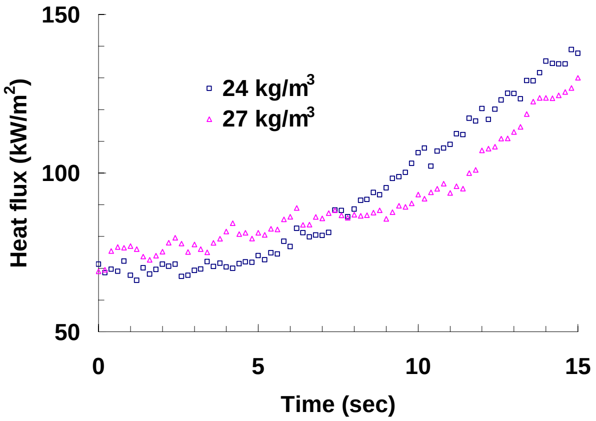

(b)

Figure 4.6 Heat flux at the simulated metal front for a velocity of (a) 0.44 cm/s, and (b) 1.5 cm/s with coating thickness of 0.12 cm

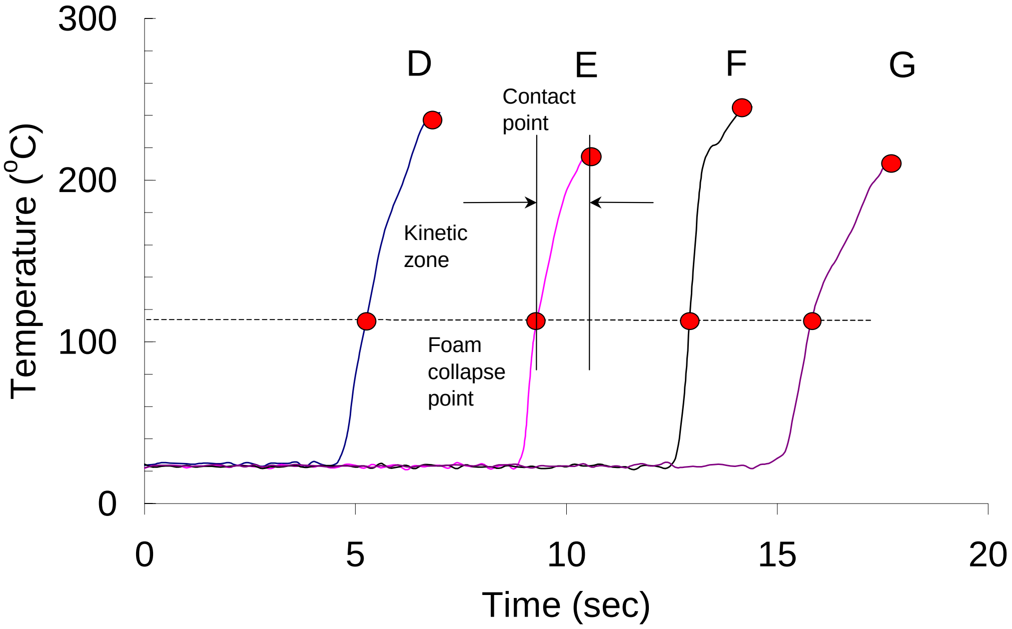

Figure 4.7 Response of thermocouples inside the foam pattern showing the kinetic zone for 27 kg/m³ foam pattern with a coating thickness of 0.07 cm under the metal front velocity of 0.95 cm/s

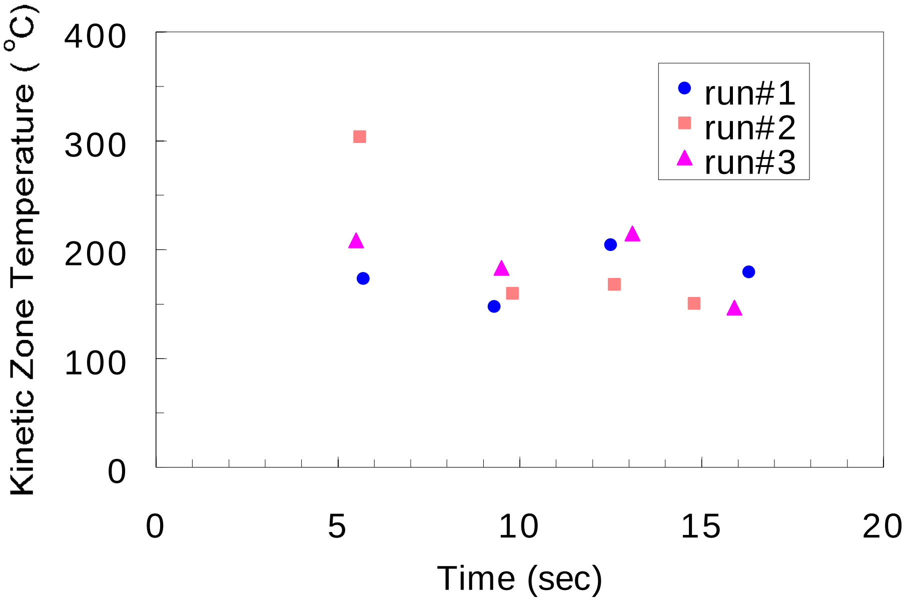

(a)

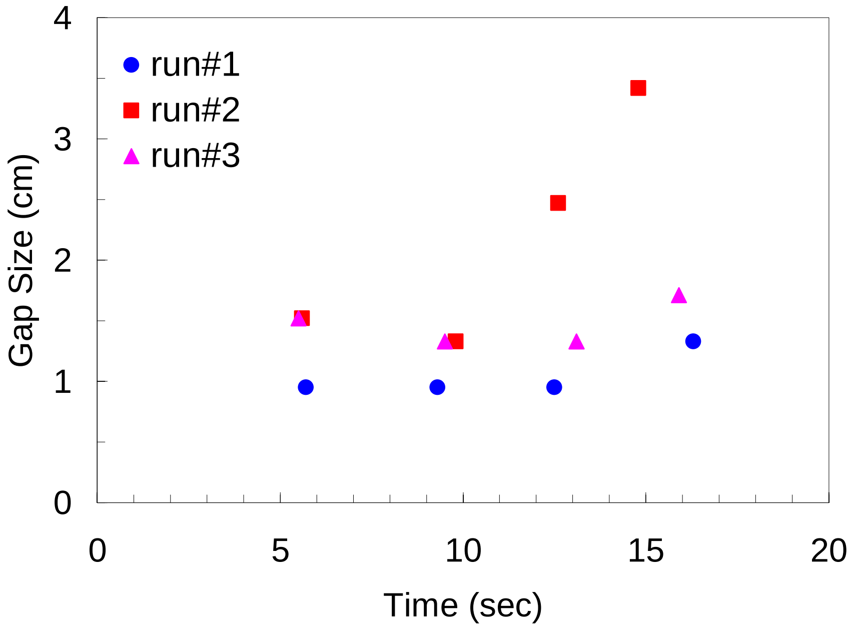

(b)

Figure 4.8 With metal front velocity of 0.95 cm/s, EPS foam density of 27 kg/m^3 and coating thickness of 0.07 cm (a) Kinetic zone temperature, and (b) gaseous gap size

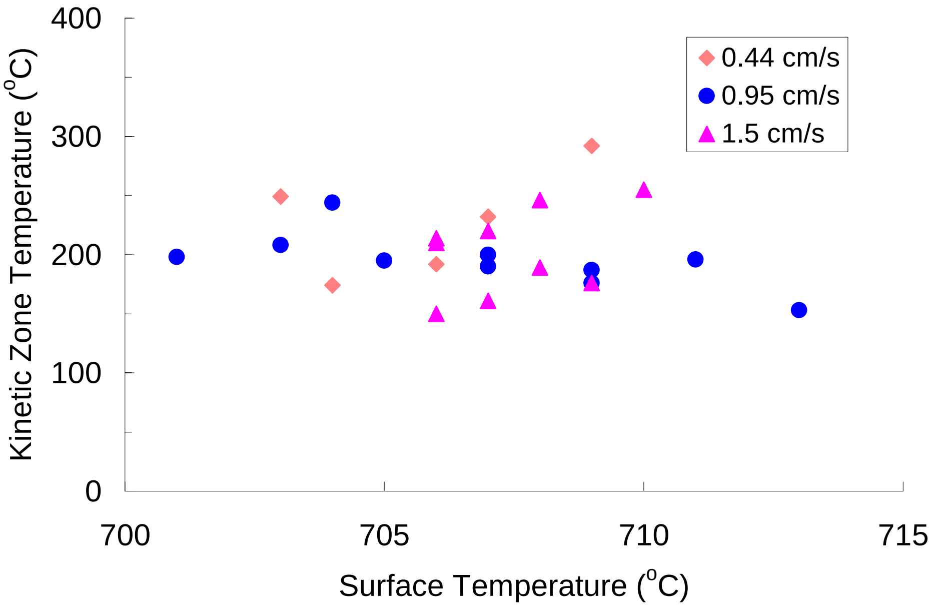

Figure 4.9 Kinetic zone temperature for different metal front velocities with different EPS foam density and coating thickness

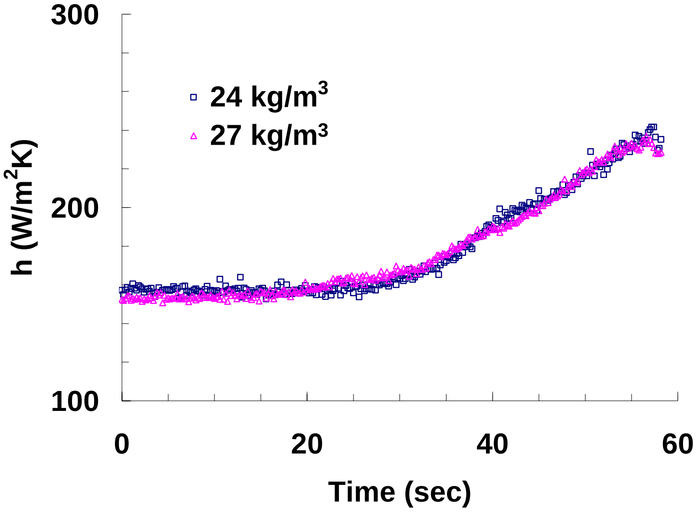

(a)

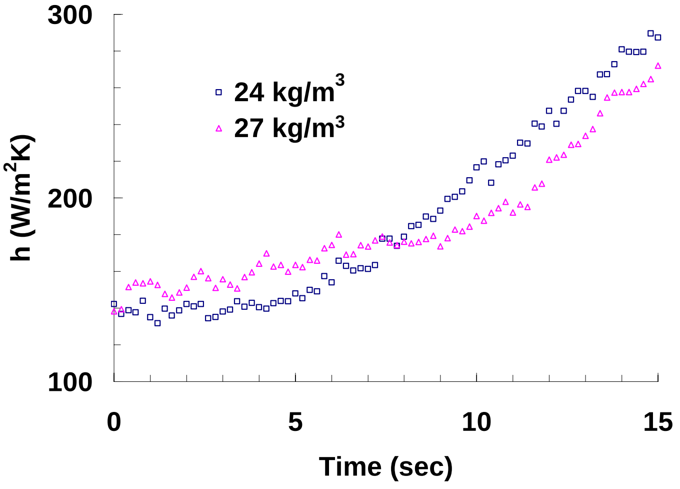

(b)

Figure 4.10 Heat transfer coefficient for a velocity of (a) 0.44 cm/s, and (b) 1.5 cm/s with coating thickness of 0.12 cm

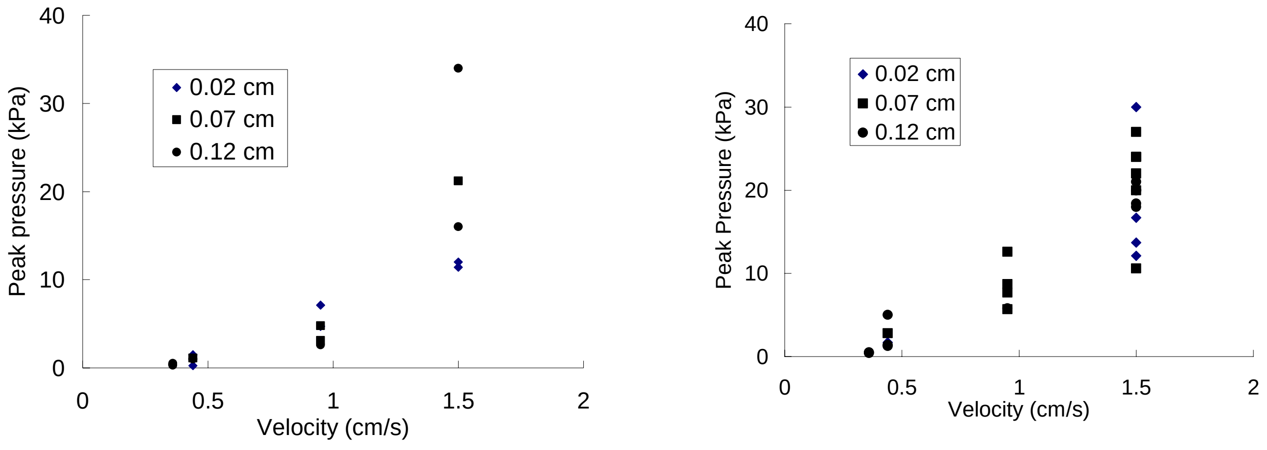

(a) (b)

Metal front velocity (cm/s)	Average peak pressure for EPS foam density of 24 kg/m³ (kPa)	Average peak pressure for EPS foam density of 27 kg/m³ (kPa)
0.36	0.4	0.45
0.44	0.99	2.5
0.95	2.6	5.8
1.5	25	19.4

Figure 4.11 Gap peak pressure as a function of simulated metal front velocity for all the coating thicknesses in both visualization and realistic top-down experiments: (a) foam density of 24 kg/m³ and (b) foam density 27 kg/m³. Gap average peak pressures for a coating thickness of 0.12 cm are listed in the table above

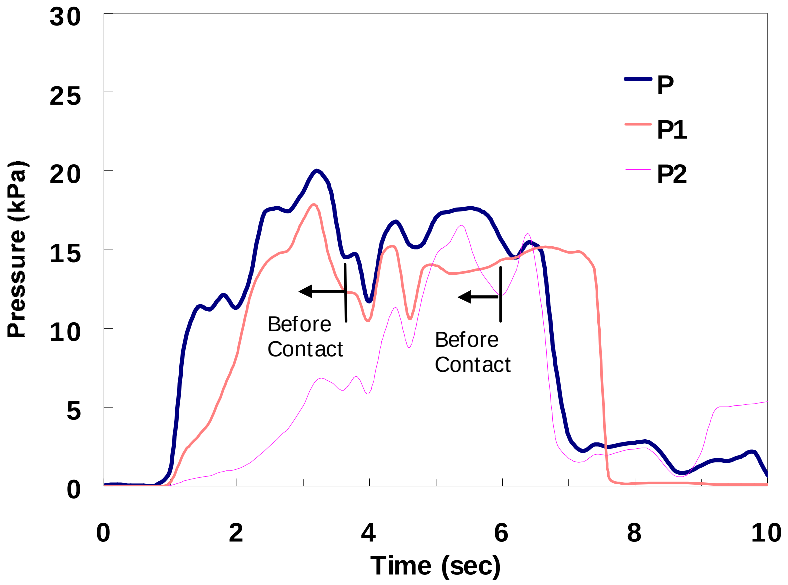

Figure 4.12 Verification of pressure measurement of pressure tap P by another two taps P1 and P2 for a metal front velocity of 1.5 cm/s with a foam density of 27 kg/m³ and coating thickness 0.07 cm. The two arrows show the useful part of pressure signal before the metal front pushes the pressure taps

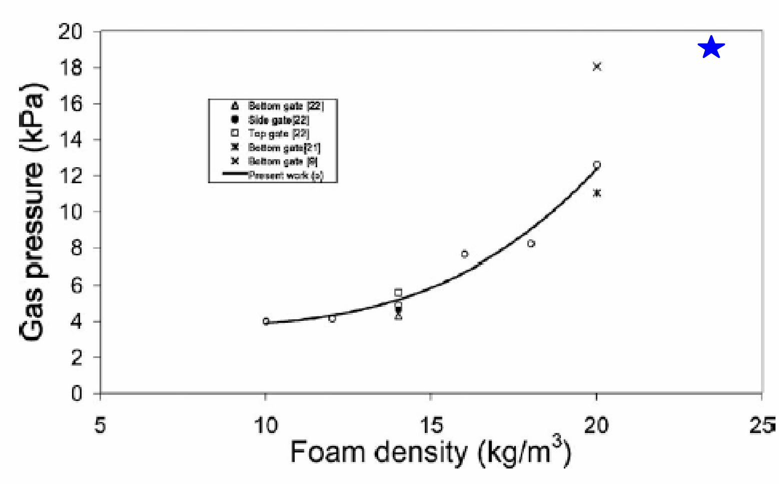

Figure 4.13 Gas pressure between the metal front and foam pattern as a function of foam density (Mirbagheri *et al*., 2004). The blue star shows the possible gas pressure for the foam density in the present work

CHAPTER 5 MODELING RESULTS AND DISCUSSION

The results from numerical modeling of the foam decomposition process were presented. Both code verification and validation were performed. Effects of several process parameters on the defect formation in castings were studied for different geometries.

Grid independence study was performed to estimate discretization errors and verify the codes and solutions. Validation of the numerical model was carried out by comparing numerical simulation against experimental studies. It has been shown that the improved model with varying heat transfer coefficient based on both gas pressure and coating thickness provide a better prediction of metal surface temperature than the basic constant heat transfer coefficient model. Several geometries are investigated with different process parameters such as initial metal temperature, metal front velocity, foam pattern property, degree of bead fusion, and coating thickness. Dependence of defect formation on these variables is also discussed.

5.1 Code Verification and Validation

5.1.1 Simple Cylinder

The cylindrical foam pattern used in experimental study is chosen to verify the modified model of varying heat transfer coefficient at the metal front. From the experiment, it was found that the heat transfer coefficient increases as the metal front advances. The foam pattern is 8.8 cm in diameter and 25.4 cm long. The computational domain is shown in Figure 5.1(a), where h = 25.4 cm and r_0 = 4.4 cm. At r = 0, a symmetric boundary condition was applied. A pressure boundary condition was used at inlet, and no-slip boundary conditions were applied at the right and bottom walls.

In order to determine the proper grid size for this study, a grid independence test was conducted for the cylindrical foam geometry. Four difference grid densities were used for the grid independence study. These grid densities were $5^r \times 30^z$, $10^r \times 60^z$, $15^r \times 90^z$ and $20^r \times 120^z$. The integrated value of mass flow rate from the top gate was used as a monitoring measure of the accuracy of the solution. Figure 5.2 shows the dependence of mass flow rate on the grid size in the longitudinal direction. A similar trend is obtained on the grid size in the radial direction. Comparison of the predicted value of mass flow rate among four different cases suggests that the two grid distributions of $15^r \times 90^z$ and $20^r \times 120^z$ give nearly identical results. The relative change in mass flow rate is less than 0.5 % when grid density increases from $15^r \times 90^z$ to $20^r \times 120^z$.

Since the FAVOR method is used to from the geometry in the code, even the coarser grid $5^r \times 30^z$ results in a comparatively small difference of 1.5% from the finer grids. The benefit of using the FAVOR method to represent a complex geometry is very significant since accurate results can be obtained even with a coarse grid. This leads to great savings in computational time in simulations for complex geometries such as those used in LFC. Considering both accuracy and computational time, all subsequent calculations were performed with $15^r \times 90^z$ uniformly-spaced grid system for the cylindrical problem.

The simulation solutions are benchmarked against experimental data for EPS foam with density 24 kg/m³, coating thickness of 0.7 mm and metal front velocity of 1.5 cm/sec. As shown in Figure 5.3, the improved model with a varying heat transfer coefficient dependent on the gas pressure and orientation of gravity predicts the metal surface temperature better than the heat transfer coefficient model with only gravity effect. Considering the experimental uncertainty as shown in Figure 5.3, good agreement is obtained between the improved model and experiment.

The relation of correction factor for gas pressure and coating thickness is shown in Figure 5.4. As coating thickness increases, the pressure correction factor decreases. For different metal front velocities, a velocity factor of f_v is also applied.

$$f_v = \frac{V_g + V_m}{V_g} \tag{5.1}$$

where V_g is the characteristic speed of gravity waves defined by Equation (3.16);
V_m is the metal front velocity.

For the cylindrical geometry a parametric study was performed for coating thickness and metal front velocity. Figure 5.5(a) shows the mold fill time of the cylinder as a function of coating thickness. As the coating thickness increases, the heat transfer coefficient between the metal front and foam pattern decreases and the fill time increases. As the metal front velocity increases, the fill time decreases as shown in Figure 5.5(b).

5.1.2 Simple Plate with Three Ingates

To further illustrate the modified model with pressure effect, a numerical simulation is performed for a simple plate (28 × 15 × 1.3 cm) with two side ingates and a top ingate. The computational domain is shown in Figure 5.1(b) with L = 28 cm and W = 15 cm. The inlet height H is 12 cm. A foam of nominal density 20 kg/m³ and Aluminum alloy 319 (Si = 6%, Cu = 3.5%) were used. Grid independence was also performed on several grid densities $26^x \times 40^y$, $52^x \times 80^y$, $78^x \times 120^y$ and $104^x \times 160^y$. Since FAVOR method is used, there was less than 2% change for any two consecutive fine grids. Considering both accuracy and computational time, the following calculations were performed with $52^x \times 80^y$ uniformly-spaced grid system for the plate problem.

The numerical model was compared with the experimental data which is available in Shivkumar and Galois (1987). The experimental results of times of arrival of the metal front at different locations in the plate with hollow sprue and ingates are shown in Figure 5.6(a). Computer simulation results from the basic model of heat transfer coefficient with gravity effect are shown in Figure 5.6(b), and results from the improved model incorporating gas pressure and coating effect are shown in Figure 5.6(c). It is apparent that the heat transfer coefficient model with only gravity effect does not adequately predict the metal front location. The metal front tends to move faster through the bottom side sprue than that through the upper side sprue and the top one. The last place to fill in the plate is about 2 cm above the middle line of the plate in experiment which is almost the same as that predicted in the improved model, whereas the basic model of heat transfer coefficient with only gravity effect predicts the last place to fill in the plate is the middle of the plate at the right side. Figure 5.7 shows the mold filling time at the right side wall of the mold and better agreement was achieved by the improved model with varying heat transfer coefficient.

5.1.3 GM Box

In order to study and improve the LFC process, General Motors Corporation designed a test box with posts, partitions and sections of different thickness. The GM box is extensively used to study the effect of process variables in both experiment and computational modeling. The heat transfer coefficient model with gravity effect in FLOW-3D is very successful to predict the defect formation for the GM box with one ingate at the side with the thicker bottom (Hirt and Barkhudarov, 2002).

But with three gates and varying degrees of bead fusion, the basic model does not adequately model the filling sequence of different sections as well as defect formation. Experiments performed by Sand and Shivkumar (2005) showed a longer filling time in the upper part of the box as well as for the higher degrees of bead fusion. Figure 5.8 (a) and (b) show the mold filling times at various locations in the casting with average degree of fusion of 51% and 76%, respectively. The basic model in FLOW-3D with constant heat transfer coefficient and gravity effect can not capture this phenomenon as shown in Figure 5.9(a). But the improved model with varying heat transfer coefficient dependent on gas pressure and gravity effect predicted the filling times better as shown in Figure 5.9(b) and (c).

5.1.4 Effect of Metal Temperature

A plate pattern from Yao (1994) was used to validate the improved temperature model. The plate pattern 20×15×1.3 cm was placed horizontally with a side ingate of 1.3×1.8 cm in cross section. The computational domain is shown in Figure 5.1(c) with L = 20 cm and W = 15 cm. An effective metallostatic head of 28 cm was applied at the inlet boundary. The effect of temperature on the mold filling behavior was studied by using several different molten liquids. The initial temperatures obtained for wax, Sn, Al, and Cu are 225, 525, 750, and 1150°C, respectively. The molten liquid was rapidly poured into the pouring basin with preheated ladle. It was observed that inlet temperatures dropped about 35°C from the initial temperature. For the four inlet temperatures of 190, 490, 715 and 1115°C, the times of mold filling are shown in Figure 5.10 from experimental results. The filling times are 4.05, 2.1, 2.7 and 3.15 seconds for the four different temperatures, respectively. The results from numerical simulation were shown in Figure 5.11 for the four cases and the same filling behavior was captured by the simulation. The maximum filling speed at 490°C corresponds to the peak volatilization of EPS foam. For temperatures under 490°C, the degradation products consist mainly of viscous residue and increase the resistance to the molten liquid. For temperatures above 490°C, the volume of gases produced increases and mold filling speed is decreased to a certain extent dependent on the elimination of the foam products. The basic model with constant heat transfer coefficient could not simulate the temperature effect, but the improved model predicted the mold filling time closer to experimental data as evidenced in Figure 5.12, showing the good agreement between experiment and simulation for the mold filling time at the right surface of the mold. The coefficients of temperature c_T used for the simulation were listed in Table 5.1.

Table 5.1 Coefficient of Temperature for Different Metal Temperature

Metal Temperature (°C)	c_T
190	0.7
490	1.4
715	1.2
1115	1.0

5.1.5 Effect of Degree of Bead Fusion

The effect of bead fusion on the molding filling times from experiments (Yao, 1994) is shown in Figure 5.13. The arrow represents the position of the ingate. Figure 5.13(a) shows lower degree of bead fusion with foam density of 26 kg/m³, and Figure 5.13(b) shows higher degree of bead fusion with foam density of 21 kg/m³. It is obvious although density is an important property that has a strong effect on casting formation, the degree of bead fusion also plays an important role on the mold filling process. By applying the correction factor for bead fusion, the improved computational model can reasonably predict the filling times for foam patterns with different degree of bead fusion. The coefficient of bead fusion c_D was chosen to have a linear dependency on degrees of bead fusion as

$$c_D = 0.6\left(DOF_a\right) + 0.7 \tag{5.1}$$

Figure 5.14 shows simulation results of the molding filling times with the effect of bead fusion. Though Yao (1994) reported the difference in the mold filling was because of the variation in degrees of bead fusion, no quantification of the bead fusion was reported. By testing the values of bead degrees of fusion, it was found that in the computational study the assumed value of 50% and 70% for lower and higher degree of bead fusion gave good results. Figure 5.14(a) shows lower degree of bead fusion with foam density of 26 kg/m^3, and Figure 5.14(b) shows higher degree of bead fusion with foam density of 21 kg/m^3. Compared with the experimental results shown in Figure 5.13, good agreement was achieved by the modified model with correction factor of degree of bead fusion.

5.2 Defect Prediction

5.2.1 Simple Plate

For the plate with three ingates, the predicted locations where two surfaces met are different from the two models as shown in Figure 5.15(a) and (b). Since the filling times are predicted more precisely by the improved model, it is safer to assume that more realistic defect formation can be predicted by the improved model as shown in Figure 5.15(b). One important observation is that there are many internal defects formed due to the meeting of two metal fronts predicted by the improved model. Because of the inclusion of gas pressure effect in the improved model, the defect near the bottom of the casting predicted in the basic model moves upwards into the casting and forms internal defects.

The use of three ingates causes several metal fronts to meet during the molding filling process which leads to internal inclusions of foam products. To check if fewer gates can help reduce defect formation, a two-gate model is tested and shown in Figure

5.15(c). The simulation results show that the defect at the right upper side of the casting is eliminated because of the removal of the top ingate. It is great encouragement that the model provides considerable amount of useful insight into the processes responsible for defect formation and final distribution in a cast part.

5.2.3 GM Box

The prediction of defect formation for the GM box is shown in Figure 5.16. Since the filling times are predicted more precisely by the improved model, it is safer to assume that more realistic defect formation can be predicted by the improved model as shown in Figure 16(b). It is observed that defects tend to form near the center of the box in the improved model while in the basic model it is on the lower part of the box.

The defect model needs further experimental comparisons to correlate the predictions with actual defects. Without more detailed validation, it is impossible to assign any significance to the absolute values of the defect scalar. However, the model can reveal useful insight into the process variables that are responsible for defect generation and final distribution in castings.

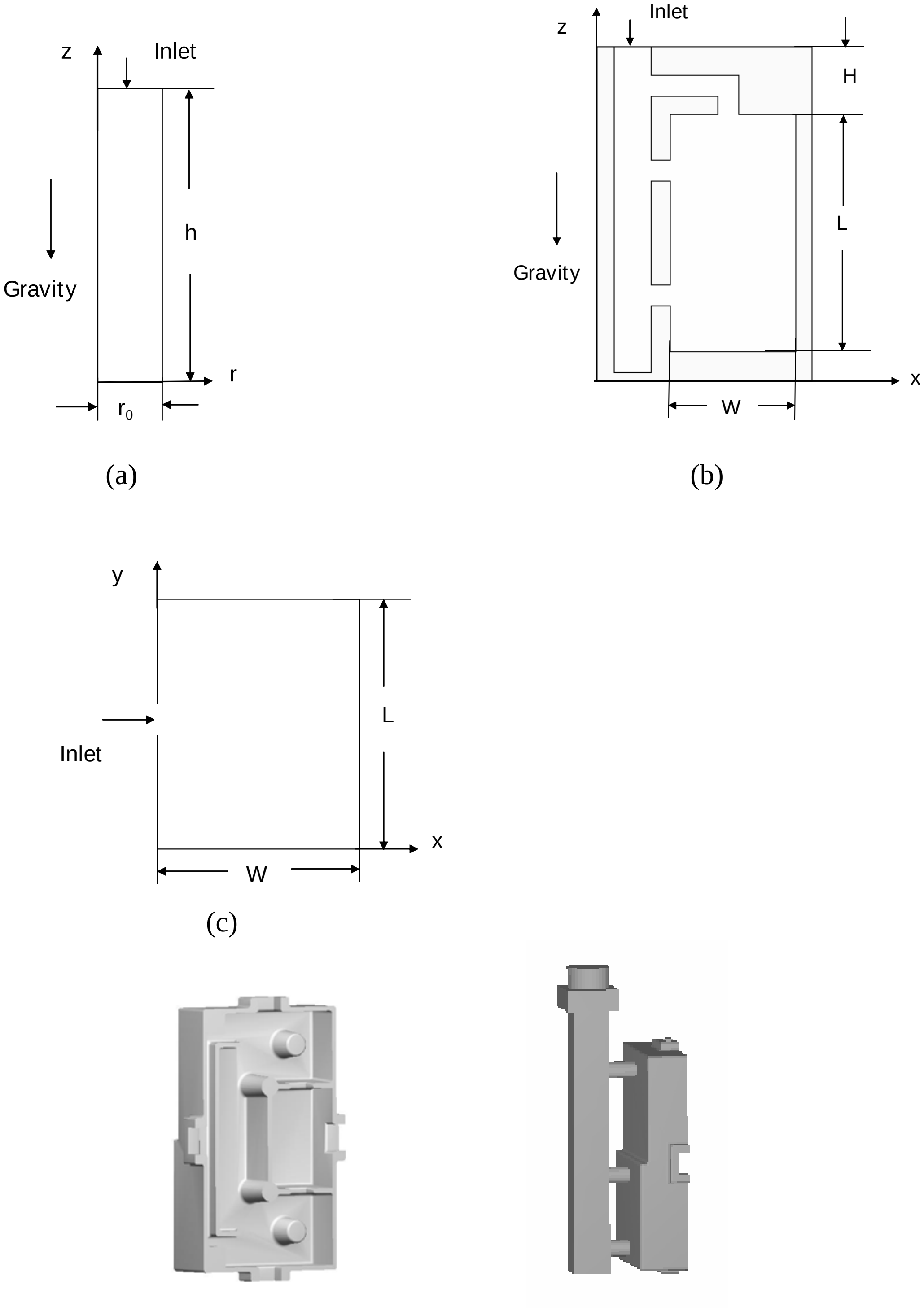
z
Inlet
h
Gravity
r
r_0
z
Inlet
H
L
Gravity
x
W
y
L
Inlet
x
W

(a)

(b)

(c)

(d)

(e)

Figure 5.1 Computational domains: (a) cylinder, (b) plate with 3 ingates, (c) plate with side ingate, (d) GM box, and (d) GM box with sprue configuration

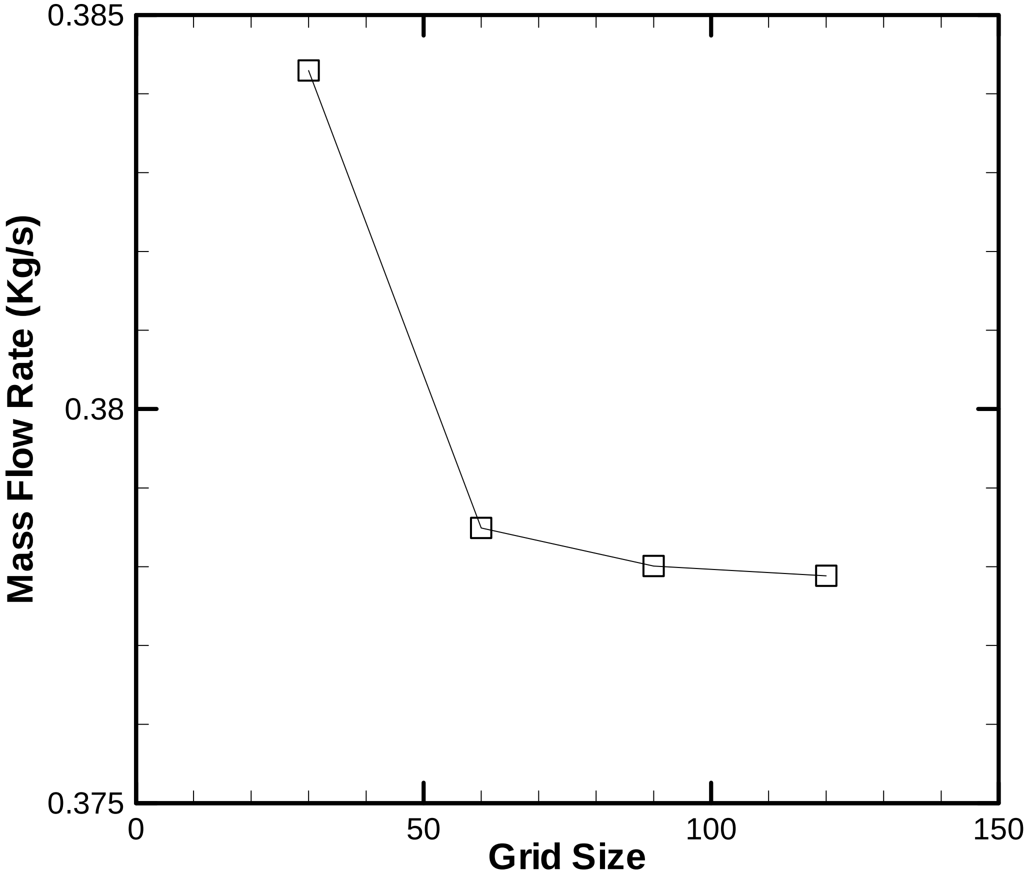

Figure 5.2 The mass flow rate at the entrance of the gate as a function of the grid size in the longitudinal direction

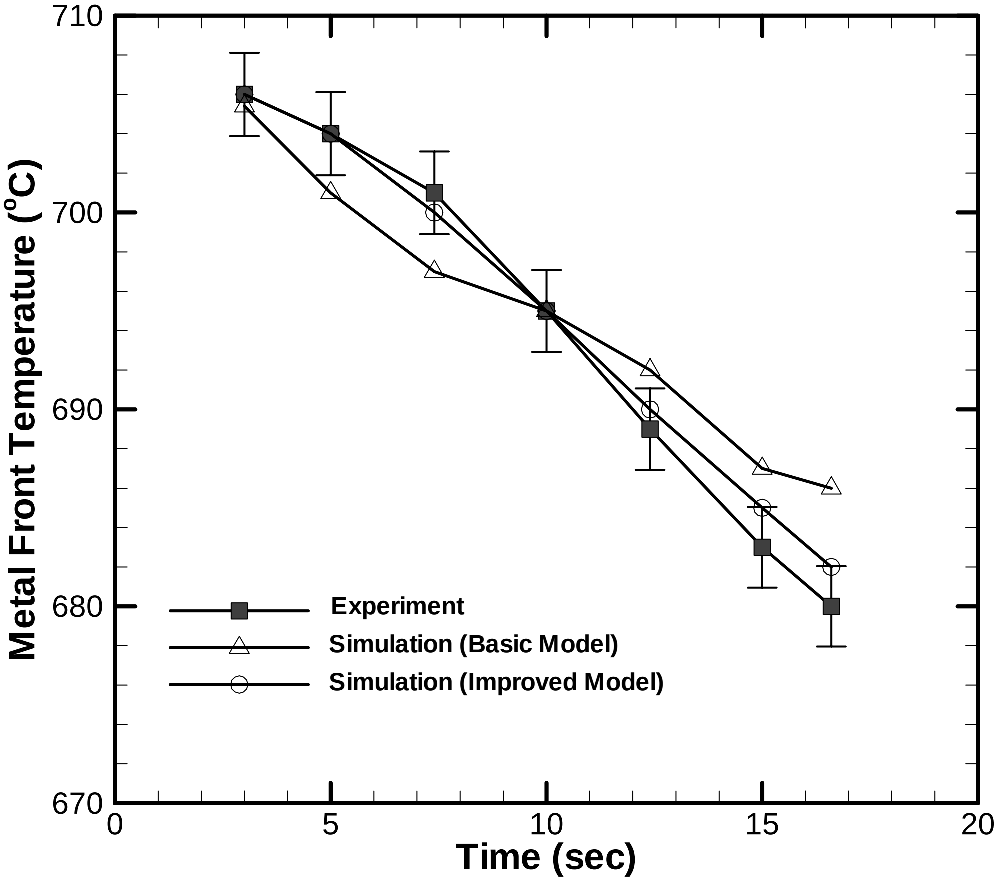

Figure 5.3 Experimental validation of basic model with gravity effect and improved model with varying heat transfer coefficient dependent on gas pressure for EPS foam with density 24kg/m³, coating thickness of 0.7 mm and metal front velocity of 1.5 cm/sec

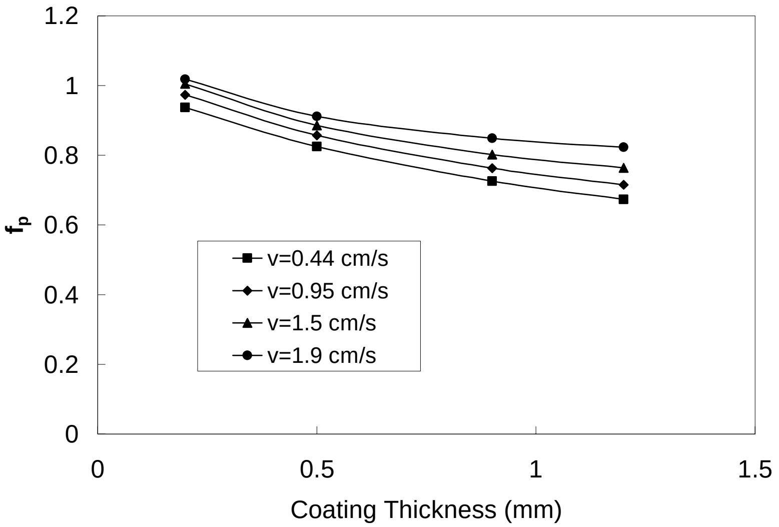

Figure 5.4 Relation between correction factor for gas pressure and coating thickness

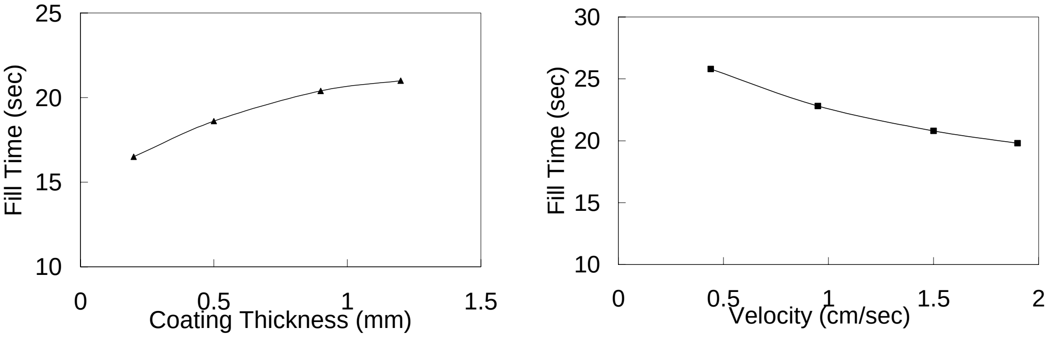

(a) (b)

Figure 5.5 Mold fill time as a function of (a) coating thickness and (b) metal front velocity

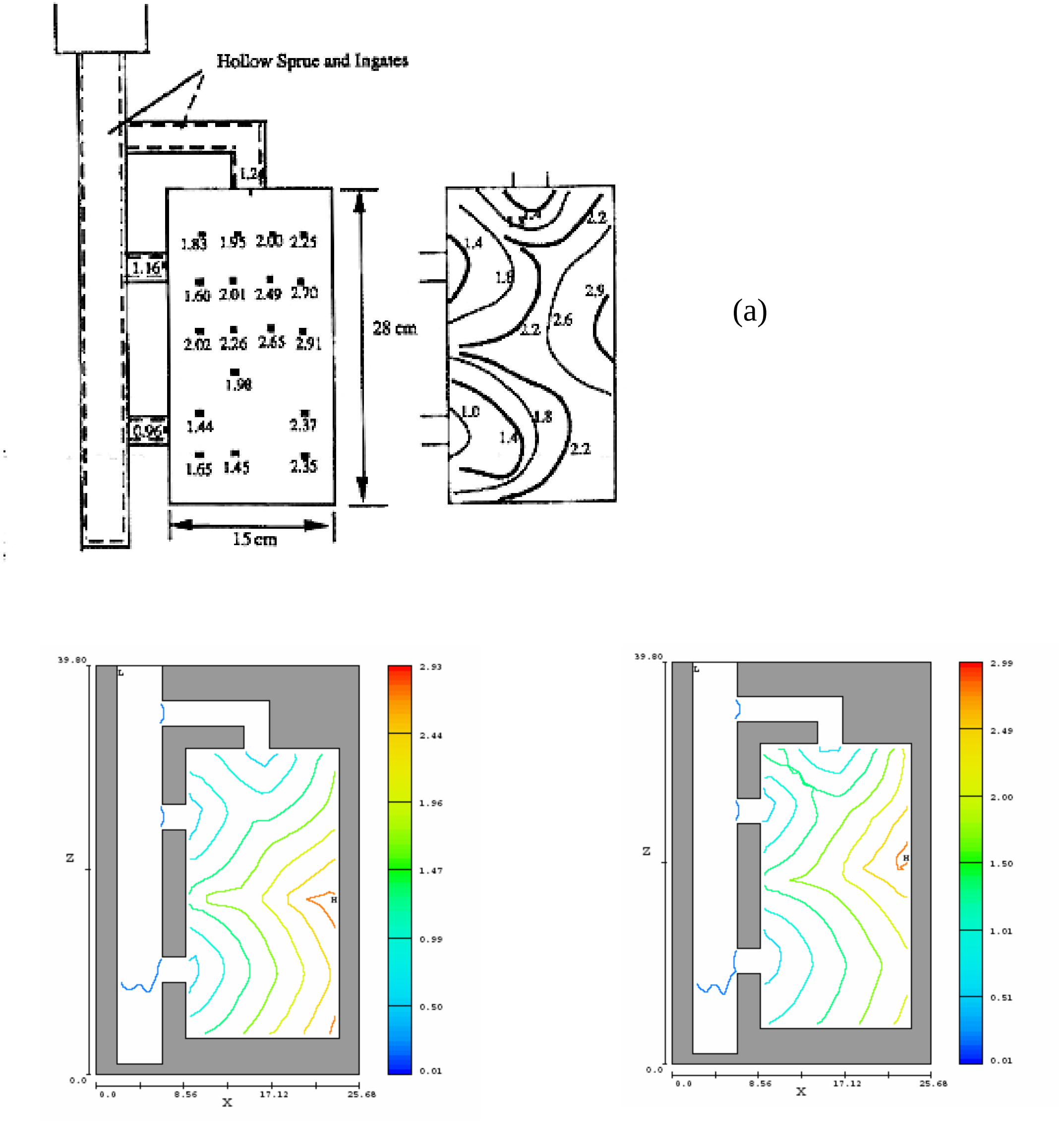

(a)

(b) (c)

Figure 5.6 Comparison of mold filling times for a plate pattern: (a) measured values by thermometric technique (Shivkumar and Galois, 1987), (b) simulation filling times based on heat transfer coefficient model with gravity effect, and (c) simulation filling times filing times based on the modified model with heat transfer coefficient based on both gas pressure and coating thickness

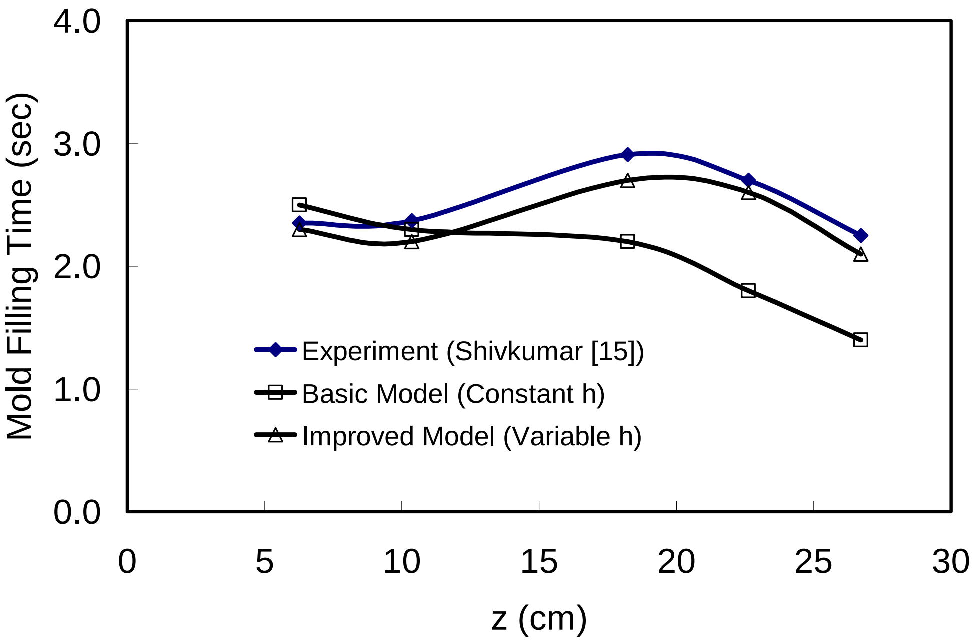

Figure 5.7 Mold filling time at the right wall of the mold for the plate pattern with 3 ingates

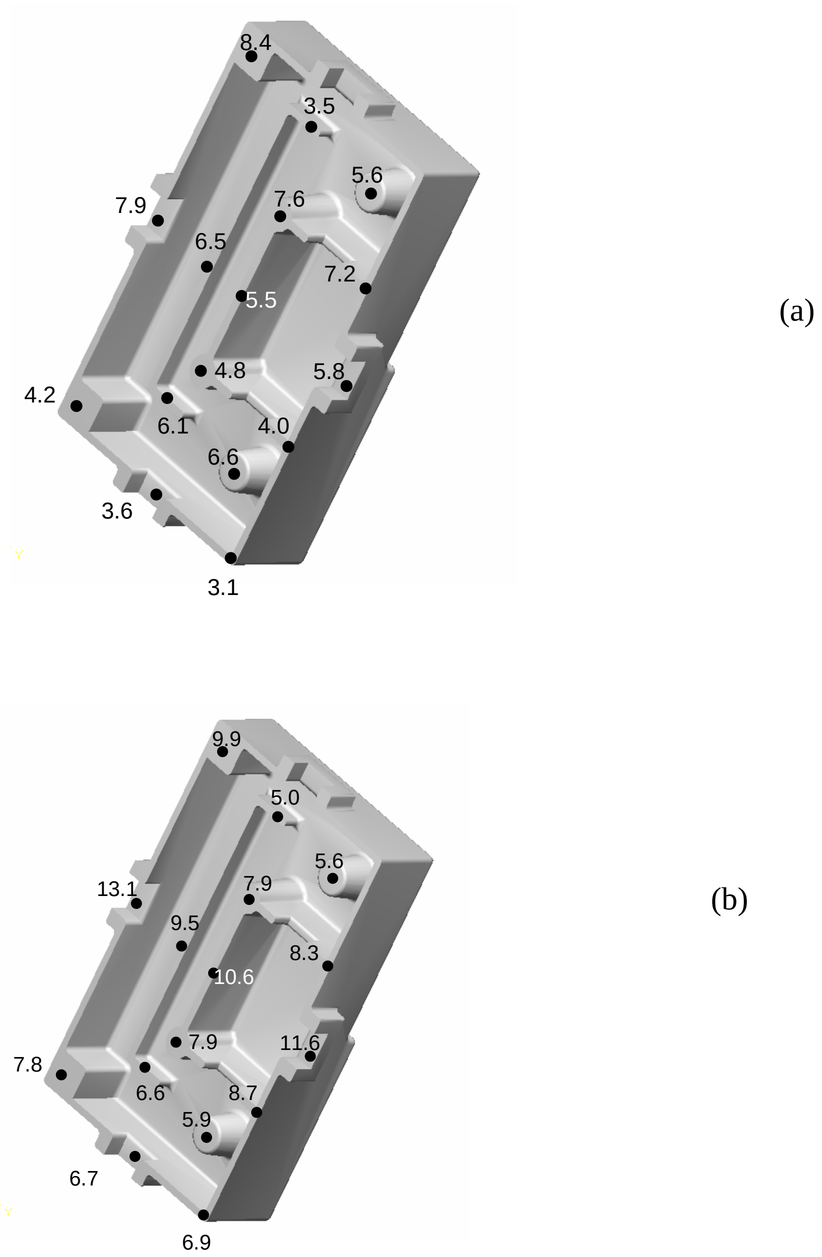
8.4
3.5
5.6
7.9
7.6
6.5
7.2
5.5
(a)
4.8
5.8
4.2
6.1
4.0
6.6
3.6
3.1
9.9
5.0
5.6
13.1
7.9
(b)
9.5
8.3
10.6
7.9
11.6
7.8
6.6
8.7
5.9
6.7
6.9

Figure 5.8 Mold filling times at various locations in the casting with 3 side gates for a foam pattern with average degree of fusion of 76% for (a) and 51% for (b). The filling time was determined from the responses of chromel-alumel thermocouples positioned at various locations during the production of the casting (Sand and Shivkumar, 2005)

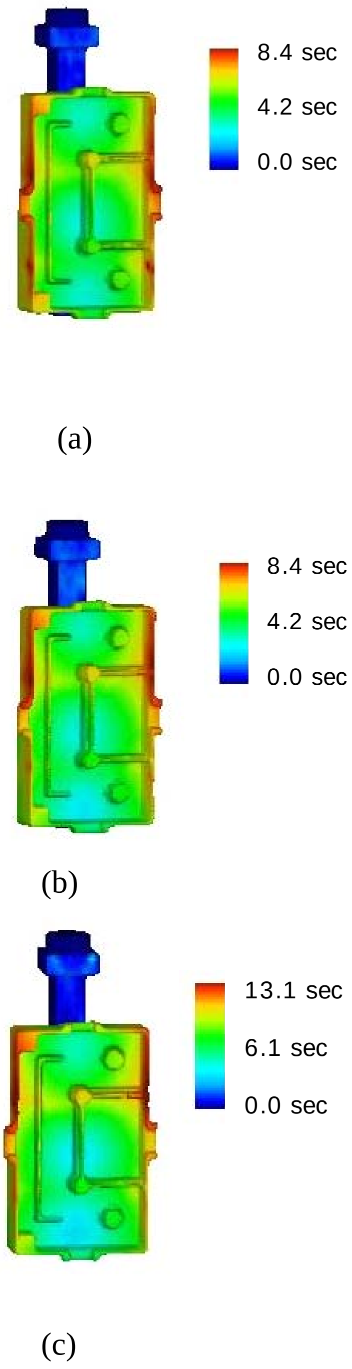

Figure 5.9 Comparisons of filling times predicted by the two models: (a) default heat transfer model with gravity effect, and (b) and (c) modified model with heat transfer coefficient based on both gas pressure and coating thickness for average degree of bead of fusion 51% and 76%. Color indicates time of filling (blue is earliest and red latest)

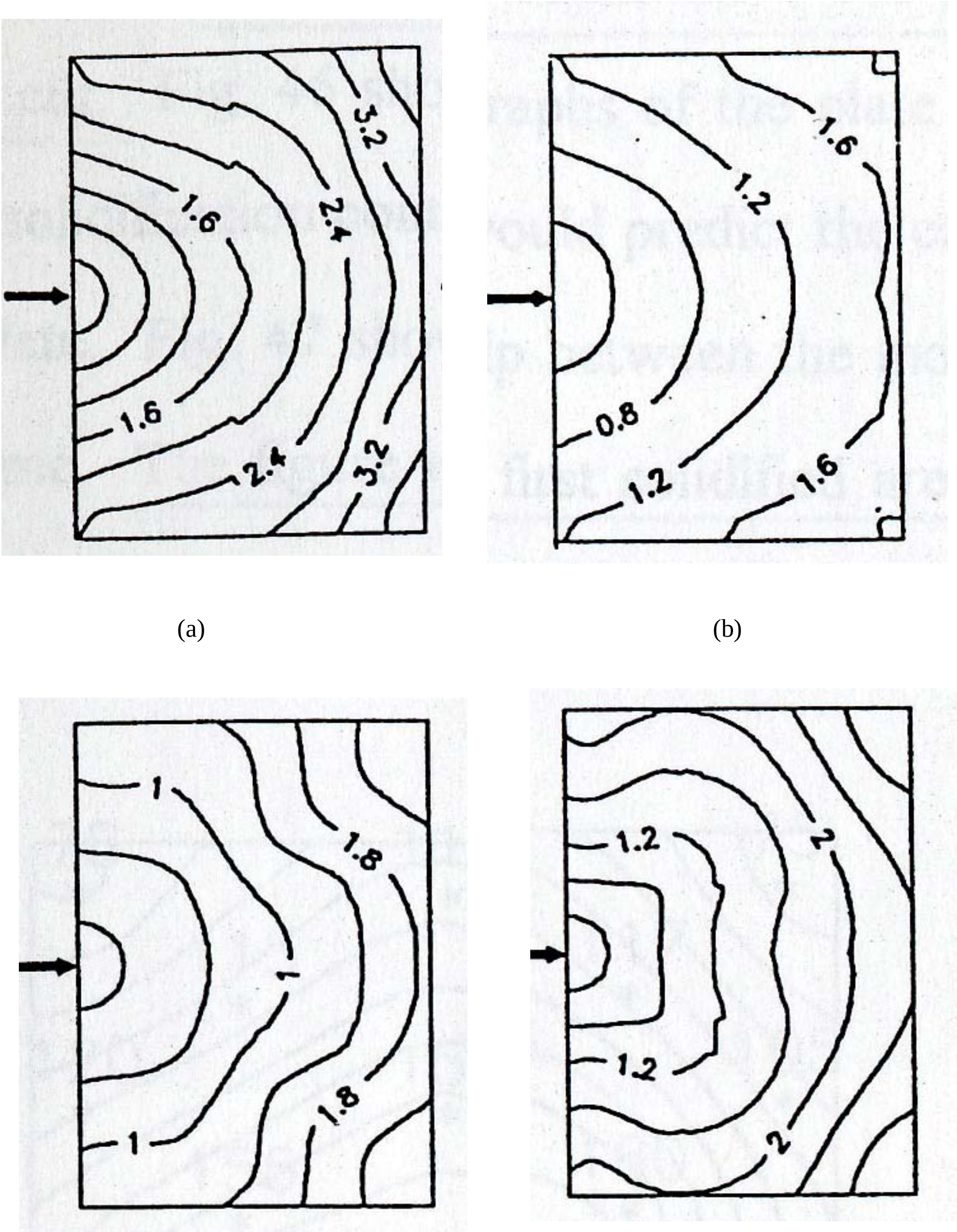

(a) (b)

(c) (d)

Figure 5.10 Experimental results for Yao (1994) showing the temperature effect on the molding filling times. The arrow represents the position of the ingate: (a) 190°C, (b) 490°C, (c) 715°C, and (d) 1115°C

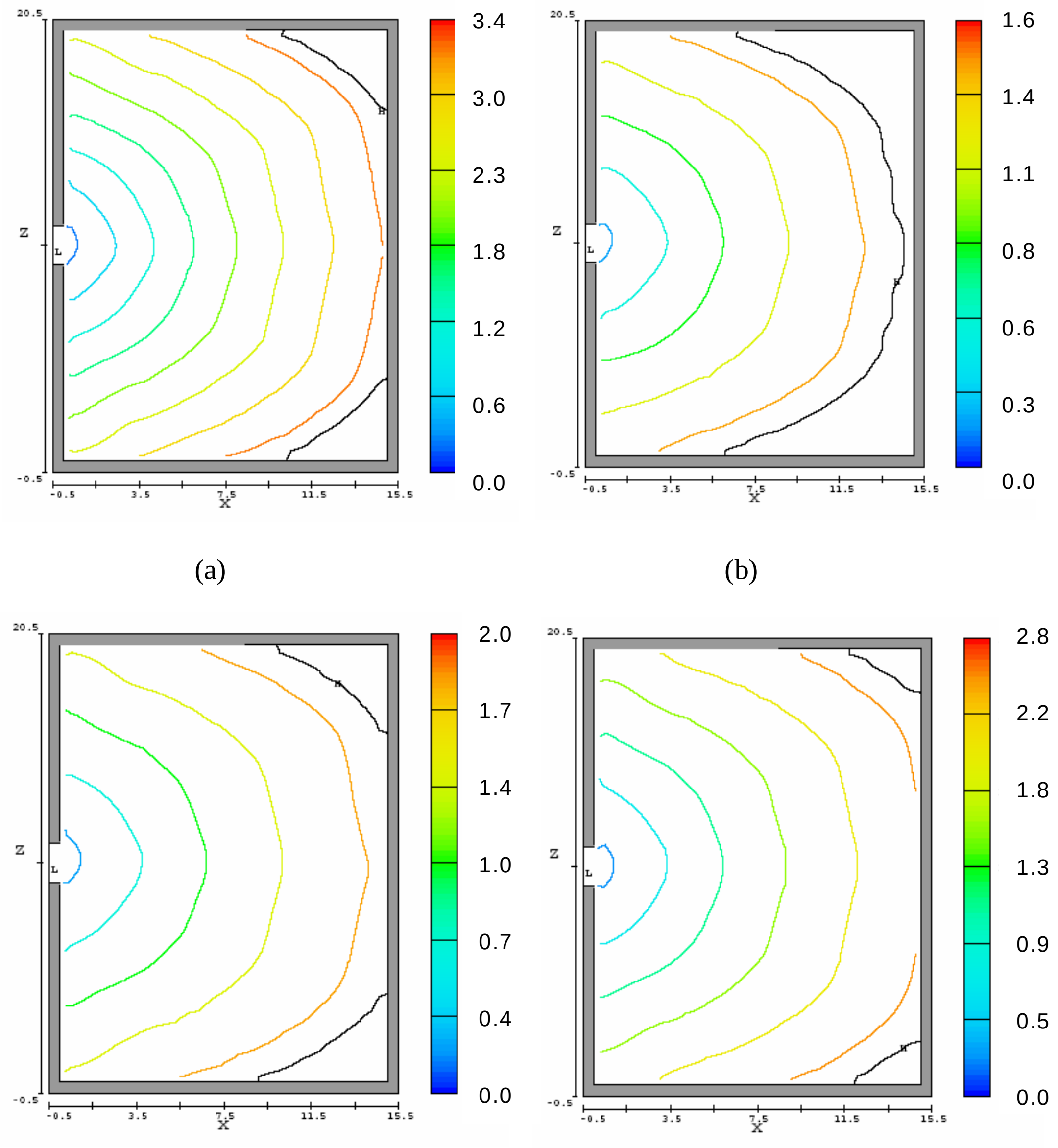

(a) (b)

(c) (d)

Figure 5.11 Simulation results showing the temperature effect on the molding filling times. Color indicates time of filling (blue is earliest and red latest): (a) 190°C, (b) 490°C, (c) 715°C, and (d) 1115°C

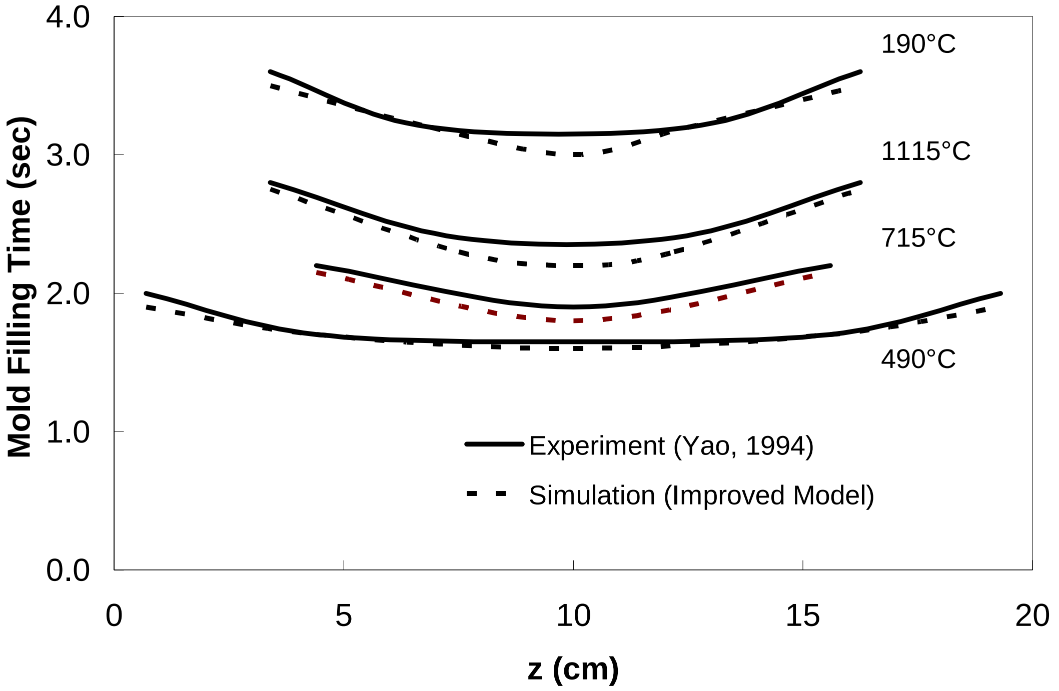

Figure 5.12 Mold filling time at the right side surface of mold showing the temperature effect

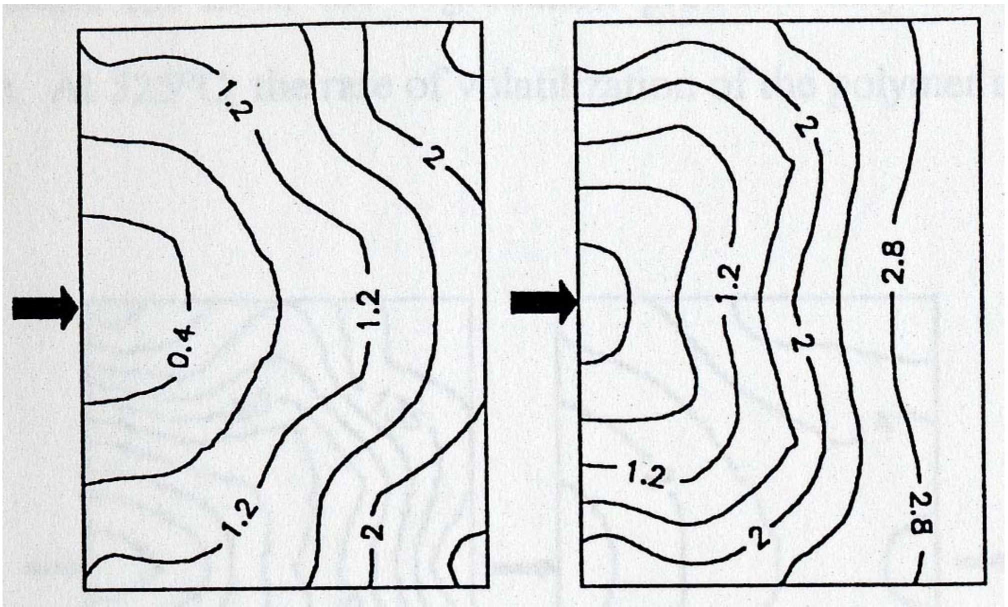

(a) (b)

Figure 5.13 Experimental results for Yao (1994) showing the effect of bead fusion on the molding filling times. The arrow represents the position of the ingate: (a) lower degree of bead fusion with foam density of 26 kg/m³, and (b) higher degree of bead fusion with foam density of 21 kg/m³

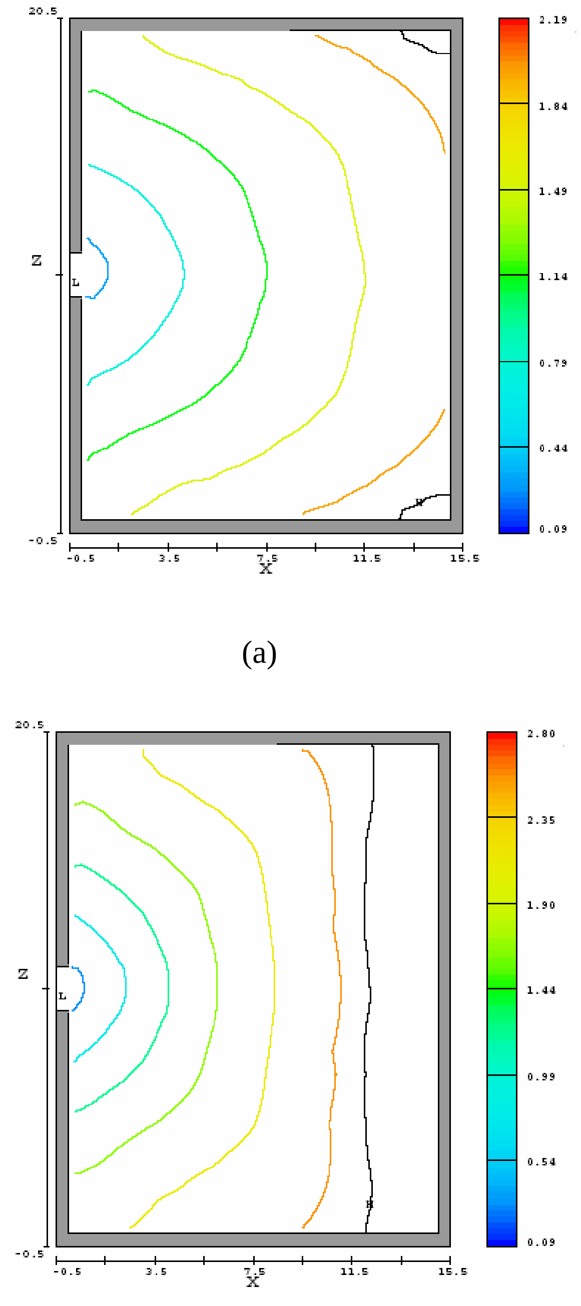

(a)

(b)

Figure 5.14 Simulation results showing the effect of bead fusion on the molding filling times. Color indicates time of filling (blue is earliest and red latest): (a) lower degree of bead fusion with foam density of 26 kg/m³, and (b) higher degree of bead fusion with foam density of 21 kg/m³

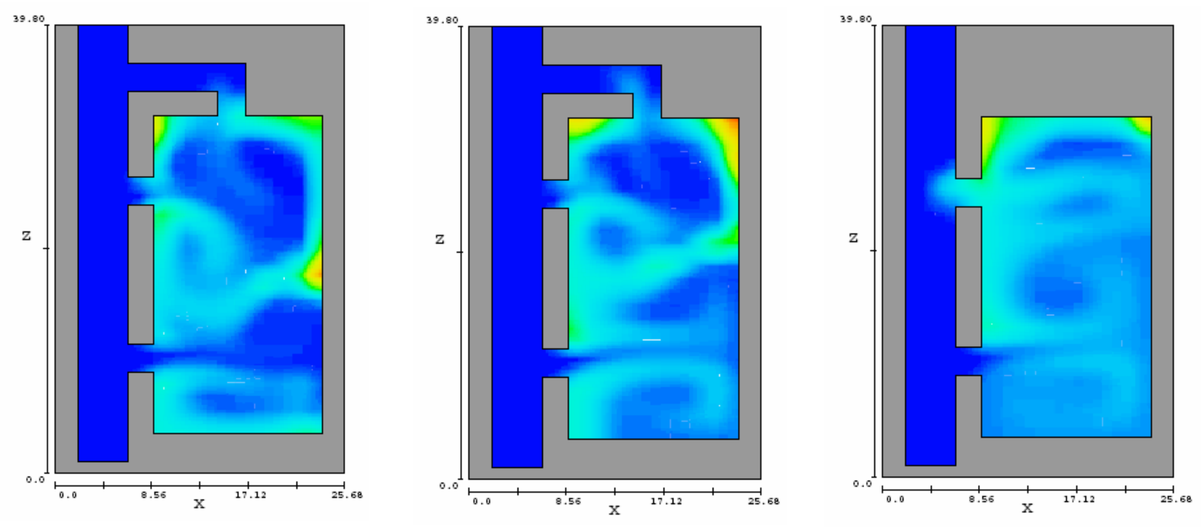

(a) (b) (c)

Figure 5.15 Defect formation predicted by (a) basic heat transfer coefficient model with gravity effect, (b) improved model with heat transfer coefficient based on both gas pressure and coating thickness, and (c) improved model for two ingates. Color represents probability for defects (blue is the lowest and red highest)

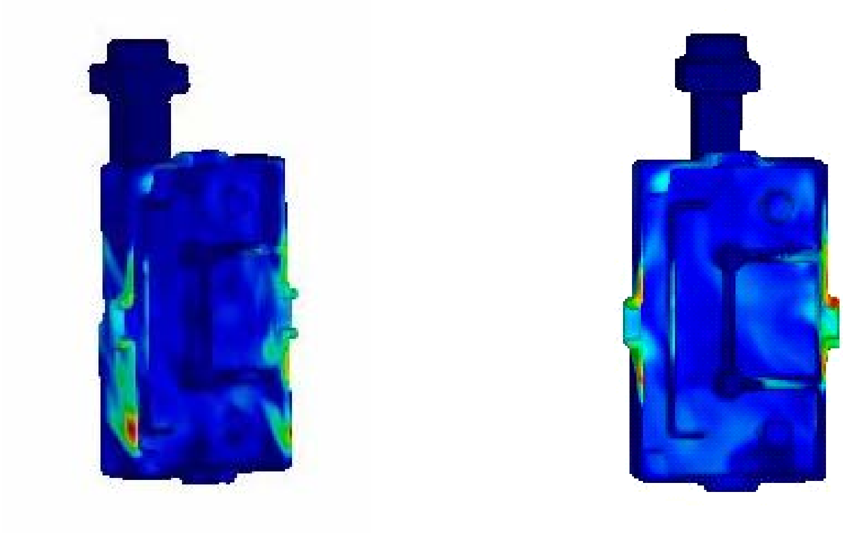

(a) (b)

Figure 5.16 Comparisons of defect formation predicted by the two models: (a) basic heat transfer model with gravity effect, and (b) improved model with heat transfer coefficient based on gas pressure. Color represents probability for defects (blue is the lowest and red highest)

CHAPTER 6 CONCLUSIONS

This investigation of lost foam casting has led to a better understanding of the effects of foam density and simulated metal front velocity in the LFC process. Results from both the visualization and realistic top-down experiments confirm that there is a gaseous gap in the metal front during the LFC process for the temperature range of aluminum casting.

It is concluded that, unlike the fluidity of the molten metal, which is highly dependent on the density of the foam patterns, foam density has a marginal effect on the heat flux and heat transfer coefficient from the metal front to the foam pattern. The heat flux and heat transfer coefficient keep increasing in the casting process until the foam pattern is fully consumed. It has been shown that the heat transfer coefficient between the casting and foam pattern cannot be considered constant when modeling the lost foam casting process. The values of heat transfer coefficients, initially 150 $W/m^2 \cdot K$ gradually increased to 220 ~ 300 $W/m^2 \cdot K$ to the end of the process. This finding will be very useful to better model the lost foam casting process leading to improvements in casting quality.

It is also concluded that higher foam density and faster simulated metal front speed give rise to a higher pressure in the gap between the metal front and the foam pattern while the metal front velocity is less than 0.95 cm/s. The gap pressure is highly dependent on the metal front velocity and with a metal front velocity of 1.5 cm/s the EPS foam density does not greatly influence the gap pressure. In temperature range of 730°C to 850°C for aluminum alloy, the effect of metal surface temperature is shown to be insignificant because the process is controlled by the foam decomposition process instead of the characteristics of molten metal.

Computational models can be used to simulate combined effects of fluid flow, heat transfer and foam decomposition during the LFC process. By using the FAVOR method, a complex geometry can be meshed efficiently. An improved model with varying heat transfer coefficient incorporated gas pressure, metal temperature, foam property and coating effect was developed into the user defined subroutine. The simulation results from the improved model showed improved agreement with experimental observations and data reported in the literature. Metal front temperature was predicted by the improved model within experimental uncertainty, whereas the prediction made by the basic model had a much larger difference from experimental measurements. Mold filling patterns and filling time difference of 1 to 4 seconds were more precisely captured by the improved model than by the basic model for several geometries. The improved code can also be used to predict flow condition of molten metal, filling sequence, and defect formation for different geometries and process variables. This information can provide the casting industry a powerful and reliable tool to analyze and optimize process and design variables.

REFERENCES

Abayarathna, S.S.S. and Tasi, H.L., 1989. Modeling of Evaporative Pattern Process, Part III: Heat/Mass Transfer in Sand Mold and Its Effect on Casting Solidification. Transactions of the American Foundrymen's Society, 97: 653-660.

Abayarathna, S.S.S. and Tsai, H.L., 1989. Modeling of Evaporative Pattern Process Part II: Determination of Possible Carbon Pickup. Transactions of the American Foundrymen's Society, 97: 645-652.

Anderson, M.J. and Whicomb, P., J., 2000. DOE Simplified - Practical Tools for Effective Experimentation.

Barkhudarov, M.R. and Hirt, C.W., 1998. Tracking Defects. In: M. Tiryakioglu and J. Campbell (Editors), Proceedings from Materials Solutions Conference 1998 on Aluminum Casting Technology, Rosemont, Illinois, pp. 63-68.

Barnett, L., 2002. Improved Lost Foam Casting Reduces Energy Use, Waste, and Emissions, while Lowering Product Defects and Cost.

Barone, M.R. and Caulk, D.A., 2005. A Foam Ablation Model for Lost Foam Casting of Aluminum, General Motors Research and Development Center.

Bates, C.E., Littleton, H.E., McMellong, B. and Stroom, P.A., 2001. Technological Developments and Worldwide Market Growth in Lost Foam Casting Production. Transactions of the American Foundrymen's Society, 105: 1557-1572.

Bhat, R.C., Bhavnani, S.H., Overfelt, R.A. and Sheldon, D., 2005. Effect of Process and Design Variables in the Production of Expandable Polystyrene for Lost Foam Casting. TMS (The Minerals, Metals, & Materials Society), Light Metals. 2005: 1101-1106.

Cai, M., Siak, J., Powell, B.R., Nouaime, G. and Swarin, S.J., 2002. Physical and Chemical Analysis of the Thermal Degradation Products of Expanded Polystyrene Patters with Short Thermal Exposure. Transactions of the American Foundrymen's Society, 110(2): 1463-1481.

Campbell, J., 1993. Invisible Macrodefects in Castings. Journal de Physique IV, 3: 861-872.

Celotto, M., Biederman, S. and Shivkumar, S., 1994. Influence of Foam Processing Variables on Polymer Degradation and Flow Behavior in the EPC Process. Transactions of the American Foundrymen's Society, 102: 977-983.

Chang, F.C. and Tsai, H.L., 1989. Numerical Study of Fluidity in Evaporative Pattern Process Including Latent Heat Effect. Transactions of the American Foundrymen's Society, 97: 521-528.

Chen, Y.-F., Chen, R.-C. and Hwang, W.-S., 1997. Mold-Filling Study in the EPC Process - Mathematical Model and Flow Characteristics. Transactions of the American Foundrymen's Society, 105: 459-464.

Davis, J.R. (Editor), 1990. Physical Properties of Carbon and Low-Alloy Steels, Metals Handbook, tenth edition, volume 1, 195-199.

Duff, E.S., 1999. Fluid Flow Aspects of Solidification Modeling: Simulation of Low Pressure Die Casting. Ph.D. Thesis, The University of Queensland.

Flow Science, http://www.flow3d.com/.

Flow Science, 2005. Flow-3D User's Manual.

Garland, B., 2003. DOE-Industry Partnerships at Work: Lost Foam Casting Research.

Goria, C.A., Serramoglia, G., Caironi, G. and Tosi, G., 1986. Coating Permeability: A Critical Parameter of the Evaporative Pattern Process. Transactions of the American Foundrymen's Society, 94: 589-600.

Green, J.J., Ramsay, C.W. and Askeland, D.R., 1998. Formation of Surface Defects in Gray Iron Lost Foam Castings. Transactions of the American Foundrymen's Society, 106: 339-347.

Hill, M.W., Lawrence, M., Ramsay, C.W. and Askeland, D.R., 1997. Influence of Gating and Other Processing Parameters on Mold Filling in the LFC Process. Transactions of the American Foundrymen's Society, 105: 443-450.

Hill, M.W., Vrieze, A.E., Moody, T.L., Ramsay, C.W. and Askeland, D.R., 1998. Effect of Metal Velocity on Defect Formation in Al LFCs. Transactions of the American Foundrymen's Society, 106: 365-374.

Hirt, C.W., 1993. Volume-Fraction Techniques: Powerful Tools for Wind Engineering. Journal of Wind Engineering and Industrial Aerodynamics, 46&47: 327-338.

Hirt, C.W., 1999. Modeling the Lost Foam Process with Defect Predictions - Progress Report: Lost-Foam Model Extensions, Wicking. FSI-03-TN45-1, Flow Science, Inc.

Hirt, C.W. and Barkhudarov, M.R., 1997. Modeling the Lost Foam Process with Defect Prediction. FSI-97-TN45, Flow Science, Inc.

Hirt, C.W. and Barkhudarov, M.R., 2002. Technology in Progress: Predicting Defects in Lost Foam Castings. Modern Casting, 92(12): 31-33.

Hirt, C.W. and Nichols, B.D., 1981. Volume of Fluid (VOF) Method for the Dynamics of Free Boundaries. Journal of Computational Physics, 39(1): 201-225.

Houzeaux, G. and Codina, R., 2004. A Finite Element Model for the Simulation of Lost Foam Casting. International Journal for Numerical Methods in Fluids, 46(2): 203-226.

Hwang, W.S. and Stoehr, R.A., 1983. Fluid Flow Modeling for Computer-Aided Design of Castings. Journal of Metals, Oct: 22-29.

Khan, S., C., R., Naylor, D. and D.G.R., S., 2000. Measurement of the Interfacial Heat Transfer Coefficient in Lost Foam Casting of A356 Al Alloy. Transactions of the American Foundrymen's Society, 108: 445-452.

Khan, S., Naylor, D. and C., R., 2001. Effect of Casting Section Thickness and Coating Thickness on the Interfacial Heat Transfer Coefficient in Lost Foam Casting. Transactions of the American Foundrymen's Society, 109: 1495-1502.

Kline, S.J. and McClintock, F.A., 1953. Describing Uncertainties in Single-Sample Experiments. Mechanical Engineering, 75(1): 3-9.

Kuo, J.-H., Chen, J.-C., Pan, Y.-N. and Hwang, W.-S., 2003. Mold Filling Analysis in Lost Foam Casting Process for Aluminum Alloys and Its Experimental Validation. Materials Transactions, 44(10): 2169-2174.

Lawrence, M.D., 1998. Some Observations and Principles for Gating of Lost Foam Casting. Transactions of the American Foundrymen's Society, 106: 349-356.

Lessiter, M.J., 1994. Expendable Pattern Casting: State of the Process. Modern Casting, 84(1): 36-38.

Lessiter, M.J., 1996. Innovations in Controlling the Lost Foam Process. Modern Casting, 86(1): 45-48.

Lessiter, M.J., 1997. Today's Lost Foam Technology Differs from Yesteryear. Modern Casting, 87(4): 32-35.

Lessiter, M.J., 2000. A Look Back at the 20th Century (Part 10) - Lost Foam Casting. Modern Casting, 90(11): 54-55.

Liu, J., Ramsay, C.W. and Askeland, D.R., 1997. A Study of Foam-Metal-Coating Interaction in the LFC Process. Transactions of the American Foundrymen's Society, 105: 419-425.

Liu, X., 1995. The Mechanism of Mold Filling and Casting Defect Formation in the Lost Foam Casting Process. Ph.D. Dissertation, University of Missouri-Rolla.

Liu, X., Ramsay, C.W. and Askeland, D.R., 1994. A Study of Mold Filling Control Mechanism in Expendable Pattern Casting Process. AFS Transactions, 102: 903-914.

Liu, X.J., Bhavnani, S.H. and Overfelt, R.A., 2004. Measurement of Kinetic Zone Temperature and Heat Transfer Coefficient in the Lost Foam Casting Process, 2004 American Society of Mechanical Engineers, Heat Transfer Division, v 375, n 3, Proceedings of the ASME Heat Transfer Division, p 411-418.

Liu, X.J., Bhavnani, S.H. and Overfelt, R.A., 2003. The Effects of Foam Density and Metal Velocity on the Heat and Mass Transfer in the Lost Foam Casting Process, Proceedings of the ASME Summer Heat Transfer Conference, v 2003, p 317−323.

Liu, Y., 2001. Foam Degradation and Mold Filling in Lost Foam Casting Aluminum Alloy. M.S. Thesis, Auburn University.

Liu, Y., Bakhtiyarov, S.I. and Overfelt, R.A., 2002. Numerical Modeling and Experimental Verification of Mold Filling and Evolved Gas Pressure in Lost Foam Casting Process. Journal of Materials Science, 37(14): 2997-3003.

Mazouz, K., 2000. The Design and Manufacture of Fire Hydrants, http://www.firehydrant.org/info/design_manufacture_elissa_wahlstrom.html.

Mehta, S., Biederman, S. and Shivkumar, S., 1995. Thermal Degradation of Foam Polystyrene. Journal of Materials Science, 30: 2944-2949.

Miller, B.A., 1996. Pattern Pyrolysis Defect Reduction in Lost Foam Casting. M.S. Thesis Thesis, University of Alabama, Birmingham.

Mirbagheri, S.H.M., Silk, J.R. and Davami, P., 2004. Modeling of Foam Degradation in Lost Foam Casting Process. Journal of Materials Science, 39(14): 4593-4603.

Mirbagheri, S.M.H., Esmaeileian, H., Serajzadeh, N., Varahram, N. and Davami, P., 2003. Simulation of Melt Flow in Coated Mould Cavity in the Casting Process. Journal of Processing Technology, 142: 493-507.

Mirbagheri, S.M.H., Varahram, N. and Davami, P., 2003. 3D Computer Simulation of Melt Flow and Heat Transfer in the Lost Foam Casting Process. International Journal for Numerical Methods in Engineering, 58(5): 723-748.

Molibog, T.V., 2002. Modeling of Metal/Pattern Replacement in the Lost Foam Casting Process. Ph.D. Dissertation, University of Alabama, Birmingham.

Pan, E.N. and Liao, K.Y., 2000. Study on Flowability of EPC A356 Al Alloy. Transactions of the American Foundrymen's Society, 106: 233-242.

Ramsey, F.L. and Schafer, D.W., 2002. The Statistical Sleuth - A Course in Methods of Data Analysis. Thomson Learning.

Reynolds, J., 1999. "Shop floor" Process Control for Lost Foam. Modern Casting, 89(5): 53-56.

Rossacci, J. and Shivkumar, S., 2003. Bead Fusion in Polystyrene Foams. Journal of Materials Science, 38(11): 201-206.

Rossacci, J. and Shivkumar, S., 2003. Influence of EPS Bead Fusion on Pattern Degradation and Casting Formation in the Lost Foam Process. Journal of Materials Science, 38(11): 2321-2330.

Salah, D., Eigenfeld, K. and Tilch, W., 2002. Reactive Lost Foam Coating, Proceedings of the 65th World Foundry Congress, Gyeongju, Korea, 2002.

Sands, M. and Shivkumar, S., 2003. EPS Molecular Weight and Foam Density Effects in the Lost Foam Process. Journal of Materials Science, 38(10): 2233-2239.

Sands, M. and Shivkumar, S., 2003. Influence of Coating Thickness and Sand Fineness on Mold Filling in the Lost Foam Casting Process. Journal of Materials Science, 38(4): 667-673.

Sands, M. and Shivkumar, S., 2005. EPS Bead Fusion Effects on Fold Defect Formation in Lost Foam Casting of Aluminum Alloys. 0022-2461, Worcester Polytechnical Engineering.

Sheldon, D.S., 2002. The Evolution of Sand Fill and Compaction Equipment for Lost Foam Casting. Transactions of the American Foundrymen's Society, 110(2): 1357-1370.

Shivkumar, S., 1994. Modeling of Temperature Losses in Liquid Metal during Casting Formation in Expendable Pattern Casting Process. Materials Science and Technology, 10: 986-992.

Shivkumar, S. and Gallois, B., 1987. Physico-Chemical Aspects of the Full Mold Casting of Aluminum Alloys, Part I: The Degradation of Polystyrene. Transactions of the American Foundrymen's Society, 95: 791-800.

Shivkumar, S. and Gallois, B., 1987. Physico-Chemical Aspects of the Full Mold Casting of Aluminum Alloys, Part II: Metal Flow in Simple Patterns. Transactions of the American Foundrymen's Society, 95: 801-812.

Shivkumar, S., Wang, L. and Apelian, D., 1990. The Lost-foam Casting of Aluminum Alloy Components. JOM, 42(11): 38-44.

Shivkumar, S., Yao, X. and Makhlouf, M., 1995. Polymer-Melt Interactions during Casting Formation in the Lost Foam Process. Scrita Metallurgica *et* Materialia, 33(1): 39-46.

Shroyer, H.F., 1958. Cavity-less Casting Mold and Method of Making Same, U.S. Patent No. 2,830,343.

Smith, B.V. and Biederman, S., 2000. Examining Lost Foam's 'White Side'. Modern Casting, 90(8): 30-34.

Smith, T.R., 1964. Method of Casting, U.S. Patent No. 3,157,924.

Sun, W., Scarber, P. and Littleton, H., 2004. Validation and Improvement of Computer Modeling of the Lost Foam Casting Process via Real Time X-ray Technology, Multiphase Phenomena and CFD Modeling and Simulation in Materials Processes, Mar 14-18 2004. Multiphase Phenomena and CFD Modeling and Simulationin Materials Processes. Minerals, Metals and Materials Society, Warrendale, United States, Charlotte, NC., United States, pp. 245-251.

Sun, Y., 1992. Transport of Polystyrene Decomposition Products and its Role in Controlling Casting Defects in Aluminum EPS Castings. Ph.D. Thesis, University of Missouri-Rolla.

Sun, Y., Tsai, H.L. and Askeland, D.R., 1996. Effects of Silicon Content, Coating Materials and Gating Design on Casting Defects in the Aluminum Lost Foam Process. Transactions of the American Foundrymen's Society, 104: 271-279.

Tsai, H.L. and Chen, T.S., 1988. Modeling of Evaporative Pattern Process, Part I: Metal Flow and Heat Transfer During the Filling Stage. Transactions of the American Foundrymen's Society, 96: 881-890.

Tseng, C. and Askeland, D.R., 1991. A Study of Selected Process Parameters for the Evaporative Pattern Casting Process. Transactions of the American Foundrymen's Society, 99: 455-464.

Wall, K.F., Bhavnani, S.H., Overfelt, R.A., Sheldon, D.S. and Williams, K., 2003. Investigation of the Performance of an Expandable Polystyrene Injector for Use in the Lost-Foam Casting Process. Metallurgical and Materials Transactions B, 34B: 843-851.

Walling, R.P. and Dantzig, J.A., 1995. Mechanisms of Mold Filling in the EPC Process. Transactions of the American Foundrymen's Society, 102: 849-854.

Wang, C., Paul, A.J., Fincher, W.W. and Huey, O.J., 1993. Computational Analysis of Fluid Flow and Heat Transfer during the EPC Process. Transactions of the American Foundrymen's Society, 101: 897-904.

Wang, D., 2001. Thermophysical Properties, Solidification Design Center, Auburn University.

Wang, L., Shivkumar, S. and Apelian, D., 1990. Effects of Polymer Degradation on the Quality of Lost Foam Castings. Transactions of the American Foundrymen's Society: 923-933.

Warner, M.H., Miller, B.A. and Littleton, H.E., 1998. Pattern Pyrolysis Defect Reduction in Lost Foam Castings. Transactions of the American Foundrymen's Society, 106: 777-785.

Wong, H., 2000. Advanced Lost Foam Casting: New Process Control Measures and Technical Knowhow Leading to Accelerated Use of Lost Foam Process, Office of Industrial Technologies, U.S. Department of Energy.

Yang, J., Huang, T. and Fu, J., 1998. Study of Gas Pressure in EPC (LFC) Molds. Transactions of the American Foundrymen's Society, 106: 21-26.

Yao, X., 1994. An Experimental Analysis of Casting Formation in the Expendable Pattern Casting (EPC) Process. M.S. Thesis, Worcester Polytechnic Institute. M.S. Thesis, Worcester Polytechnic Institute.

APPENDIX A

THERMOPHYSICAL PROPERTIES

Table A.1 Thermal degradation characteristics of polymer patterns used in lost foam casting process (Yao, 1994)

	EPS	PMMA
Glass transition temperature (°C)	80 to 100	105
Collapse temperature (°C)	110 to 120	140 to 200
Melting temperature (°C)	160	260
Starting temperature of volatilization (°C)	275 to 300	250 to 260
Peak volatilization temperature (°C)	400 to 420	370
End volatilization temperature (°C)	460 to 500	420 to 430
Heat of degradation (J/g)	912	842
Rate of vaporization at 750°C (Kg/s·m^2)	0.77	0.61
Rate of vaporization at 1300 °C (Kg/s·m^2)	0.18	0.31
Gas yield at 750°C (m^3(STP)/Kg)	0.23	0.273
Gas yield at 1300°C (m^3(STP)/Kg)	0.76	0.804
%Viscous residue at 750°C	61	32
%Viscous residue at 1400°C	15	3

Table A.2 Thermophysical properties of Aluminum alloy 319 (Wang, 2001)

Property	Value
Liquid metal density (kg/m³)	2500
Solid metal density (kg/m³)	2700
Thermal conductivity of liquid metal (W/m·K)	79
Thermal conductivity of solid metal (W/m·K)	145
Specific heat of liquid metal (J/kg·K)	1145
Specific heat of solid metal (J/kg·K)	963
Solidus temperature (°C)	450
Liquidus temperature (°C)	596
Viscosity (Pa·s)	0.0016
Thermal expansion coefficient (1/K)	3.0E-5
Critical solidification fraction above which metal has no fluidity	0.51
Coefficient of solidification drag (1/s)	0.1

Table A.3 Thermophysical conductivity of ANSI 1008, 1025 and interpolated 1018 (Davis, 1990)

Temperature (°C)	ANSI 1008 (W/m·K)	ANSI 1025 (W/m·K)	ANSI 1018 (interpolated) (W/m·K)
100	57.8	51.1	53.9
200	53.2	49.0	50.7
300	49.4	46.1	47.5
400	45.6	42.7	43.9
500	41.0	39.4	40.1
600	36.8	35.6	36.1
700	33.1	31.8	32.3
800	28.5	26.0	27.0

APPENDIX B

PRESSURE TRANSDUCER CALIBRATION

The high accuracy PX800 pressure transducer has a accuracy of ±0.1% BFSL and the pressure range is 0 to 20 kPa. It was calibrated using water column apparatus. A known pressure of water column was applied to an excited transducer and the output voltage was read and converted to pressure through the linear equation provided by Omega Engineering. The water column was applied in increments of 6 inches (15.2 cm) and reached 69 inches (1.75 m). An average of 3 readings was plotted against the standard water column below.

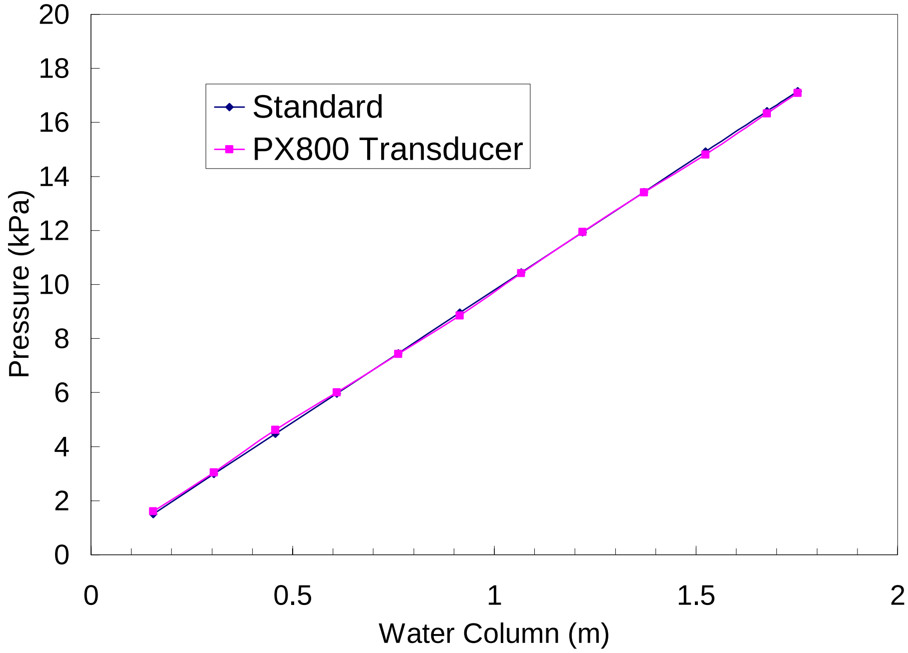

Figure B.1 Calibration curve for pressure transducer PX800

PX70 transducers were also calibrated. These transducers have a linearality of ±0.5% FS and a repeatability of ±0.3% FS with a pressure range of 0 to 15 kPa. A known pressure was applied to an excited transducer and the output voltage was read. An average of 3 readings was plotted and curve fitted to obtain an equation. A typical plot is shown below.

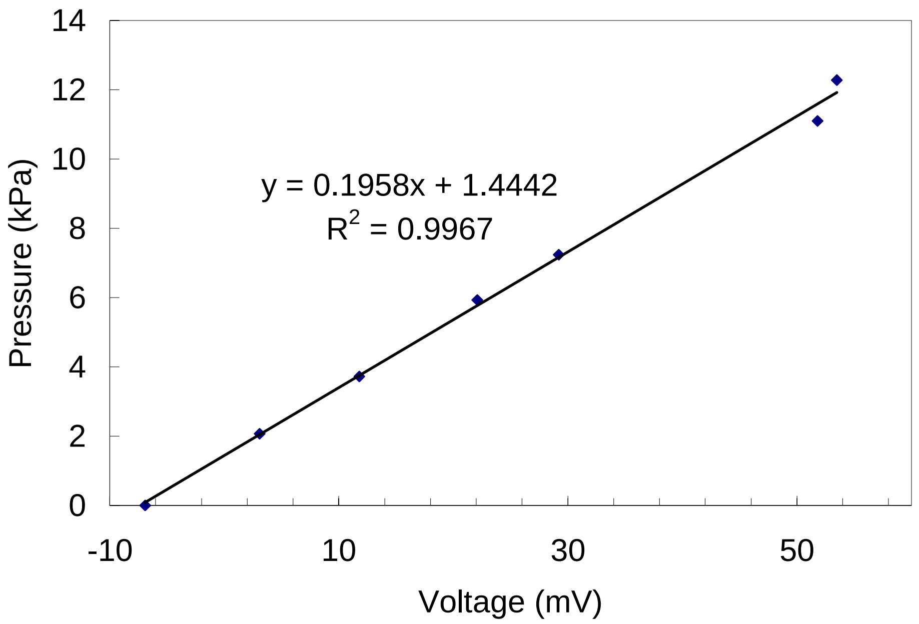

Figure B.2 Calibration curve for pressure transducer PX70

APPENDIX C

UNCERTAINTY ANALYSIS

Uncertainty analysis was performed using the method proposed by Kline and McClintock (1953). In general, some dependent variable may be expressed mathematically as $R=f(x_1, x_2, \ldots, x_n)$, then the absolute uncertainty in R can be obtained as

$$U_R = \sqrt{\left(\frac{\partial R}{\partial x_1}.U_{x_1}\right)^2 + \left(\frac{\partial R}{\partial x_2}.U_{x_2}\right)^2 + \ldots + \left(\frac{\partial R}{\partial x_n}.U_{x_n}\right)^2} \tag{C.1}$$

Where

U_R is the absolute uncertainty;

R is the variable for which the uncertainty is desired;

$x_1, x_2, \ldots, x_n$ are the individual components required to determine R [$R = f(x_1, x_2, \ldots, x_n)$].

The uncertainties in the temperature sensors and pressure transducers are obtained from the manufacturer's user manuals. The uncertainties of sensor positions are determined from the machining equipment.

C.1 Calculating the uncertainty in heat flux u_{qs}

$$q_s = -k \left.\frac{\partial T}{\partial x}\right|_s \tag{C.2}$$

Three data points (x_0, T_0), (x_1, T_1) and (x_2, T_2) are used for the evaluation of temperature gradient at the surface of metal front. The temperature profile can be expressed by 2nd order Lagrange interpolating polynomial,

$$T(x) = \sum_{i=0}^{2} T(i) L_i(x) \tag{C.3}$$

where

$$L_i(x) = \prod_{\substack{i=0 \\ i \neq k}}^{2} \frac{(x - x_i)}{(x_k - x_i)} \qquad (C.4)$$

It can be shown that the temperature gradient is

$$grad = \left.\frac{\partial T}{\partial x}\right|_s = \frac{(x_1 + x_2)T_0}{(x_0 - x_1)(x_0 - x_2)} + \frac{(x_0 + x_2)T_1}{(x_1 - x_0)(x_1 - x_2)} + \frac{(x_0 + x_1)T_2}{(x_2 - x_0)(x_2 - x_1)} \qquad (C.5)$$

Let

$$A = \frac{(x_1 + x_2)T_0}{(x_0 - x_1)(x_0 - x_2)} \qquad (C.6)$$

$$B = \frac{(x_0 + x_2)T_1}{(x_1 - x_0)(x_1 - x_2)} \qquad (C.7)$$

$$C = \frac{(x_0 + x_1)T_2}{(x_2 - x_0)(x_2 - x_1)} \qquad (C.8)$$

The absolute uncertainty in the temperature gradient is

$$U_{grad} = \sqrt{U_A^2 + U_B^2 + U_C^2} \qquad (C.9)$$

The relative uncertainty in the temperature gradient is

$$u_{grad} = \frac{U_{grad}}{grad} = \sqrt{\frac{U_A^2 + U_B^2 + U_C^2}{(A + B + C)^2}} \qquad (C.10)$$

The uncertainty of A, B and C can be easily obtained. For example, A can be rewritten as

$$A = \frac{aT_0}{bc} \qquad (C.11)$$

where

$$a = x_1 + x_2 \qquad (C.12)$$

$$b = x_0 - x_1 \qquad (C.13)$$

$$c = x_0 - x_2 \qquad (C.14)$$

The absolute uncertainty in a is

$$U_a = \sqrt{U_{x1}^2 + U_{x2}^2} \tag{C.15}$$

The relative uncertainty in a is

$$u_a = \sqrt{\frac{U_{x1}^2 + U_{x2}^2}{\left(x_1 + x_x\right)^2}} \tag{C.16}$$

The uncertainty in b and c can be found similarly to the procedures for a. So the relative uncertainty in A is

$$u_A = \sqrt{u_a^2 + u_{T0}^2 + u_b^2 + u_c^2} \tag{C.17}$$

The uncertainty in B and C can be found similarly to the procedures for A. Then the relative uncertainty in the temperature gradient can be calculated.

Typical values for (x_0, T_0), (x_1, T_1) and (x_2, T_2) are (0.1”, 710°C), (0.6”, 730°C) and (1.1”, 750°C). The uncertainty in x is ± 0.001”, the uncertainty in thermocouples is ± 0.4%. By plugging in these values, the relative uncertainty in q_s is found to be 0.35%.

C.2 Calculating the uncertainty heat transfer coefficient *h*

$$h = \frac{q_s}{T_s - T_z} \tag{C.18}$$

Uncertainty in heat transfer coefficient h is

$$u_h = \frac{U_h}{h} = \sqrt{\left(\frac{U_{q_s}}{q_s}\right)^2 + \frac{U_{Ts}^2 + U_{Tz}^2}{\left(T_s - T_z\right)^2}} \tag{C.19}$$

For heat flux, u_{qs}=±0.35%. For T_s, a similar procedure is followed as described in Section C.1, and it is found that u_{Ts}=±1.5%. For temperature sensor, T_s-T_z=500°C, u_{Tz}=±0.4%.

Thus, the relative uncertainty in heat transfer coefficient is found to be u_h=±2.2%.

APPENDIX D

LABVIEW® INTERFACE

The interface was developed in LabVIEW® which continuously scans data through National Instrument PCI-MIO-16XE-50 data acquisition card connected to SCXI-1100 multiplexer amplifier and SCXI-1000 conditioning chassis at a rate of 500 scans/sec out of which every 100 data points were averaged.

The virtual instrumentation (VI) is a user defined interface combining hardware and software to create measurement and control solutions. Within the VI, sub-VIs can be called to produce more complicated tasks. National Instrument provided many useful VIs, such as VIs for thermocouples, data filtering, and plotting functions. Additionally, users can also define modules that can be used as sub-VIs.In the LabVIEW® VI shown in Figure D.1, the first chart shows the pressure measurement through channel 1 performed by the pressure tap going through the heated steel block. A user-defined sub-VI was used to convert the milivolt signal into pound force per square inch (psi). The digital reading is shown next to the plot. The second chart monitors the temperature signals through channel 2 to 5. The number of channels can be easily adjusted by dragging the channel chart and adding additional channels. The user interface is also called as front panel in LabVIEW®. The coding of the front panel is performed in the diagram form known as graphical programming. The Main diagram, file input and device control of the front panel are shown in Figure D.2 and D.3.

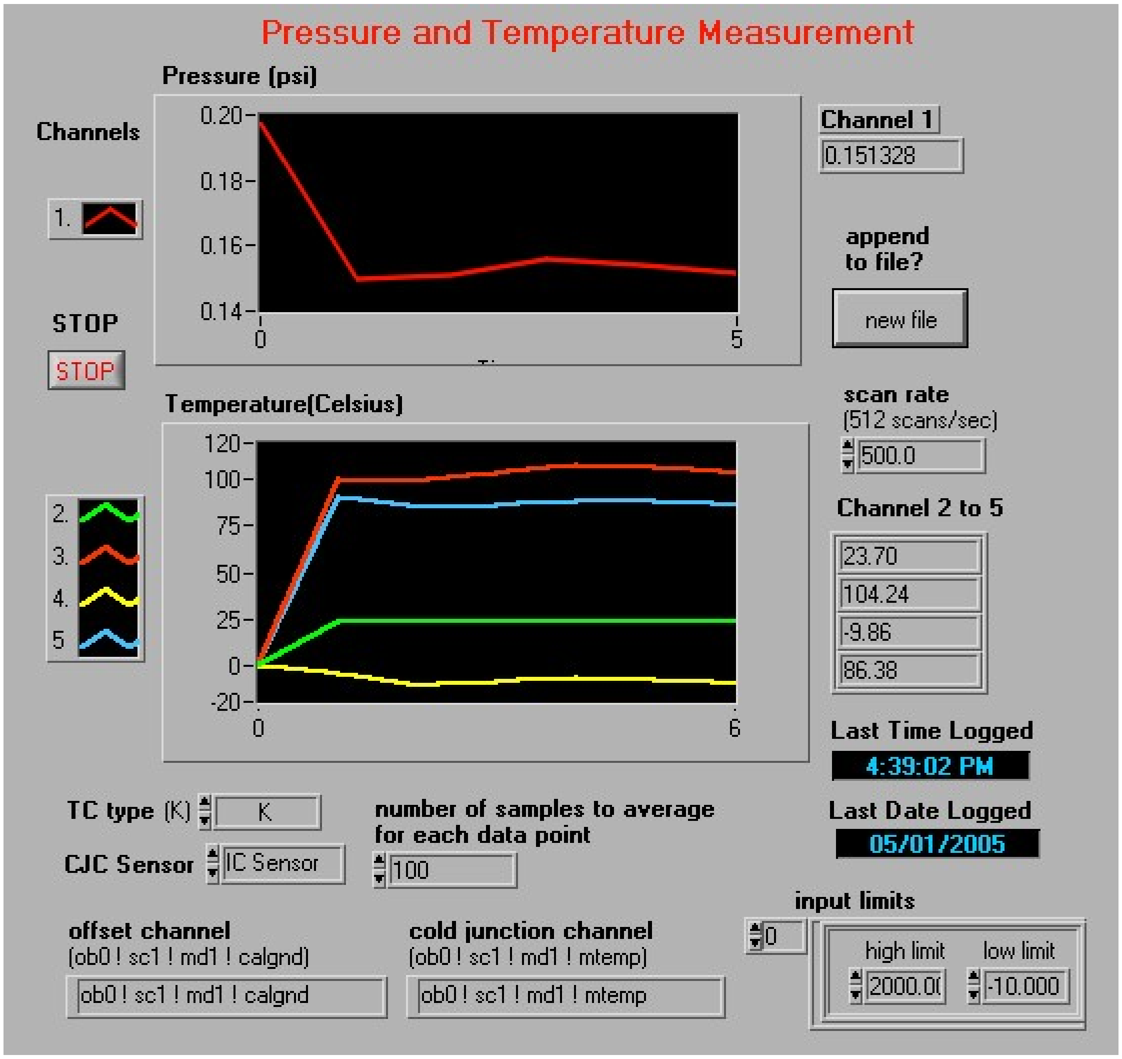
Pressure and Temperature Measurement
Pressure (psi)
Channels
1.
0.20
0.18
0.16
0.14
0
5
STOP
STOP
Temperature(Celsius)
120
100
75
50
25
0
-20
0
6
2.
3.
4.
5
append to file?
new file

Channel 1
0.151328

scan rate (512 scans/sec): 500.0

Channel 2 to 5
23.70
104.24
-9.86
86.38

Last Time Logged: 4:39:02 PM

Last Date Logged: 05/01/2005

TC type (K): K

CJC Sensor: IC Sensor

number of samples to average for each data point: 100

offset channel (ob0 ! sc1 ! md1 ! calgnd): ob0 ! sc1 ! md1 ! calgnd

cold junction channel (ob0 ! sc1 ! md1 ! mtemp): ob0 ! sc1 ! md1 ! mtemp

input limits: 0

high limit: 2000.0(

low limit: -10.000

Figure D.1 Measurement interface developed in LabVIEW®

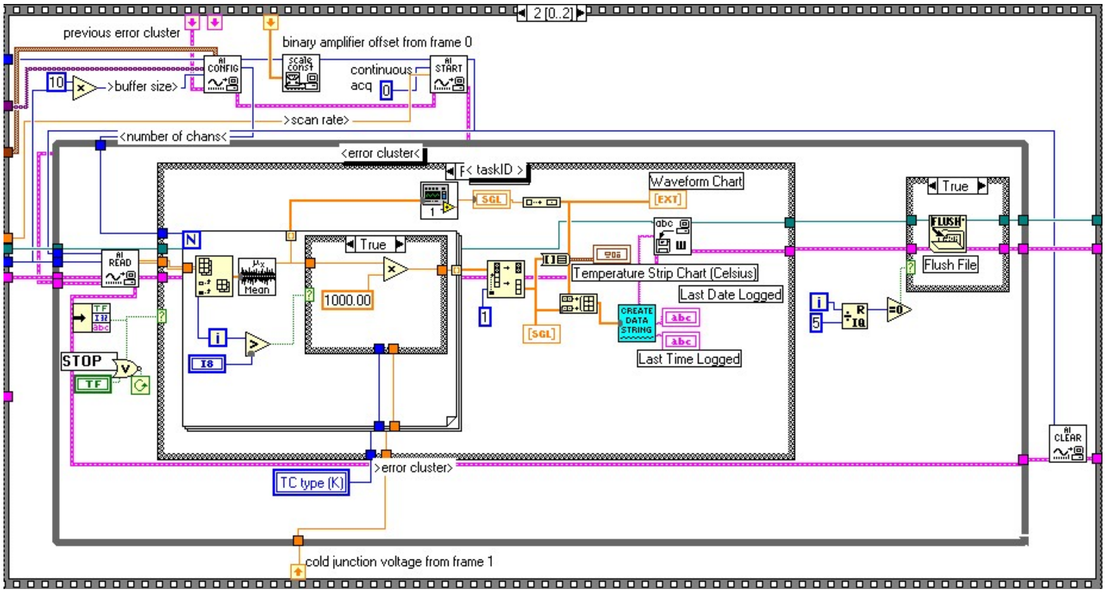
2 [0..2]
previous error cluster
binary amplifier offset from frame 0
10
>buffer size>
AI CONFIG
scale const
continuous acq
0
AI START
>scan rate>
<number of chans<
<error cluster<
F< taskID >
Waveform Chart
SGL
EXT
AI READ
N
Mean
True
1000.00
i
I8
STOP
TF
1
Temperature Strip Chart (Celsius)
Last Date Logged
CREATE DATA STRING
abc
Last Time Logged
SGL
i
5
True
FLUSH
Flush File
AI CLEAR
TC type (K)
>error cluster>
cold junction voltage from frame 1

Figure D.2 Main diagram of the VI measuring temperature and pressure

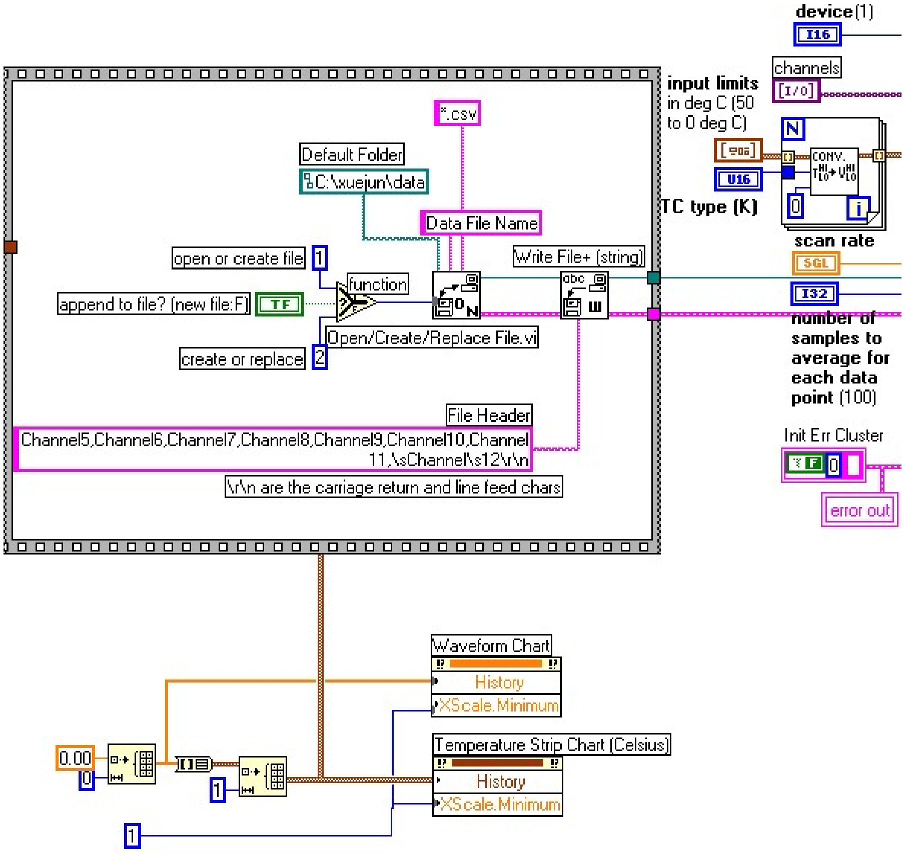
device(1)
I16
channels
I/O
input limits in deg C (50 to 0 deg C)
U16
N
CONV.
0
i
TC type (K)
scan rate
SGL
I32
number of samples to average for each data point (100)
Init Err Cluster
F
0
error out
*.csv
Default Folder
C:\xuejun\data
Data File Name
open or create file
1
append to file? (new file:F)
TF
function
Write File+ (string)
Open/Create/Replace File.vi
create or replace
2
File Header
Channel5,Channel6,Channel7,Channel8,Channel9,Channel10,Channel 11,\sChannel\s12\r\n
\r\n are the carriage return and line feed chars
Waveform Chart
History
XScale.Minimum
Temperature Strip Chart (Celsius)
History
XScale.Minimum
0.00
0
1
1

Figure D.3 File output and devices control in the VI

APPENDIX E

SID 2.0 FHNL SERIAL INTERFACE DEVICE PROGRAM

```
100 KEY ON:                 REM ENABLE FUNCTION KEYS
110 CLS :                   REM CLEAR SCREEN
510 PRINT #ACTIVE, "R 34":  REM  SEND RATE 34
520 PRINT #ACTIVE, "S 235":  REM  SEND SLOPE 235
530 PRINT #ACTIVE, "F 34":   REM  SEND FIRST RATE 34;
540 PRINT #ACTIVE, "/B 0":   REM  SEND SET BIT 0 LOW; ENABLE DRIVER POWER
550 REM PRINT #ACTIVE, "N 800":  REM  SEND NUMBER OF STEPS 800
560 REM PRINT #ACTIVE, "G":      REM  GO NUMBER OF STEPS --------
570 REM PRINT #ACTIVE, "/B 2":   REM  SET BIT 2 LOW
580 REM PRINT #ACTIVE, "H 1":    rem  HOME ON B1 - HOMING COMMAND DISABLED
585 PRINT #ACTIVE, "A 0":    REM  DECLARE CURRENT POSITION AS P = 1
590 REM PRINT #ACTIVE, "P 0":    REM  SEND 'MOVE TO POSITION 0'
600 REM PRINT #ACTIVE, "P 17600": REM  SEND 'MOVE TO POSITION XXXXX'
610 REM PRINT #ACTIVE, "P 0":    REM  MOVE TO POSITION 0
660 PRINT #ACTIVE, "/B 3":   REM  SET BIT 3 LOW
800 PRINT #ACTIVE, "+":      REM SET DIRECTION+
```

APPENDIX F

LIST OF R VALUE CORRESPONDING TO VELOCITY OF THE MOTION SYSTEM

Table F.1 List of R value corresponding to velocity of the motion system

R Value	Step rate	Time to travel 25.4 cm (sec)	Velocity (cm/sec)
10	229	69.9	0.36
12	275	58.2	0.44
21	596	26.8	0.95
29	963	16.6	1.5
34	1192	13.4	1.9

APPENDIX G

DESIGN OF HEATER AND CYLINDER

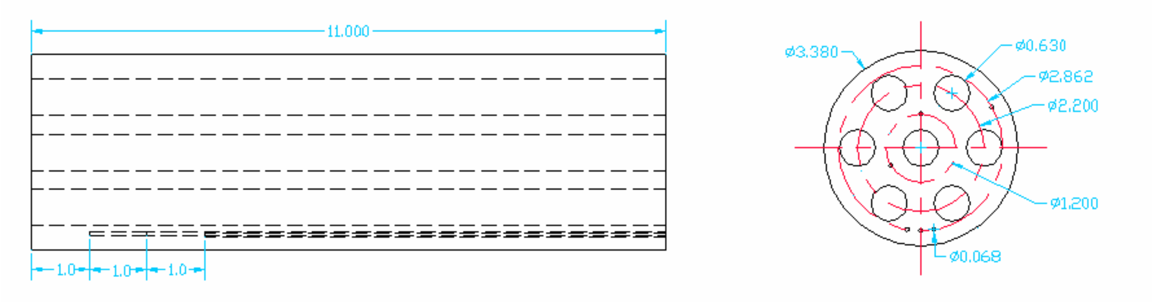
11.000
1.0
1.0
1.0
ø3.380
ø0.630
ø2.862
ø2.200
ø1.200
ø0.068

Figure G.1 Design of steel block with heaters

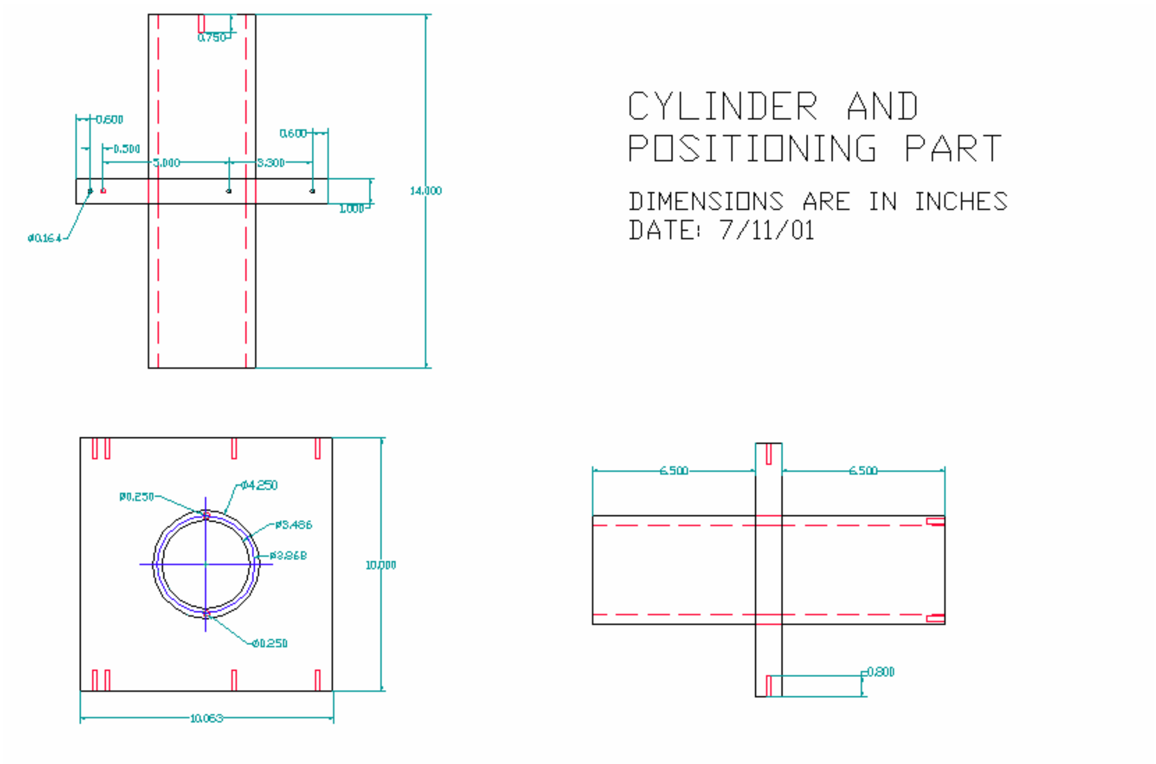
0.750
0.600
0.500
5.000
3.300
0.600
1.000
14.000
ø0.164
CYLINDER AND
POSITIONING PART
DIMENSIONS ARE IN INCHES
DATE: 7/11/01
ø0.250
ø4.250
ø3.486
ø3.868
ø0.250
10.000
10.063
6.500
6.500
0.800

Figure G.2 Design of cylinder and positioning part

APPENDIX H

CUSTOMIZED FORTRAN SUBROUTINE FOR THE IMPROVED MODEL

```
      subroutine hfobcl(nn,ijob,ijnb,htran)
c
c  subroutine for heat transfer coefficient between metal and foam
c
      use arrays_module
c
      use meshcb_module
c
      use voids_module
c
#ifdef SINGLE
      include '../comdeck/precis4.f'
#else
      include '../comdeck/precis.f'
#endif
c
      include '../comdeck/params.f'
      include '../comdeck/cntrl.f'
      include '../comdeck/const.f'
      include '../comdeck/diag.f'
      include '../comdeck/logvar.f'
      include '../comdeck/obsd.f'
      include '../comdeck/obsijk.f'
      include '../comdeck/bcinfo.f'
      include '../comdeck/acctrm.f'
      include '../comdeck/index.f'
      include '../comdeck/scala.f'
      include '../comdeck/state.f'
c
      include '../comdeck/func.f'
c
c     htran=computed heat transfer coefficient
c     nn=obstacle number
c     hobs1(nn)=input heat transfer cofficient for obstacle nn
c     ijob=cell ijk index
c     ijnb=index of neighbor cell with most metal
c     gx,gy,gz = components of gravitational acceleration
c     cgfob=coefficient of proportionality in "roughness" model
c     rough(nn)=characteristic length for heat transfer "roughness"
c
c    ****************************************
c     Basic model htc
       htran=hobs1(nn)
c    ****************************************
c
```

```
c      ***************************************
c      Improved model
c      Time dependent htc
      htrn=htran(0.7649*t**2-0.6488*t+150.0)
c     ****************************************
c      for pressure correction factor
c      Pressure on the interface
      if(fn(ijk).gt.emf) then
      p(ijk)=0.0e4*(1.0/(0.5+fn(ijk)))+(1.0-1.0/(0.5+fn(ijk)))*p(ijkp)
      htran=htran*(0.3+(1-0.3)*(p(ijk)/(p(ijk)+18.0*1.5)))
      sclr(ijk,2)=p(ijk)
      endif
c
c
c       **********************************
c       GM box with sprue htc as a function of pressure
c       8.5 sec filling time
c        htran=htran*(0.5+0.5*(35.0/(35.0+zk(k))))*0.45
c       13.1sec filling time
c        htran=htran*(0.5+0.5*(35.0/(35.0+zk(k))))*0.23
c       *****************************
c       Shivkumar plate
c        htran=htran*(0.0+1.0*(20.0/(20.0+zk(k))))*1.4
c       two gates
c       htran=htran*(0.0+1.0*(20.0/(20.0+zk(k))))*2.0
c       *************************************
c       Yao's plate
c        for temperature dependence
c        T=490C
c        htran=htran*1.4
c        T=190
c        htran=0.7*htran
c        T=715
c        htran=htran*1.2
c        htran=1.4*htran*(490.0/(490.0+abs(490.0-190.0))
c        for 50% degree of fusion
c        htran=htran*1.3
c        for 70% degree of fusion
c        if (t.lt.2.0) then
c        htran=htran*(0.6+0.5*abs(zk(k)-10.0)/10.0)
c        else
c        htran=htran*(0.5+1.2*abs(zk(k)-10.0)/10.0)
c        endif
c
c ------- include pressure and temperature dependencies
```

```
c     p(ijob) = pressure of ijob cell
c     tn(ijob) = fluid temperature of ijob cell
c     xi(i),yj(j),zk(k) = center of ijk cell
c     i,j,k recovered from ijob using call inijk(ijob,i,j,k)
c     idum1,...,idum9 = dummy integer parameters for model building
c     dum1,...,dum9 = dummy floating point parameters for model building
c -------
c
c ------- add gravitational "roughness" effect (foaml is characteristic
c         length)
      if(cgfob.lt.ztest .or. rough(nn).lt.ztest) return
           ght=zero
           if(fabs(gx).gt.ztest) then
             if(ijnb.eq.imjk) ght=gx
             if(ijnb.eq.ipjk) ght=-gx
           endif
           if(fabs(gy).gt.ztest) then
             if(ijnb.eq.ijmk) ght=gy
             if(ijnb.eq.ijpk) ght=-gy
           endif
           if(fabs(gz).gt.ztest) then
             if(ijnb.eq.ijkm) ght=gz
             if(ijnb.eq.ijkp) ght=-gz
           endif
           if(fabs(ght).gt.ztest) then
             gvel=fsqrt(fabs(ght)*rough(nn))
             htcor=fsign(cgfob,ght)*gvel/(gvel+hobs1(nn)/rcobs(nn))
             htran=htran*(one+htcor)
c          htran=htran*(one+htcor)*(one+0.5*p(ijob)/(p(ijob)+8.0e4))
           endif
      return
      end
```

APPENDIX I

FLOW-3D$^{®}$ PROJECT INPUT FILE EXAMPLE

```
&xput --- numerical controls, options, time control
twfin = 1.00,     Time to end calculation.
delt = 0.001,      Initial time step size
prtdt =1000.0,  Time interval between long prints in HD3OUT
itb =1,           Indicator for free surfaces or sharp interfaces,=1, free surface or sharp
interface
ihtc =1,           Fluid / obstacle heat transfer flag,=1, evaluate heat transfer
gz =-980.,
ifenrg =2, Flag for internal energy evaluation, 2, solve transport equation for internal
energy (1st order advection)

&limits---output and numerical limits

&props---material properties
rhof =2.7,         Density of fluid #1.
cv1 =8.37e+6,   Specific heat of fluid #1
thc1 =1.88e+7,  Thermal conductivity of fluid #1
tl1 =933.0,        Liquidus temperature of fluid #1. (Used only when TS1>0.)
ts1 =933.0,         Solidus temperature of fluid #1.
clht1 =3.94e+9, Latent heat of fusion in fluid #1(alt: CLHT).
remark='set limited compressibility for better convergence',
rcsql =0.1e-6,   Reciprocal (rho•c²) of fluid #1
mu1 =0.03,       Dynamic viscosity of fluid #1.

&scalar
remark='set surface contaminant model parameters',
    nsc =1,             remark='total number of scalar functions',
    idfct =1,           remark='scalar index used for tracking contaminant',
    isclr(1) =3,        remark='use higher order advection for contaminant',
    dftfob =1.0e+3,      remark='scaling factor for contaminant source',

 &bcdata ---boundary conditions
    wl =5,    pbc(1) =7.41e+4,  Pressure at mesh boundary n
    tbc(1) =988.2,    Temperature at mesh boundary n
    fbc(1) =1.0, Fluid fraction at mesh boundary n
           sclbc(1,1) =0.0, Scalar magnitude of species ns at mesh boundary n
    wr =2,
    wf =2,          wbk =2,                 wb =2,           wt =2,
    hwall1(5) =1.0e+4,   hwall1 (6)=1.0e+4,
    hwall1(3) =1.0e+4,   hwall1 (4)=1.0e+4,
    Fixed heat transfer coefficient to fluid #1 from mesh boundary n.
    tbcd=298.2, Default obstacle and mesh boundary surface temperature.

&mesh---grid generation
    nxcelt=60,
     px(1)=-0.1,     px(2)=0.0,        px(3)=0.736,

     nycelt=1,
       py(2)=0.323,

     nzcelt=17,
       pz(1)=0.0,      pz(2)=0.246,      pz(3)=0.514,

&obs---geometry definition
  remark='first obstacle described flow obstruction',
  remark='second obstacle describes foam',
    avrck =-2.1, AVRCK<0, a negative value flags preprocessor to adjust cell volume
fractions so ratio does not exceed magnitude of AVRCK
    nobs =2,
    hobs1(1) =1.0e+4,   Heat-transfer coefficient to fluid #1 for obstacle m
twobs(1,1)=298.2, Time-dependent heat transfer surface temperature at time TOBS(t) for
obstacle m.
    iob(1) =1,
     xl(1)=0.736,   xh(1)=1.209,
     zl(1)=0.514,   zh(1)=1.22,
    iob(3) =1,
     rah(3)=0.26,   rotx(3)=90.0, trnx(3)=3.677, trnz(3)=1.0,
   iob(7) =2,      remark='obstacle 2 is foam',
    ifob(2)=1,    remark='foam flag for obstacle 2',
  remark='set foam properties and initial temperature',
    hobs1(2) =6.0e6,               remfob(2) =1.6e5,(rho*Emelt),  tmfob(2) =373.0, (Tmelt)
    rcobs(2) =8.0e5, (rho*Cp),  revfob(2) =0.8e+5,(rho*Evap),   tvfob(2) =1020.0, (Tvap)
    twobs(1,2) =338.2,  ospor(2) =10.0, Surface area per unit bulk volume for porous
obstacle m (used for heat transfer only).
&fl --- initial conditions
    pvoid=0.0, Default void initial total pressure (vapor plus non-condensable).

&bf --- baffle definition
   nbafs=0, Number of porous baffles

&temp --- initial temperature
  remark='set initial metal temperature',
   tempi =988.2,

&grafic --- output request
   nvplts=2,         contpv(1)='sclr1',
                contpv(2)='vfob',   remark='plot request for foam',
   vqmx(1)=4000.,

&parts --- mass/marker particles
```